



UNIVERSIDADE ESTADUAL DE CAMPINAS
FACULDADE DE CIÊNCIAS MÉDICAS

MONIQUE CULTURATO PADILHA MENDONÇA

**ÓXIDO DE GRAFENO E SISTEMA NERVOSO CENTRAL: AVALIAÇÃO DOS
EFEITOS NA BARREIRA HEMATOENCEFÁLICA E PERFIL
NANOTOXICOLÓGICO**

***GRAPHENE OXIDE AND CENTRAL NERVOUS SYSTEM: EVALUATION OF
EFFECTS ON BLOOD BRAIN BARRIER AND NANOTOXICOLOGICAL PROFILE***

CAMPINAS

2016

MONIQUE CULTURATO PADILHA MENDONÇA

**ÓXIDO DE GRAFENO E SISTEMA NERVOSO CENTRAL: AVALIAÇÃO DOS
EFEITOS NA BARREIRA HEMATOENCEFÁLICA E PERFIL
NANOTOXICOLÓGICO**

***GRAPHENE OXIDE AND CENTRAL NERVOUS SYSTEM: EVALUATION OF
EFFECTS ON BLOOD BRAIN BARRIER AND NANOTOXICOLOGICAL PROFILE***

Tese apresentada à Faculdade de Ciências Médicas da
Universidade Estadual de Campinas como parte dos requisitos
exigidos para a obtenção do título de Doutora em Farmacologia.

*Thesis presented to the Faculty of Medical Sciences, State
University of Campinas as part of the requirements for obtaining
the title of Doctor in Pharmacology.*

ORIENTADORA: PROFA. DRA. MARIA ALICE DA CRUZ HOFLING

ESTE EXEMPLAR CORRESPONDE À
VERSÃO FINAL DA TESE DEFENDIDA PELA
ALUNA MONIQUE CULTURATO PADILHA MENDONÇA, E
ORIENTADA PELA PROFA. DRA. MARIA ALICE DA CRUZ HOFLING

CAMPINAS

2016

Agência(s) de fomento e nº(s) de processo(s): FAPESP, 2012/24782-5; FAPESP, 2015/03254-9

Ficha catalográfica
Universidade Estadual de Campinas
Biblioteca da Faculdade de Ciências Médicas
Maristella Soares dos Santos - CRB 8/8402

M523o Mendonça, Monique Culturato Padilha, 1986-
Óxido de grafeno e sistema nervoso central : avaliação dos efeitos na barreira hematoencefálica e perfil nanotoxicológico / Monique Culturato Padilha Mendonça. – Campinas, SP : [s.n.], 2016.

Orientador: Maria Alice da Cruz Hofling.
Tese (doutorado) – Universidade Estadual de Campinas, Faculdade de Ciências Médicas.

1. Barreira hematoencefálica. 2. Nanoestruturas. 3. Óxido de grafeno reduzido. 4. Toxicidade. I. Cruz-Hofling, Maria Alice da, 1944-. II. Universidade Estadual de Campinas. Faculdade de Ciências Médicas. III. Título.

Informações para Biblioteca Digital

Título em outro idioma: Graphene oxide and central nervous system : evaluation of effects on blood brain barrier and nanotoxicological profile

Palavras-chave em inglês:

Blood-brain barrier

Nanostructures

Reduced graphene oxide

Toxicity

Área de concentração: Farmacologia

Titulação: Doutora em Farmacologia

Banca examinadora:

Maria Alice da Cruz Hofling [Orientador]

Frank Denis Torres Huaco

Alexandre Leite Rodrigues de Oliveira

Patricia da Silva Melo

Leonardo Fernandes Fraceto

Data de defesa: 23-06-2016

Programa de Pós-Graduação: Farmacologia

BANCA EXAMINADORA DA DEFESA DE DOUTORADO

MONIQUE CULTURATO PADILHA MENDONÇA

ORIENTADORA: PROFA. DRA. MARIA ALICE DA CRUZ HOFLING

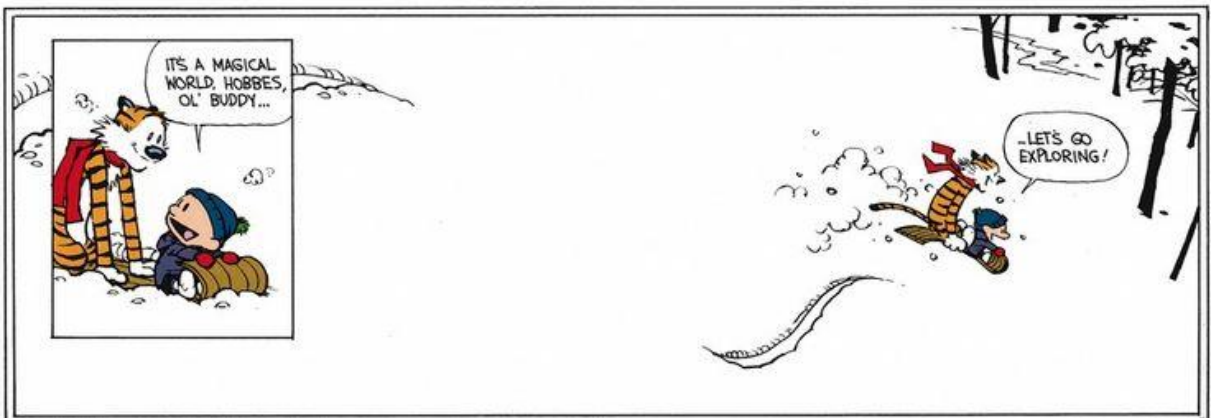
MEMBROS:

- 1. PROFA. DRA. MARIA ALICE DA CRUZ HOFLING**
 - 2. DR. FRANK DENIS TORRES HUACO**
 - 3. PROF. DR. ALEXANDRE LEITE RODRIGUES DE OLIVEIRA**
 - 4. PROFA. DRA. PATRICIA DA SILVA MELO**
 - 5. PROF. DR. LEONARDO FERNANDES FRACETO**
-

Programa de Pós-Graduação em Farmacologia da Faculdade de Ciências Médicas da Universidade Estadual de Campinas.

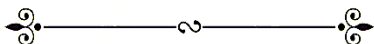
A ata de defesa com as respectivas assinaturas dos membros da banca examinadora encontra-se no processo de vida acadêmica da aluna.

Data: 23/06/2016



Calvin and Hobbes by Bill Watterson, 1995: 'A day full of possibilities'.....'It's a magical world, Hobbes, ol'buddy.'

DEDICATÓRIA



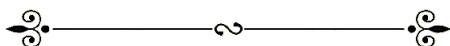
Dedico este trabalho...

*Aos meus pais, Claudenir Padilha (in memoriam) e Fátima Padilha,
minha eterna incentivadora.*

*Ao Bruno, meu porto seguro, pelo apoio nos momentos de dificuldade e por assumir meu
lugar enquanto me dediquei à pesquisa,
minhas desculpas e eterna gratidão.*

*A minha filha Maria Eduarda, fonte especial da minha inspiração e entusiasmo,
que mesmo tão pequena compreende a importância dessa conquista
e aceitou a minha ausência.*

AGRADECIMENTOS



- À minha querida orientadora Prof^a Dr^a. Maria Alice da Cruz Hofling, exemplo de ética e amor à profissão. Já dizia Rubem Alves: “Todo conhecimento começa com o sonho.” Obrigada por me ajudar na construção deste sonho!
- Ao Prof. Dr. István Krizbai, pela hospitalidade, ensinamentos e por me proporcionar a oportunidade de participar de trabalhos excepcionais no Biological Research Centre, Szeged, Hungria.
- Ao Prof. Dr. Marcelo Bispo de Jesus pelo constante apoio e por estruturar bases que, com certeza, serão fundamentais para alcançar meus objetivos futuros.
- Aos membros da banca do exame de qualificação, Prof. Dr. André Almeida Schenka, Prof. Dr. Marcelo Lancellotti e Profa Dra Elaine Conceição de Oliveira, agradeço pela disponibilidade e pelas valiosas contribuições. Aos membros da banca da defesa, Dr. Frank Denis Torres Huaco, Prof. Dr. Alexandre Leite Rodrigues de Oliveira, Profa Dra Patricia da Silva Melo e Prof. Dr. Leonardo Fernandes Fraceto, agradeço por terem aceitado fazer parte deste momento final, podendo então, compartilhar seus conhecimentos.
- Aos professores do Departamento de Farmacologia por todo conhecimento ministrado ao longo do curso.
- Aos bioteristas Miguel Silva e Antônio Vilson dos Santos pelos cuidados com os animais de experimentação, tão importantes para este trabalho.
- Às técnicas de laboratório Stephanie Souto e Cíntia Rizoli pelo apoio precioso que proporcionaram.
- À todos meus amigos que me apoiaram e incentivaram de maneira mais próxima ou mesmo à distância. Em especial aos amigos brasileiros Bruno Kenzo, Maria Helena R. M. Britto e Thaísa

Fachinelli; aos húngaros Imola Wilhelm, Csilla Fazakas, János Haskó, Ádám Nyúl-Tóth, Judit Molnár e Fruzsina Walter e minha flatmate mexicana Lupita Valle.

- À eterna amiga Edilene Siqueira Soares por me acompanhar durante toda trajetória acadêmica. “In good times and bad times....that’s what friends are for!” (Rod Stewart). Obrigada pela amizade verdadeira!
- À toda minha família por todo o amor dispensado e compreensão necessária para conviver comigo nesta fase de formação.
- Ao meu irmão Ryan pelo carinho e por torcer sinceramente pelas minhas conquistas.
- À Fundação de Amparo à Pesquisa do Estado de São Paulo (FAPESP) pelo suporte financeiro concedido através da Bolsa Regular para Doutorado (Processo 2012/24782-5) e Bolsa Estágio de Pesquisa no Exterior (BEPE) (Processo 2015/03254-9).
- A todos que de alguma forma contribuíram para realização deste trabalho.
- Por último, agradeço a Deus por sua proteção e amparo, pela saúde e pela força que me concedeu, para que conseguisse chegar até aqui.

Muito obrigada de coração !!!

RESUMO

A barreira hematoencefálica (BHE), localizada na interface sangue-cérebro, é uma estrutura dinâmica destinada a manter a homeostasia do sistema nervoso central (SNC) através da regulação altamente restritiva propiciada por barreiras físicas e moleculares, tanto paracelulares quanto transcelulares. Entretanto, a BHE também restringe a entrada de agentes terapêuticos importantes para o tratamento de desordens do SNC. Dentre as abordagens utilizadas para superar o problema, a utilização de nanomateriais é particularmente promissora. Os nanomateriais de carbono despertam grande interesse devido às extraordinárias propriedades físico-químicas que apresentam e ao fato de que a (sub)organização celular do SNC e dos nanomateriais a base de carbono compartilham semelhanças morfológicas e funcionais. Na primeira fase deste projeto, analisamos (i) a capacidade do óxido de grafeno reduzido (rGO) modular a permeabilidade da BHE de ratos Wistar adultos, (ii) os possíveis mecanismos envolvidos neste processo, (iii) a toxicidade deste nanomaterial 15 minutos, 1 hora, 3 horas e 7 dias após administração de uma dose intravenosa única (7 mg/kg). rGO concentrou-se principalmente no tálamo e hipocampo, com pico de distribuição ocorrendo às 3 horas, como detectado por espectroscopia de massas por imagem. A presença sistêmica de rGO induziu abertura transitória da BHE no hipocampo dos animais como demonstrado em nível anatômico (infusão de azul de Evans), subcelular (microscopia eletrônica de transmissão) e molecular (expressão de proteínas da via paracelular e transcelular). Os ratos tratados com rGO mostraram-se clinicamente indistinguíveis dos animais controle injetados com veículo (água destilada). Análises hematológicas, histopatológicas (marcadores de neurônios e astrócitos), bioquímicas (avaliação nefrotoxicidade e hepatotoxicidade) e testes genotóxicos mostraram que a injeção de rGO produziu efeitos toxicológicos mínimos nos tempos avaliados. Comparando com o grupo controle, os animais tratados com rGO apresentaram diminuição nos níveis de ureia 3 horas pós-tratamento e aumento na atividade de superóxido-dismutase 1 hora e 7 dias pós-tratamento. Alterações intra-rGO-grupos foram leucocitose (rGO-1 hora *vs.* rGO-3 horas) e leucopenia (rGO-3 horas *vs.* rGO-7 dias), no entanto, nenhuma resposta inflamatória foi observada no soro e no hipocampo, região onde a BHE foi permeabilizada. Na segunda fase do projeto, foram realizados testes *in vivo* e *in vitro* com rGO funcionalizado com o polímero polietilenoglicol (PEG 6.000). A peguilação tem sido usada para melhorar as características físico-químicas dos nanomateriais. Com a concentração mais elevada (100 µg/ml), rGO não funcionalizado

apresentou baixa toxicidade, enquanto rGO-PEG induziu efeitos deletérios e morte em cultura primárias de astrócitos e células endoteliais de cérebro de ratos. Corroborando os dados *in vitro*, houve progressiva diminuição na expressão de marcadores astrocitários (GFAP e conexina-43) e marcadores da junção de oclusão, adesão e lâmina basal (occludina, β -catenina e laminina) após injeção de rGO-PEG *in vivo*, dados estes indicativos de ruptura da BHE. A formação intracelular de espécies reativas de oxigênio *in vitro* e o aumento no sistema antioxidante enzimático *in vivo* induzido por rGO-PEG sugerem danos mediados por estresse oxidativo. Concluimos que dentro das condições experimentais utilizadas rGO, mas não rGO-PEG, pode ser uma ferramenta promissora a ser testada como veículo para entrega de fármacos que possuem difícil acesso ao SNC.

Palavras-chave: Barreira hematoencefálica. Nanomateriais. Óxido de grafeno reduzido. Toxicidade.

ABSTRACT

The blood brain barrier (BBB), located on the blood-brain interface, is a dynamic structure destined to maintain the homeostasis of central nervous system (CNS) through the highly restrictive control afforded by physical and molecular barriers from paracellular and transcellular pathway. However, BBB also restricts the entry of important therapeutic agents for the treatment of CNS disorders. Among the approaches used to overcome this problem, the use of nanomaterials is particularly promising. Carbon-based nanomaterials arouse great interest due to their extraordinary physicochemical properties and morphological and functional similarities shared between the (sub)cellular organization of the CNS and carbon-based nanomaterials. In the first part of the project, we analyze (i) the ability of reduced graphene oxide (rGO) to modulate the permeability of BBB in adults Wistar rats, (ii) the possible mechanisms involved in this process, (iii) the toxicity of this nanomaterial 15 minutes, 1 hour, 3 hours and 7 days after a single intravenous administration (7 mg/kg). rGO were mainly concentrated in thalamus and hippocampus, with peak of distribution occurring at 3 hours, as detected by mass spectroscopy imaging. Systemic presence of rGO induced transient opening of the BBB in the hippocampus of animals as shown at anatomical (Evans blue dye infusion), subcellular (transmission electron microscopy) and molecular (expression of paracellular and transcellular pathway proteins) levels. The rGO-treated rats were clinically indistinguishable from controls animals injected with vehicle (distilled water). Hematological, histopathological (neurons and astrocytes markers), biochemical (nephrotoxicity and hepatotoxicity assessment) and genotoxicological based tests showed that systemic rGO injection seemed to produce minimal toxicological effects at the time points assessed. Regarding the control group, rGO-treated animals exhibited reduction in blood urea nitrogen level 3 hours post-treatment and increases in superoxide dismutase activity 1 hour and 7 days post-treatment. Intra-treated groups alterations involved leukocytosis (rGO-1 hour *vs.* rGO-3 hours) and leukopenia (rGO-3 hours *vs.* rGO-7 days), nevertheless, no inflammatory response was induced in the serum and hippocampus, the permeabilized region of BBB. In the second part of the project, *in vivo* and *in vitro* tests were carried out using rGO functionalized with polyethylene glycol (PEG 6,000). The PEGylation has been used to improve the physicochemical characteristics of nanomaterials. Using the highest concentration (100 µg/ml), non-functionalized rGO showed low toxicity whereas rGO-PEG induced deleterious effects and death in primary culture of astrocytes and rat brain endothelial cells. Corroborating the *in vitro*

data, there was a progressive decrease in the expression of astrocytic markers (GFAP and connexin-43), tight and adherens junctions and basal lamina (occludin, β -catenin and laminin) markers after rGO-PEG injection *in vivo*, indicating BBB disruption. The formation of intracellular ROS *in vitro* and the increase in the enzymatic antioxidant system *in vivo* induced by PEGylated rGO indicated oxidative stress-mediated damage. We concluded that within the experimental conditions used rGO, but not rGO-PEG, could be a promising tool to be tested as a carrier for delivery of drugs that have difficult access to the CNS.

Key words: Blood-brain barrier. Nanomaterials. Reduced graphene oxide. Toxicity.

LISTA DE ILUSTRAÇÕES

Introdução

Fig. 1 Componentes celulares da barreira hematoencefálica.....	21
Fig. 2 Componentes moleculares das junções endoteliais	22
Fig. 3 Vias de acesso ao SNC através da BHE	28
Fig. 4 Estratégias para entrega de fármacos para o SNC	28
Fig. 5 Representação esquemática das possíveis vias envolvidas no transporte de drogas do nariz ao cérebro e à corrente sanguínea sistémica	29
Fig. 6 Vários tipos de nanomateriais à base de carbono	34
Fig. 7 Síntese do óxido de grafeno reduzido a partir do grafite	36
Fig. 8 Representação esquemática das principais características físico-químicas e das várias aplicações biológicas dos nanomateriais da família do grafeno	38
Fig. 9 Mecanismo de toxicidade dos nanomateriais da família do grafeno	42

Capítulo I

Fig. 1 rGO morphology and physicochemical characterization	47
Fig. 2 Compiled mass spectra of (a) an aqueous suspension of rGO and (b) hippocampal tissue 1 h after rGO injection in rats	48
Fig. 3 MALDI-MSI images of a coronal section of rat brain tissue and the density of rGO in the brain	49
Fig. 4 Visualization of rGO by confocal laser microscopy and light microscopy.....	50
Fig. 5 Gross view of a whole brain after infusion with Evans blue dye	51
Fig. 6 Electron micrographs of rat hippocampal capillaries.....	51
Fig. 7 Molecular evaluation of hippocampal BBB paracellular pathway proteins as assessed by Western blotting	52
Fig. 8 Schematic representation of the present experimental design aimed at demonstrating nanomaterial-based opening of the blood-brain barrier.....	53
Fig. 9 Methodology used for quantitative analysis of rGO.....	53

Capítulo II

Fig. 1 Light micrographs of CA1 hippocampal subfield of rats 1 h after i.v. injection of vehicle (A) and 15 minutes after i.v. injection of rGO (B), Hematoxylin-eosin	61
Fig. 2 Expression of TNF- α (A) and IFN- γ (B) in hippocampal homogenates after rGO i.v. administration (7 mg/kg)	62
Fig. 3 Light micrographs of parts of hepatic lobules at 1 h-control (A,C,E), rGO-15 minutes (B) and 7 days -rGO treated rats (D,F)	63
Fig. 4 Renal cortical sections stained with Hematoxylin-Eosin (A,B), immunostained for caspase 9 (C,D) and stained with Masson's trichrome (E,F)	64
Fig. 5 Expression of SOD-1 (A) and catalase (B) in hippocampal homogenates after rGO i.v. administration (7 mg/kg)	66
Fig. 6 FE-SEM images of rGO sheet with a thickness of ~5 nm (A). Stability of rGO in water and different physiological solution including 0.9% saline solution, cell medium (DMEM) and BSA (B)	67

Capítulo III

Fig. 1 rGO-PEG characterization	80
Fig. 2 Effect of rGO-PEG treatment on the viability of primary culture of rat astrocytes	82
Fig. 3 Effects of rGO and rGO-PEG treatment on rat brain endothelial cells	84
Fig. 4 Expression of hippocampal BBB paracellular pathway proteins as assessed by WB	86
Fig. 5 Expression of astrocytic markers assessed by WB in hippocampal homogenate	87
Fig. 6 ROS levels in astrocytes	89
Fig. 7 Effects of rGO-PEG administration in antioxidant enzymes.....	90

Apêndice

Fig. 1 Fotografia representativa da distribuição do corante Azul de Evans 3 horas após a injeção de rGO (7mg/kg)	118
Fig. 2 Fotografias representativas de ratos adultos injetados com Azul de Evans 3 horas após a administração de (A) água destilada e (B) rGO	118
Fig. 3 Expressão de caveolina-1 após a administração i.v. de 7 mg/kg de rGO	119

Fig. 4 Efeitos da administração i.v. de 7 mg/kg de rGO na expressão da (A) proteína de influxo de glicose GLUT-1 e (B) proteína de efluxo P-gp em homogenato hipocampal.	119
Fig. 5 Fotomicrografias representativas de secções histológicas de fígado após injeção i.v. de (A) PEG (controle) e (B-E) rGO-PEG	120
Fig. 6 Fotomicrografias representativas do cortex renal após injeção i.v. de (A) PEG (controle) e (B-E) rGO-PEG	121

LISTA DE SIGLAS E ABREVIATURAS

Siglas e abreviaturas em português/latim

BHE	Barreira Hematoencefálica
C	Carbono
CA1	<i>Cornus Ammonis 1</i>
CO₂	Dióxido de Carbono
Cx	Conexinas
DMSO	Dimetilsulfóxido
EROS	Espécies Reativas de Oxigênio
KOH	Hidróxido de Potássio
NaOH	Hidróxido de Sódio
O₂	Oxigênio
PEG	Polietilenoglicol
P-gp	Glicoproteína-P
SNC	Sistema Nervoso Central
UV-VIS	ultravioleta-visível
ZO	<i>Zonula Occludens</i>

Siglas e abreviaturas em inglês

¹³C NMR	Carbon 13 Nuclear Magnetic Resonance
AJ	Adherens Junction
ALT	Alanine Aminotransferase
ANOVA	Analysis of Variance
AST	Aspartate Aminotransferase
ATP	Adenosine Triphosphate
BBB	Blood-Brain Barrier
BUN	Blood Urea Nitrogen
C	Carbon
CAT	Catalase
CH₂	Methylene
CH₃	Methyl Group
CI	Cell Index

CM-H2DCFDA	5-(6)-Chloromethyl-2',7'-Dichlorodihydrofluorescein Diacetate, Acetyl Ester
CNS	Central Nervous System
Cx43	Connexin-43
DLS	Dynamic Light Scattering
DNA	Deoxyribonucleic Acid
DOC	Sodium Deoxycholate
ESAM	Endothelial Cell-Selective Adhesion Molecules
Fe₃O₃	Iron oxide
FESEM	Field Emission Scanning Electron Microscopy
FDA	Food and Drug Administration
FTIR-ATR	Fourier-transform Infrared Spectroscopy in the Attenuated Total Reflectance Mode
GFAP	Glial Fibrillary Acidic Protein
GJ	Gap-junction
GLUT-1	Glucose Transporter 1
GO	Graphene Oxide
H	Hydrogen
Hb	Hemoglobin
Hct	Hematocrit
HRTEM	High-Resolution Transmission Electron Microscopy
IFN-γ	Interferon-γ
JAM	Junctional Adhesion Molecules
LAT-1	L-Type Amino Acid Transporter 1
MALDI-MSI	Matrix Assisted Laser Desorption/Ionization Mass Spectrometry Imaging
MCH	Mean Corpuscular Hemoglobin
MCHC	Mean Corpuscular Hemoglobin Concentration
MCV	Mean Corpuscular Volume
MRPs	Multidrug Resistance-Associated Proteins
N	Nitrogen
NeuN	Neuronal Nuclei
O	Oxygen
PBS	Phosphate Buffered Saline
PCA	Principal Component Analysis
PDI	Polydispersity Index
PECAM	Platelet Endothelial Cell Adhesion Molecule
PEDOT	Poly (3,4-ethylenedioxythiophene)

PEG	Polyethylene glycol
PFA	Paraformaldehyde
PLT	Platelet
PPO	Red Blood Cell
RBC	Polyphenol Oxidase
RBECs	Rat Brain Endothelial Cells
RER	Rough Endoplasmic Reticulum
RES	Reticuloendothelial System
rGO	Reduced Graphene Oxide
RNA	Ribonucleic Acid
RO-201724	4-(3-butoxy-4-methoxybenzyl)imidazolidin-2-one
ROS	Reactive Oxygen Species
SEM	Standard Error of the Mean
siRNA	Small interfering RNA
SOD	Superoxide Dismutase
TBARS	Thiobarbituric Acid Reactive Substances
TEM	Transmission Electron Microscopy
TJ	Tight Junction
TNF-α	Tumor Necrosis Factor- α
WB	Western Blotting
WBC	White Blood Cell

SUMÁRIO

I Introdução	21
1 Barreira hematoencefálica	21
1.1 Unidade Neurovascular	22
1.1.1 Células endoteliais	22
1.1.2 Pericitos.....	23
1.1.3 Lâmina basal.....	24
1.1.4 Astrócitos	24
1.1.5 Neurônios e interneurônios	25
1.2 Vias de acesso ao SNC através da BHE	26
1.3 Estratégias para entrega de fármacos ao SNC através da BHE	28
1.3.1 Administração local.....	29
1.3.2 Administração via intranasal	29
1.3.3 Modulação da BHE.....	30
2 Nanomateriais	33
2.1 Grafeno e nanomateriais da família do grafeno	34
2.2 Funcionalização	36
2.3 Nanomedicina	38
2.3.1 Biosensores	38
2.3.2 Crescimento e diferenciação de células	39
2.3.3 Engenharia de tecidos	39
2.3.4 Entrega de fármacos e genes	40
2.4 Nanotoxicidade	40
II Objetivos	43
2 Objetivo geral.....	43
2.1 Objetivos específicos.....	43
III Capítulos	44
Capítulo I - Reduced graphene oxide induces transient blood-brain barrier opening: an in vivo study.....	45
Capítulo II - Reduced graphene oxide: nanotoxicological profile	58

Capítulo III- PEGylation of reduced graphene oxide induces toxicity in cells of the blood-brain barrier: <i>in vitro</i> and <i>in vivo</i> studies	71
IV Discussão Geral	96
4.1 Caracterização dos nanomateriais	96
4.2 Distribuição do nanomaterial no parênquima cerebral	98
4.3 Avaliação da integridade da BHE	100
4.4 Avaliação <i>in vivo</i> da toxicidade aguda e subcrônica de rGO	101
4.5 Avaliação dos efeitos da pegulação sobre a toxicidade de rGO <i>in vitro</i> e <i>in vivo</i>	104
V Conclusões	108
VI Referências	110
VII Apêndice	118
VIII Anexos	122
7.1 Certificado da Comissão de Ética no Uso de Animais	122
7.2 Direitos autorais	123



I INTRODUÇÃO

1 Barreira Hematoencefálica

A barreira hematoencefálica (BHE) é uma barreira seletiva altamente especializada localizada na interface entre o sangue e o cérebro. Sua principal função é manter a homeostasia do sistema nervoso central (SNC) através da regulação do transporte de nutrientes, eletrólitos e metabólitos entre o sangue e o SNC [1].

A figura 1 apresenta uma representação esquemática dos componentes da BHE. **Células endoteliais** de um capilar cerebral cercado por **pericitos** envolvidos por uma densa **membrana basal** e **pés astrocitários**. Em conjunto com os **neurônios**, estes componentes formam a unidade neurovascular [2].

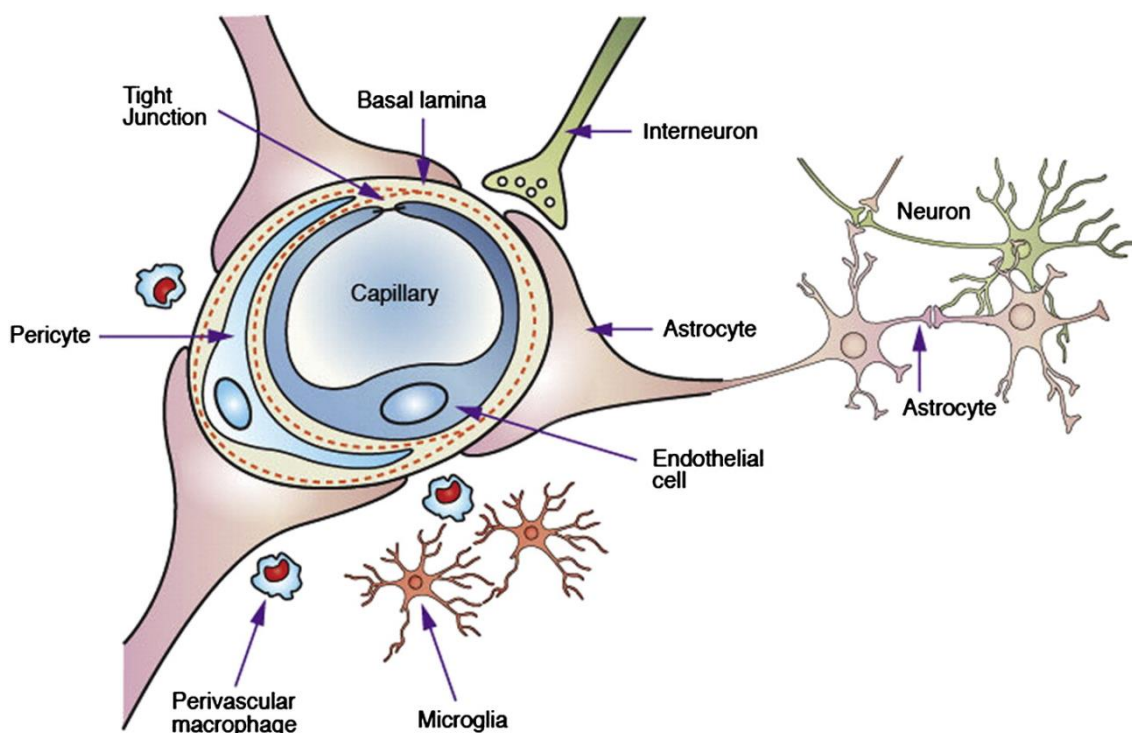


Fig.1 Componentes celulares da barreira hematoencefálica. A BHE é formada por células endoteliais rodeadas por pericitos, lâmina basal e pés astrocitários. O esquema mostra ainda a interação de astrócitos com neurônios e a presença de micróglia. Retirado de [3].

1.1 Unidade Neurovascular

1.1.1 Células endoteliais

As células endoteliais cerebrais apresentam um fenótipo que as faz diferentes das células endoteliais localizadas em outros locais. São células altamente polarizadas que expressam transportadores de influxo e efluxo específicos e são conectadas por junções intercelulares denominadas junções de oclusão (*tight junctions*), junções de adesão (*adherens junctions*) e junções comunicantes (*gap junctions*) (Fig. 2) [4].

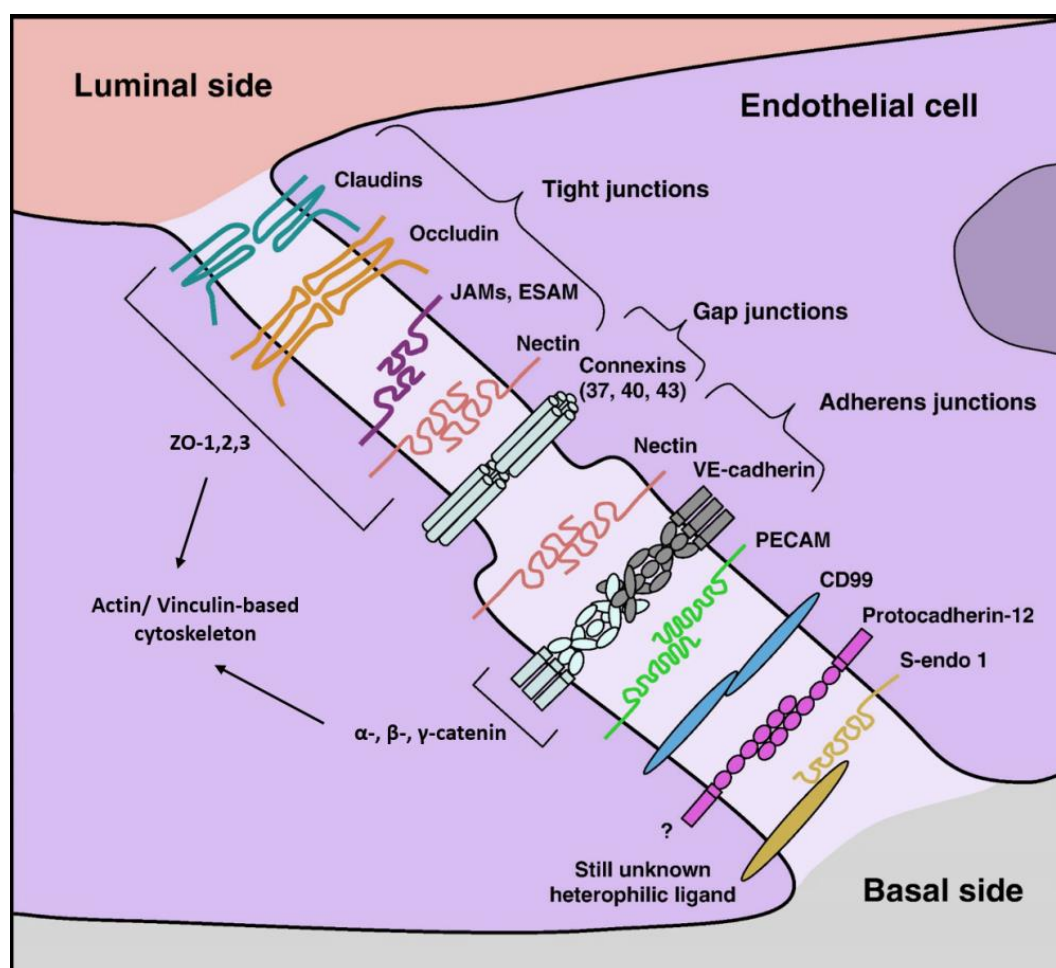


Fig. 2 Componentes moleculares das junções endoteliais. Claudinas, ocludinas, JAM (*Junctional Adhesion Molecules*) e ESAM (*Endothelial Cell-Selective Adhesion Molecules*) estão localizadas nas junções de oclusão; VE-Caderina nas junções de adesão e connexinas nas junções comunicantes. Nectina está presente tanto nas junções de oclusão quanto nas junções de adesão, enquanto PECAM (*Platelet Endothelial Cell Adhesion Molecule*), Protocadherin-12, CD99 e S-endo 1 estão fora destas estruturas. Tanto as junções de oclusão quanto as junções de adesão estão ligadas ao citoesqueleto de actina através de proteínas acessórias da família da ZO (*Zonula occludens*) e cateninas. Adaptado de [5].

As junções de oclusão apresentam duas funções primordiais, a função de barreira que impede a livre passagem de substâncias e a função de “portão” que controla a passagem paracelular de íons e solutos entre as células [6]. São formadas por proteínas integrais de membranas denominadas claudina, ocludina, molécula de adesão juncional e molécula de adesão seletiva à célula endotelial e várias proteínas citoplasmáticas acessórias, destacando-se a *zonula occludens (ZO)*, ZO-1, ZO-2 e ZO-3. Estas proteínas acessórias conectam as proteínas de membrana à actina para a manutenção da integridade estrutural e funcional do endotélio [7].

As junções de adesão executam várias funções incluindo a iniciação e estabilização da adesão celular, regulação do citoesqueleto de actina, sinalização intracelular e regulação da transcrição. São compostas por glicoproteínas transmembrana da superfamília caderina, que interagem com os membros da família das cateninas (α , β e γ). Em conjunto, estas proteínas controlam a formação, manutenção e funções das junções de adesão [8].

As junções comunicantes são canais de baixa resistência responsáveis pela comunicação entre o citoplasma de células adjacentes, permitindo a transferência intercelular de pequenos solutos tais como íons, metabólitos e segundos mensageiros. São constituídas pela união de dois hemicanais protéicos denominados conexons. Um conexon é composto por seis subunidades de proteínas integrais de membrana, as conexinas (Cx). Diferentes regiões do organismo apresentam isoformas distintas de conexinas. Em relação ao SNC, pelo menos 11 isoformas foram detectadas incluindo Cx26, Cx29, Cx30, Cx32, Cx33, Cx37, Cx36, Cx40, Cx43, Cx45, and Cx47 [8]. Entretanto, ainda não foi bem estabelecido quais isoformas estão presentes na BHE. Há um consenso apenas sobre a presença da Cx43 em todos os componentes da unidade neurovascular [9].

1.1.2 Pericitos

Os pericitos são células perivasculares que circundam parcialmente as células endoteliais de capilares e pequenas vênulas. Tanto os pericitos quanto as células endoteliais estão associados a proteínas da matriz extracelular da lâmina basal. Eles são responsáveis pela regulação de várias funções neurovasculares necessárias para a homeostase do SNC incluindo manutenção do fluxo sanguíneo, angiogênese e

estabilidade vascular; clearance de metabólitos tóxicos e manutenção da permeabilidade da BHE e da lâmina basal [10].

Sob condições normais, os pericitos são relativamente quiescentes; entretanto, sob condições estressantes ou lesões, os pericitos sofrem alterações fenotípicas e funcionais que podem incluir migração, proliferação ou diferenciação contribuindo para a patogênese da doença [11].

1.1.3 Lâmina basal

A lâmina basal é uma camada de matriz extracelular composta por colágeno tipo IV, laminina, fibronectina, entactina, trombospondina e várias proteoglicanas [12]. É utilizada como um local de ancoragem e de sinalização para as interações célula-célula [1]. Estas interações podem estimular a expressão de proteínas das junções de oclusão, indicando que, embora essas proteínas constituam a principal barreira para difusão paracelular, as proteínas da lâmina basal estão provavelmente envolvidas na sua manutenção [2].

No SNC, os vasos sanguíneos são envolvidos por uma camada interna (endotelial) e outra externa (parenquimal) de lâmina basal. A lâmina basal endotelial é secretada por células endoteliais e pericitos, que estão envoltos nesta lâmina. Já, a lâmina basal parenquimal é secretada por astrócitos e conecta os pés astrocitários à lâmina basal através de interações proteína-proteína. Dessa forma, o acesso de moléculas e células ao parênquima cerebral requer não apenas a travessia das junções das células endoteliais mas também ambas camadas de lâmina basal [4].

1.1.4 Astrócitos

Os astrócitos são as células gliais mais abundantes do SNC. Apresentam um formato estrelado; núcleo grande, ovoide ou ligeiramente irregular e citoplasma com a proteína ácida fibrilar glial (GFAP, do inglês *glial fibrillary acidic protein*), um filamento intermediário exclusivo dessas células no SNC. De acordo com a morfologia de seus prolongamentos citoplasmáticos e sua localização no SNC podem ser divididos em dois subtipos principais, astrócitos protoplasmáticos e astrócitos fibrosos. Os astrócitos protoplasmáticos são encontrados na substância cinzenta e exibem poucos curtos e espessos prolongamentos que, conseqüentemente, são pouco reativos à marcação com

GFAP. Astrócitos fibrosos são encontrados na substância branca e exibem numerosos longos prolongamentos com aparência clássica “star-like”, que se coram facilmente com GFAP [13].

Várias pesquisas tem demonstrado a importância dos astrócitos na manutenção das propriedades da BHE, tanto em condições normais quanto patológicas. Os astrócitos secretam moléculas que são importantes para a regulação das interações entre os componentes da BHE [14]. Eles fornecem apoio metabólico e estrutural aos neurônios através de redes extensas formadas pelos canais das junções comunicantes, principalmente Cx43 [15].

Os prolongamentos dos pés astrocitários apresentam canais de água (Aquaporina-4) e um canal retificador de potássio (Kir 4.1), que estão envolvidos respectivamente na regulação da passagem de água e potássio para o interior das células [16], contribuindo para manutenção da homeostase do microambiente neural e modulando as transmissões sinápticas. Além disso, os astrócitos produzem moléculas antioxidantes como glutatona, ascorbato e superóxido dismutase e um grande número de fatores de crescimento e neurotrofinas, importantes para a sobrevivência das células cerebrais durante os processos neurodegenerativos [14].

Em casos de injúria cerebral, os astrócitos tornam-se reativos e respondem rapidamente através de um fenômeno denominado astrogliose reativa. Em casos leves e moderados, a astrogliose reativa caracteriza-se por um aumento variável da expressão de GFAP e de outros genes, bem como hipertrofia astrocitária. Enquanto em casos severos, há um aumento acentuado na expressão de GFAP e de outros genes, juntamente com hipertrofia e proliferação astrocitária [17].

1.1.5 Neurônios e interneurônios

Devido aos seus mecanismos de homeostase altamente sofisticados, os neurônios podem ser considerados “the pacemaker” da unidade neurovascular. Os neurônios detectam variações muito pequenas em seu suprimento de nutrientes e oxigênio, e transformam estes sinais em mensagens elétricas e químicas para os interneurônios adjacentes ou astrócitos. Em resposta a estes sinais, mecanismos de ajuste são ativados. Quando necessário, os neurônios se comunicam com os vasos sanguíneos influenciando o tônus vascular e, conseqüentemente, o fornecimento de sangue para a área ao seu redor [18].

Uma das formas de detectar os neurônios e diferenciá-los das demais células do sistema nervoso é utilizar o marcador *Neuronal Nuclei* (NeuN). Desde sua descoberta, NeuN tornou-se um dos marcadores neuronais mais utilizados devido seu amplo padrão de distribuição no sistema nervoso e localização específica no núcleo de neurônios maduros. Entretanto, estudos recentes tem argumentado que a imunoreatividade de NeuN pode variar durante certas doenças e estados fisiológicos exigindo cautela na interpretação dos resultados [19].

O sistema imunológico também desempenha um papel importante no SNC em relação à sobrevivência e morte neuronal. As citocinas podem atuar no SNC como fatores de crescimento neuronal e/ou como neurotoxinas, desempenhando, portanto, um papel importante em diversas doenças neurológicas e trauma cerebral [20].

1.2 Vias de acesso ao SNC através da BHE

Um dos principais desafios no desenvolvimento de agentes terapêuticos para o tratamento de desordens cerebrais é a dificuldade de atravessar a BHE e chegar ao SNC. Como ilustrado na figura 3, há diferentes vias de transporte pelo qual moléculas podem atravessar a BHE, dentre elas:

a) Via paracelular: pequenas moléculas hidrofílicas (< 3 nm) difundem-se passivamente através das junções interendoteliais. Esta via caracteriza-se por alta condutância e baixa seletividade. A permeabilidade da via paracelular é mantida pelo equilíbrio entre a força contrátil gerada no citoesqueleto endotelial e a força adesiva produzida nas junções célula-célula e pelo contato célula-matriz [21].

b) Via transcelular: em geral o transporte transcelular passivo está limitado a pequenas moléculas lipossolúveis que difundem-se através da bicamada lipídica e entram no SNC. Normalmente, estas moléculas apresentam peso molecular < 500 Da, $\log P_{oct}$ entre 2-4 e número de doadores de ligações de hidrogênio menor que 5. São exemplos, pequenas moléculas gasosas (CO_2 e O_2), barbitúricos, etanol e cafeína [22].

c) Proteínas específicas de transporte: utilizadas para o transporte de moléculas essenciais à sobrevivência das células cerebrais. Por exemplo, para o transporte de glicose utiliza-se o transportador de glicose GLUT-1, enquanto aminoácidos são transportados através do

transportador LAT-1. A ligação com a molécula provoca uma alteração conformacional na proteína transportadora, resultando no transporte da molécula para o outro lado da membrana, a favor do gradiente de concentração. Se a molécula necessitar se mover contra o gradiente de concentração, o ATP pode fornecer a energia necessária para facilitar o processo [3, 21].

d) Bombas de efluxo: os transportadores de efluxo, como a glicoproteína-P (P-gp) e as MRPs (*Multidrug Resistance-Associated Proteins*), realizam a retirada de metabólitos tóxicos a partir do cérebro e impedem a entrada de compostos potencialmente neurotóxicos provenientes do sangue. São um dos principais obstáculos para o acúmulo de uma vasta gama de moléculas biologicamente ativas no cérebro [3, 21].

e) Transcitose mediada por receptor: as células endoteliais do cérebro apresentam receptores para transferência de moléculas hidrofílicas maiores e essenciais, tais como hormônios, fatores de crescimento, ferro, insulina e lipoproteínas. A ligação do ligante no receptor resulta em endocitose, seguida da internalização da vesícula endocítica até a superfície oposta e exocitose [23].

f) Transcitose adsorptiva: é provocada por uma ligação eletrostática entre moléculas carregadas positivamente e a superfície da membrana plasmática que é carregada negativamente. Esta interação induz a formação de vesículas com posterior internalização e exocitose [23].

g) Transcitose mediada por células: trata-se de um mecanismo conhecido como "cavalo de Tróia". Esta rota de transporte depende de células do sistema imunológico para atravessar a BHE sem danificá-la. Ao contrário das vias de transporte mencionadas acima, que normalmente permitem a passagem apenas de moléculas com propriedades específicas, a transcitose mediada por células é única na medida em que pode ser utilizada praticamente por qualquer tipo de molécula ou material, bem como sistemas de carreadores particulados [3].

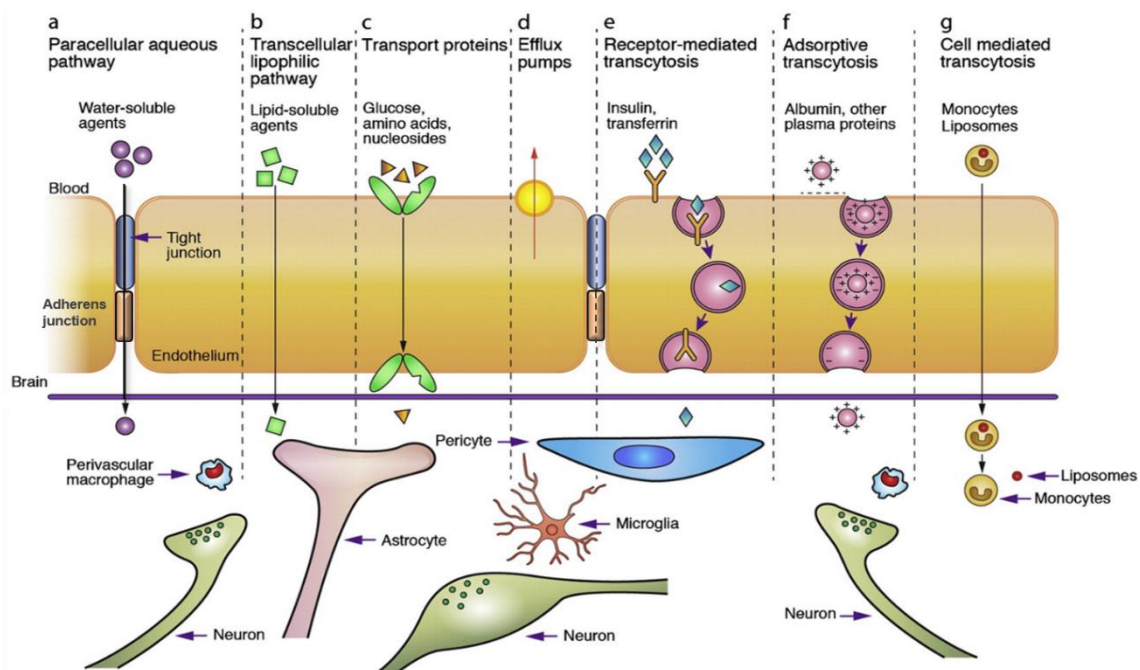


Fig. 3 Vias de acesso ao SNC através da BHE. As vias de transporte “a - f” são comumente utilizadas por solutos, enquanto a via “g” envolve monócitos, macrófagos e outras células do sistema imune e pode ser utilizada por qualquer fármaco livre ou mesmo incorporado em lipossomas ou nanopartículas. Retirado de [3].

1.3 Estratégias para a entrega de fármacos através da BHE

Considerando as características da BHE, nota-se que a entrega de fármacos para o SNC é algo extremamente complexo. Durante as últimas décadas, múltiplas estratégias vem sendo desenvolvidas para contornar os obstáculos e desenvolver terapias mais eficazes para o tratamento de desordens neurológicas (Fig. 4).

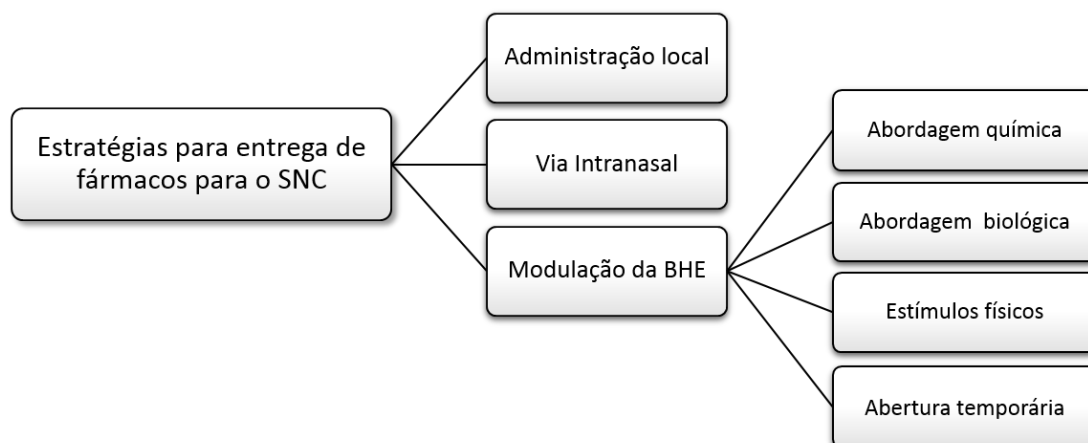


Fig. 4 Estratégias para entrega de fármacos para o SNC.

1.3.1 Administração local

A maneira mais direta de contornar a BHE é entregar os fármacos diretamente no local alvo dentro do SNC. Através de implantes ou injeções em bolus intermitentes, é possível maximizar a quantidade de fármaco que atinge o tecido alvo com mínima exposição do tecido saudável circundante. Dessa forma, há redução dos efeitos colaterais que a presença do fármaco na circulação sistêmica provocaria. Trata-se de uma importante estratégia para o tratamento de tumores cerebrais, uma vez que os agentes quimioterápicos são substâncias extremamente tóxicas [24, 25].

1.3.2 Administração via intranasal

A administração intranasal é uma via alternativa para a entrega de fármacos ao SNC já que permite o acesso direto ao cérebro sem a participação da BHE. Uma vez que o fármaco atravessa o epitélio, ele difunde-se através do nervo olfatório e/ou do trigêmeo, distribuindo-se por todo o cérebro (Fig. 5) [26].

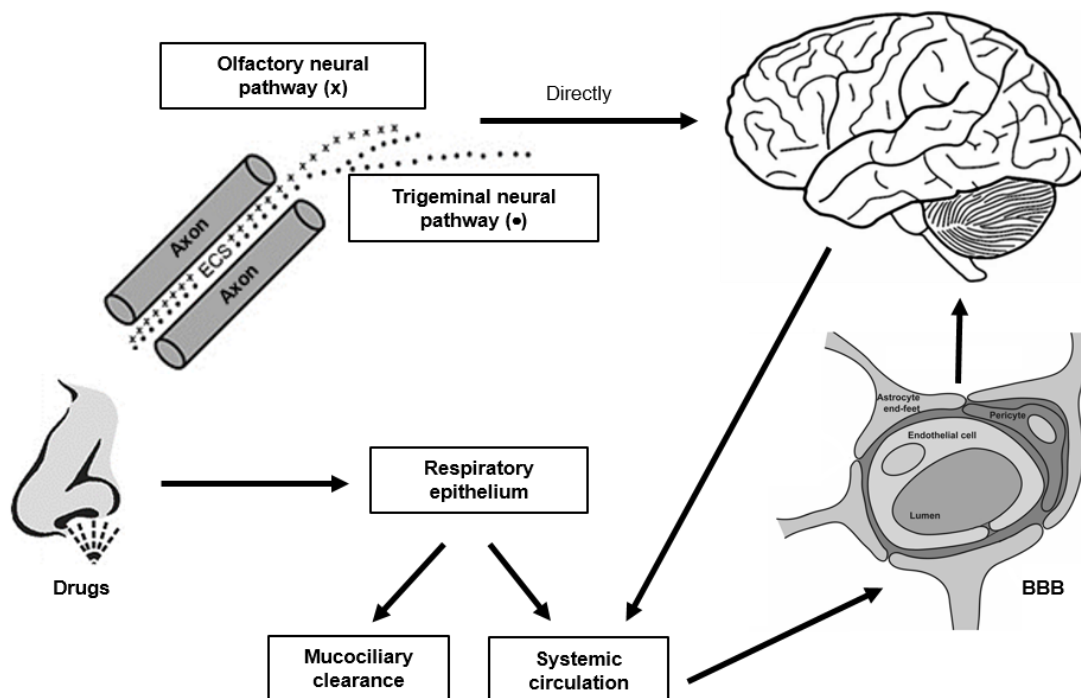


Fig. 5 Representação esquemática das possíveis vias envolvidas no transporte de drogas do nariz ao cérebro e à corrente sanguínea sistêmica.

Como a via de administração intranasal é um método seguro e eficaz, muitas formulações vem sendo desenvolvidas, diversas patentes já foram registradas [27] e algumas formulações já estão presentes no mercado [28]. Entretanto, há algumas limitações para o uso da administração intranasal. Por exemplo, concentrações diferentes podem ser obtidas em diferentes regiões do cérebro e da medula espinal. A eficiência da entrega do fármaco tende a diminuir com o aumento do seu peso molecular. Além disso, se houver irritações na mucosa nasal esta via deve ser evitada [24].

1.3.3 Modulação da BHE

Nas últimas duas décadas, houve um aumento gradual do conhecimento e compreensão das moléculas envolvidas nas junções de oclusão e adesão e, em paralelo, a descoberta de que moduladores poderiam ser utilizados para realizar a abertura da BHE, variando desde substâncias químicas e biológicas à estímulos físicos. A base racional para a modulação da abertura das junções de oclusão baseia-se no fato de que sua abertura é um fenômeno associado a muitas doenças cerebrais e muitos moduladores já foram caracterizados; esta modulação pode permitir a passagem através da BHE tanto de pequenas moléculas hidrossolúveis quanto de macromoléculas incluindo sistemas de entrega de drogas, tais como lipossomos, nanopartículas, micelas, conjugados de polímeros; a utilização de estímulos físicos, tal como ultrassons, proporcionam uma permeabilização local temporária da BHE, permitindo, portanto, a entrega de fármacos em locais específicos de forma não invasiva [3].

Abordagem química

A abordagem química mais comum de entrega de drogas no SNC é a utilização de **pró-fármacos**. Os pró-fármacos são definidos como compostos que necessitam de biotransformação prévia antes de se tornarem um agente farmacológico ativo. Eles foram desenvolvidos de modo a melhorar as propriedades físico-químicas, farmacêuticas e/ou farmacocinéticas de compostos farmacologicamente potentes. Três estratégias básicas têm sido utilizadas para facilitar o transporte de pró-fármacos para o SNC: (i) aumento da difusão passiva através da conversão de grupos funcionais não-polares em grupos polares, a chamada lipidação de moléculas; (ii) aumento do transporte mediado por proteínas específicas ou receptores endógenos, e (iii) diminuição do efluxo do fármaco a partir do

cérebro para o sangue. A fim de atingir doses terapêuticamente eficazes no SNC, o processo de biotransformação do pró-fármaco deve ser lento nos tecidos periféricos e rápido no cérebro. Além disso, tendo em conta a complexidade anatômica do SNC, a biotransformação deve ser limitada a certas estruturas cerebrais [29].

A diminuição do efluxo do fármaco a partir do cérebro para o sangue pode ser obtida através da **modulação das bombas de efluxo** expressas nas células endoteliais dos capilares cerebrais. Dentre todas as bombas de efluxo, a P-gp transporta o maior número de fármacos comumente utilizados (medicamentos anticancerígenos, antibióticos, antieméticos, antiepilépticos, esteróides, entre outros) e é, portanto, o alvo mais óbvio para modulação. Os mecanismos pelos quais a atividade da P-gp na BHE podem ser moduladas incluem inibição direta por inibidores específicos, modulação funcional e modulação transcricional. Cada mecanismo tem o potencial de reduzir a função de P-gp seletivamente e, por conseguinte, aumentar a permeabilidade no cérebro de fármacos que são substratos de P-gp [30].

Abordagem biológica

Abordagens biológicas para entrega de fármacos no SNC emanam principalmente da compreensão das nuances fisiológicas e anatômicas dos sistemas de transporte através da BHE. Segundo Chen & Liu [3], o melhor sistema é aquele que possa satisfazer as seguintes características:

- A superfície do fármaco deve ser quimicamente modificada. Deve apresentar um dispositivo capaz de interagir com as proteínas, receptores ou células apresentados na superfície da BHE e assim facilitar a absorção do fármaco;
- O fármaco pode ser encapsulado em um sistema de entrega de droga com superfície modificada, tal como lipossomas ou **nanopartículas**.
- O sistema de entrega do fármaco deve ser não imunogênico, a menos que tem como alvo os monócitos/macrófagos.
- O alvo deve ser um receptor específico, reduzindo assim os potenciais efeitos colaterais e aumentando a eficiência do transporte;
- Todos os sistemas devem possuir tamanho específico, para que as suas propriedades sejam uniformes e consistentes e o seu destino biológico possa ser controlado.
- O revestimento com polímeros, tal como polietilenoglicol (PEG), pode prolongar o tempo de circulação do sistema de entrega.

Estímulos físicos

Desde a década de 1950, evidências demonstram a capacidade do **ultrassom** em provocar a abertura da BHE. Entretanto, nessa época, para atingir a energia suficiente para produzir efeitos no cérebro era necessária a realização de uma craniotomia. Um progresso importante foi obtido quando microbolhas de gás foram introduzidas no fluxo sanguíneo antes da exposição ao ultrassom, permitindo que a BHE fosse transientemente (6 a 24 horas) aberta no foco do ultrassom, sem dano neuronal agudo. Assim, a introdução de núcleos de cavitação na corrente sanguínea reduziu a intensidade necessária para produzir a abertura da BHE, facilitando a aplicação da técnica uma vez que não era mais necessária a realização de craniotomia, e diminuindo o risco de danos aos tecidos [31, 32].

Abertura temporária

A injeção intra-arterial de **soluções hiperosmóticas** tais como manitol e arabinose, tem sido utilizada clinicamente para facilitar a entrada de fármacos no cérebro. Estas soluções provocam retração das células endoteliais por puxar osmoticamente a água para fora da célula, o que resulta no desacoplamento dos domínios extracelulares das proteínas das junções de oclusão e, conseqüentemente, sua abertura temporária. Este método produz uma abertura transiente e difusa da BHE, permitindo a entrega de diversas substâncias terapêuticas [33]. Embora tal abordagem seja utilizada clinicamente como um instrumento eficaz para a entrega de fármacos para grandes regiões do cérebro, trata-se de um procedimento um pouco mais invasivo que pode exigir anestesia geral, e levar a efeitos colaterais graves, como convulsões, bradicardia e hipotensão [31].

Destacamos também a ação de alguns **excipientes farmacêuticos** sobre a BHE. Um dos excipientes farmacêuticos mais utilizados, o dodecil sulfato de sódio, induz um extenso, mas reversível, extravasamento de azul de Evans e de ácido α -aminoisobutírico (25-100 $\mu\text{g}/\text{kg}$) em ratos [34]. Isto não é surpreendente considerando que o dodecil sulfato de sódio é um tensoativo aniônico que pode interagir com os lípidos ou proteínas na membrana celular. Outros excipientes como etanol, glicerol e dimetilsulfóxido (DMSO) em concentrações maiores que 1 g/kg são capazes de induzir abertura da BHE. A administração de 0,2 ml de uma solução 50% de etanol ou DMSO em um camundongo de 25 g é equivalente a uma dose de 4 g/kg. Baixas doses (3 mg/kg) de

polissorbato-80 (Tween-80) já são capazes de induzir a abertura da BHE, permitindo a passagem de neuropeptídeos que anteriormente não eram capazes de atravessar a BHE [35].

Alguns **compostos vasoativos**, incluindo prostaglandinas, leucotrienos, bradicinina e histamina, podem aumentar seletivamente a permeabilidade de capilares cerebrais em estados patológicos. Capilares cerebrais normais tendem a resistir aos efeitos destes compostos por meio de uma "barreira enzimática" que inativa-os. Em contraste, esta barreira enzimática é perdida em certos estados patológicos, permitindo que os compostos vasoativos aumentem seletivamente a permeabilidade dos capilares anormais. Clinicamente, a infusão intracarotídea de agentes vasoativos pode aumentar a quantidade de fármaco que chega ao tecido doente. Ao contrário do uso de soluções hiperosmóticas, este é um método menos invasivo e, possivelmente, uma técnica mais confiável já que afeta principalmente a vasculatura [23].

Outro agente utilizado no passado para abrir temporariamente as junções de oclusão foi o **Cereport** (RMP- 7 ou labradimil), um agonista seletivo do receptor B2 de bradicinina. Cereport aumenta seletivamente a absorção do fármaco no tumor cerebral sem provocar efeitos adversos nas áreas não permeabilizadas do cérebro, uma vez que não apresentava toxicidade por si só. Apesar dos resultados positivos obtidos nos modelos animais e na fase I dos ensaios clínicos, os resultados da fase II foram inconsistentes. Houve atividade significativa em pacientes com glioma maligno recorrente após radioterapia, ao passo que, foi ineficiente em gliomas infantis de alto grau de malignidade e gliomas do tronco cerebral. Isso destaca o desafio de traduzir a pesquisa experimental em terapia clínica [36, 37].

Embora estas abordagens sejam benéficas para o tratamento de tumores e outras desordens cerebrais, elas podem trazer riscos adicionais, pois enquanto a BHE permanece aberta outras substâncias potencialmente danosas podem ter acesso ao SNC. Dessa forma, a utilização de qualquer uma das abordagens citadas anteriormente requer uma análise toxicológica completa, tanto da substância isolada quanto dos efeitos que ela pode causar em órgãos vitais do organismo.

2 Nanomateriais

Dentre todas as estratégias peculiares descritas no item anterior, uma delas vem se destacando nos últimos anos, a utilização de nanomateriais. A Comissão Europeia

estabeleceu em 2011 a recomendação 2011/696/UE, definindo nanomateriais como um material de origem natural ou manufaturado, que contém partículas num estado desagregado, agregado ou aglomerado, e em cuja distribuição número-tamanho 50% ou mais das partículas apresentem uma ou mais dimensões externas entre 1 e 100 nanómetros [38].

O mercado mundial de nanomateriais têm apresentado crescimento extremamente rápido. Diferentes tipos de nanomateriais vêm sendo descobertos a cada dia. Produtos nanotecnológicos já estão presentes em vários aspectos do nosso cotidiano: nossos carros, casas, eletroeletrônicos, medicamentos e até alimentos. Estima-se que 11 milhões de toneladas de nanomateriais são produzidas anualmente, representando um valor de mercado de 20 bilhões de euros [39].

2.1 Grafeno e nanomateriais da família do grafeno

O **grafite** é um dos materiais naturais mais antigos e mais amplamente utilizados no mundo. Nas últimas duas décadas, com a valorização da nanotecnologia e o desenvolvimento de novas técnicas de fabricação, os nanomateriais progrediram imensamente e o grafite agora está sendo amplamente utilizado como material de partida para projetar outros tipos de nanomateriais à base de carbono, incluindo os nanotubos de parede única ou múltiplas, fulerenos, nanodiamantes e grafeno (Fig. 6) [40].

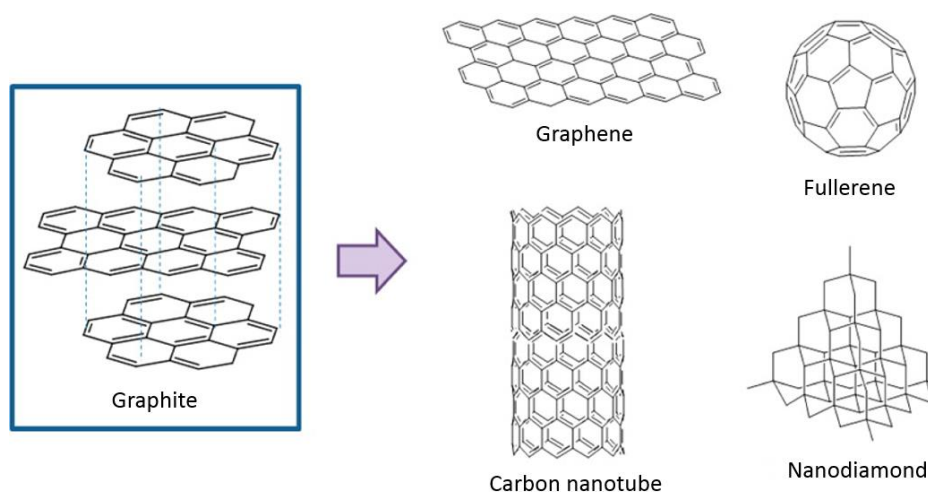


Fig. 6 Vários tipos de nanomateriais à base de carbono - grafeno, nanotubos de carbono, fulerenos e nanodiamantes. Adaptado de [40].

Grafeno é o nome dado a uma monocamada plana de átomos de carbono fortemente empacotados com hibridização sp^2 em uma estrutura bidimensional (2D) hexagonal, semelhante a uma colmeia [41].

Trata-se do mais fino e mais forte material já visto no universo. Sua estrutura bidimensional com conjugação π confere ao grafeno extraordinárias propriedades físicas, incluindo grande área teórica específica ($2.630 \text{ m}^2 \text{ g}^{-1}$), alto módulo de Young ($\sim 1,0 \text{ TPA}$) e elasticidade, inigualável eletrividade e condutividade térmica ($\sim 5000 \text{ Wm}^{-1}\text{K}^{-1}$); além de propriedades eletrônicas fascinantes, tais como campo elétrico ambipolar e condução balística. Sua propriedades eletrônicas, ópticas, magnéticas, térmicas e mecânicas únicas tornaram o grafeno um excitante candidato para aplicação em sensores; transistores; filmes finos, transparentes e condutores; dispositivos de geração e armazenamento de energia [42].

Apesar da vasta gama de aplicações, o grafeno apresenta duas grandes desvantagens. Uma delas é a dificuldade de produção em larga-escala de folhas de grafeno de alta qualidade. A outra é que o grafeno não é dispersível em soluções aquosas e diversos solventes orgânicos. Ele tende a formar aglomerados irreversíveis devido as interações van der Waals e empilhamento π - π . Como resultado, a conjugação do grafeno com fármacos ou componentes biológicos é extremamente desafiadora [43].

Neste contexto, o uso de outros nanomateriais a base de grafeno tem recebido bastante atenção. Com base no número de camadas e na modificação química realizada, os nanomateriais da família do grafeno classificam-se em grafeno de poucas ou múltiplas camadas, óxido de grafeno e óxido de grafeno reduzido [44], todos possuindo propriedades diferentes entre si.

O **óxido de grafeno** é a forma oxidada do grafite (Fig. 7). Pode ser caracterizado como uma monocamada grafítica com regiões aromáticas (átomos de carbono sp^2) e alifáticas (átomos de carbono sp^3) contendo grupos funcionais hidroxila e epóxi em seu plano basal e carbonila e carboxila em suas bordas [45, 46].

É importante mencionar que a presença de tais grupos funcionais podem afetar de forma significativa as propriedades mecânicas, eletrônicas e eletroquímicas do óxido de grafeno e, portanto, modificar seu desempenho em diversas aplicações. Comparado com grafeno pristino (sem defeitos), a presença destes grupos funcionais proporcionam uma grande vantagem, tornam o óxido de grafeno fortemente hidrofílico. Isto confere boa capacidade de dispersão em muitos solventes, especialmente em água ($6,6 \text{ } \mu\text{g/ml}$). Por outro lado, os grupos funcionais oxigenados do óxido de grafeno podem dar origem

a defeitos estruturais notáveis, concomitante com alguma perda de condutividade elétrica. [47, 48]. Assim, dependendo da aplicação vislumbrada para o óxido de grafeno, uma etapa de redução é necessária para restaurar a sua condutividade elétrica.

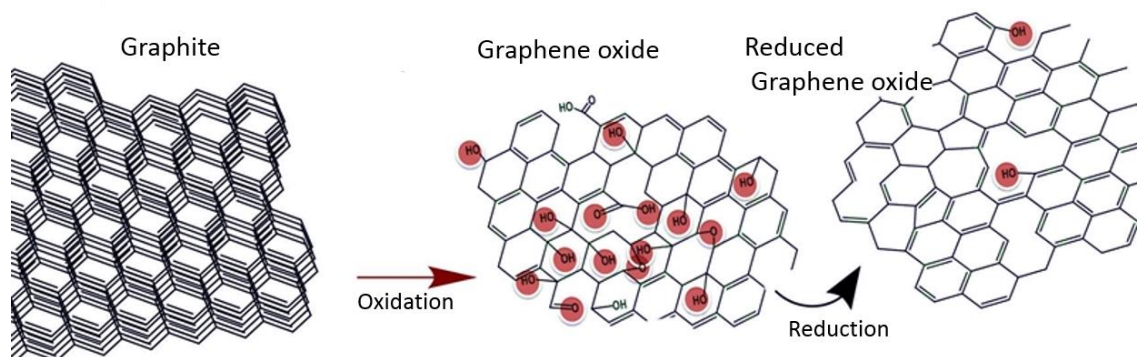


Fig. 7 Síntese do óxido de grafeno reduzido a partir do grafite. Adaptado de [49].

Esta etapa pode ser feita por tratamento térmico ou por tratamento químico com agentes redutores como hidrazina; hidretos de metal (hidreto de sódio, boro-hidreto de sódio, hidreto de alumínio); vitamina C; ácido iodídrico; hidroquinona; ureia e soluções alcalinas fortes (KOH e NaOH) [50].

O grau de redução obtido é dependente do processos de redução utilizado e influencia significativamente as propriedades físicas do nanomaterial. Com a redução do óxido de grafeno, há formação de um produto mais semelhante ao grafeno - o **óxido de grafeno reduzido** (Fig. 7). Ambos nanomateriais apresentam estrutura e propriedades elétricas, térmicas e mecânicas similares, apesar de ser impossível reduzir totalmente o óxido de grafeno e grupos funcionais epóxi e hidroxila residuais permanecerem no plano basal do óxido de grafeno reduzido [51]. Entretanto, a presença desses grupos funcionais confere uma hidrofobicidade maior ao óxido de grafeno reduzido (4.74 $\mu\text{g/mL}$) quando comparado ao grafeno [48], beneficiando sua aplicação nas áreas biomédicas.

2.2 Funcionalização

A fim de melhorar a dispersão e estabilidade de materiais à base de grafeno em meio fisiológico, pode-se realizar uma funcionalização na superfície do nanomaterial. Existem duas formas de funcionalização: não covalente e covalente.

A funcionalização não covalente baseia-se em interações fracas do tipo van der Waals e interações π - π entre o grafeno e seus derivados com um ligante, tal como

moléculas orgânicas e polímeros. Normalmente, as forças van der Waals ocorrem entre o grafeno e moléculas orgânicas ou polímeros com caráter altamente hidrofóbico, enquanto as interações π - π são comuns entre o grafeno e moléculas com sistema π altamente estendido. Devido a presença de grupos oxigenados na superfície basal e bordas do óxido de grafeno e, em menor quantidade, do óxido de grafeno reduzido, interações iônicas e ligações de hidrogênio estão sempre envolvidas [52].

A manipulação e o processamento da funcionalização não covalente são mais difíceis quando comparados à funcionalização covalente, entretanto apresenta a vantagem de preservar propriedades importantes tais como a condutividade elétrica e resistência mecânica, uma vez que o sistema π e a estrutura das ligações sp^2 não são afetados [52].

A funcionalização covalente do grafeno baseia-se em duas vias gerais: (i) formação de ligações covalentes entre radicais livres e dienófilos e ligações C=C do grafeno pristino e (ii) formação de ligações covalentes entre os grupos funcionais de pequenas moléculas e polímeros com os grupos funcionais oxigenados disponíveis no plano basal e bordas do óxido de grafeno e óxido de grafeno reduzido [46].

Um dos métodos mais comuns de funcionalização covalente é a introdução de aminas. Foi demonstrado que a adição de longos grupos amina alifáticos aumenta a capacidade de dispersão do grafeno em solventes, permitindo sua aplicação em biodispositivos e como carreador de fármacos. Do mesmo modo, aminas primárias funcionalizadas com porfirina e aminas secundárias funcionalizadas com fulereno têm sido anexadas ao óxido de grafeno, obtendo-se materiais com excelente desempenho óptico não linear [53].

Além de moléculas pequenas, polímeros também têm sido ligados à superfície do óxido de grafeno. Estas ligações são tipicamente realizadas pelos métodos “grafting to” e “grafting from”.

No método “grafting to”, o primeiro passo é a síntese de um polímero com propriedades específicas. Através da modificação do sítio ativo, estes polímeros ligam-se preferencialmente aos grupos funcionais disponíveis na superfície do óxido de grafeno/óxido de grafeno reduzido. Normalmente, uma cadeia de polímeros com porções amino-terminal e hidroxila-terminal são ligadas através de amidação ou esterificação com os grupos carboxila da superfície do óxido de grafeno/óxido de grafeno reduzido. Já, no método “grafting from” a ordem é inversa à anterior. Primeiro fixa-se a cadeia contendo o monômero funcional na superfície do nanomaterial, ou seja, realiza-se a polimerização de monômeros a partir de macro-iniciadores derivados da superfície do

grafeno ou dos grupos hidroxilas e carboxila do óxido de grafeno/óxido de grafeno reduzido. Ao contrário do método “grafting to”, este método permite que polímeros com alto peso molecular sejam ligados à superfície do nanomaterial [54].

2.3 Nanomedicina

A descoberta do grafeno abriu uma nova área de investigação e suas potenciais aplicações tornaram-se objeto de intensa investigação. Suas principais características físico-químicas e aplicações em medicina estão ilustradas na figura 8.

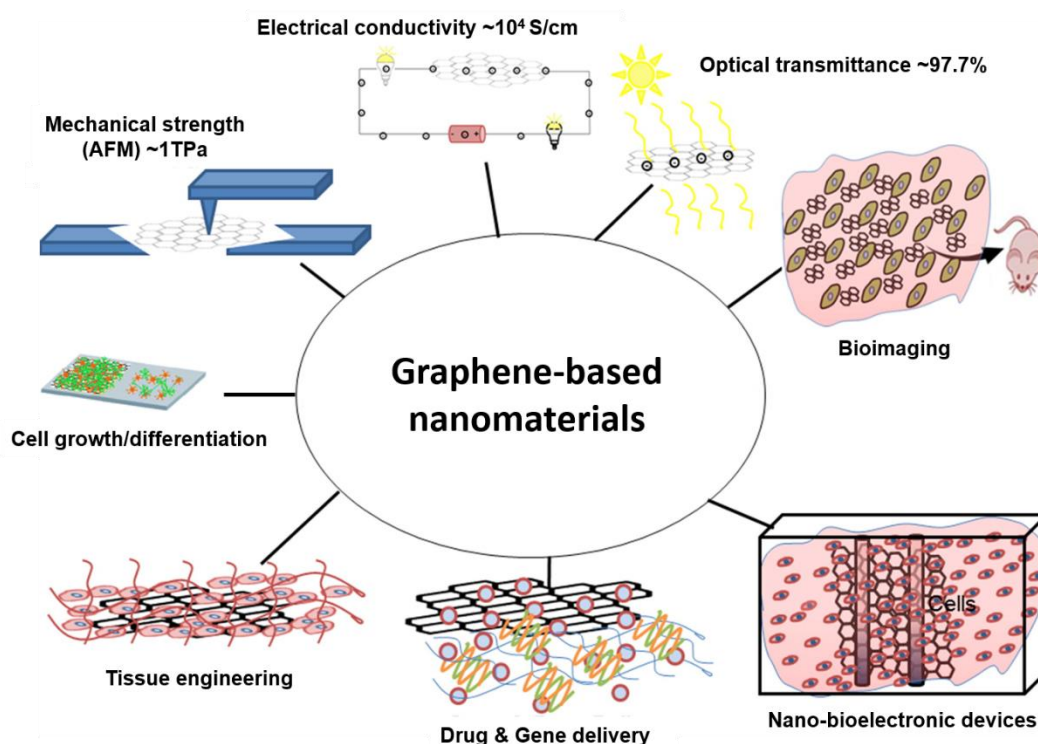


Fig. 8 Representação esquemática das principais características físico-químicas e das várias aplicações biológicas dos nanomateriais da família do grafeno. Adaptado de [44].

2.3.1 Biosensores

Recentemente, a maioria dos estudos eletroquímicos envolvendo materiais a base de grafeno tem sido realizados utilizando o óxido de grafeno reduzido, uma vez que trata-se de um nanomaterial abundante que apresenta baixo custo de produção [55].

É o nanomaterial da família do grafeno que apresenta as melhores características para detecção de serotonina: alta sensibilidade, boa seletividade e estabilidade, baixo limite de detecção e tempo de resposta rápido [56]. Também tem apresentado resultados promissores na detecção de insulina [57] e após funcionalização, tem sido eficaz na detecção de tirosina (hemin-rGO) [58], catecol (PEDOT-rGO-Fe₂O₃-PPO) [59] e peróxido de hidrogênio (rGO/Au₂O₃) [60].

2.3.2 Crescimento e diferenciação de células

Devido a (sub)organização celular do SNC e os nanomateriais à base de carbono compartilham algumas semelhanças morfológicas e funcionais, vários grupos de pesquisa começaram explorar o uso desses nanomateriais no campo da neurociência [61]. O grafeno e seus derivados vem sendo utilizados como substrato para crescimento e diferenciação de células-tronco em neurônios, astrócitos e oligodendrócitos tanto *in vitro* [62] quanto *in vivo* [63].

Além disso, a capacidade do óxido de grafeno em estimular a diferenciação de células-tronco mesenquimais em adipócitos e células-tronco pluripotentes em linhagem endodérmica também foi demonstrada. Também foi relatado que *scaffolds* de grafeno são bons substratos para indução de formação óssea e diferenciação cardiomiogênica a partir de células-tronco mesenquimais humanas [64].

2.3.3 Engenharia de tecidos

O campo da engenharia de tecidos envolve a reparação, regeneração e substituição de tecidos e órgãos lesionados. Para alcançar este objetivo, os tecidos artificiais devem possuir características-chave como guiar o crescimento celular, carrear moléculas bioativas, gerar sinais físicos e químicos, e estimular propriedades mecânicas do tecido receptor. No entanto, cada tecido apresenta diferentes propriedades mecânicas, elétricas e físicas. Portanto, o uso de materiais com múltiplos componentes que possam abordar grande parte dos requisitos citados acima vem sendo amplamente utilizados para a fabricação de tecidos artificiais [65].

Os materiais à base de grafeno são um dos nanomateriais mais versáteis devido às suas propriedades físicas e químicas excepcionais. Além disso, eles podem interagir com outras biomoléculas tais como o DNA, enzimas, proteínas, peptídeos e uma

variedade de materiais bioativos tornando-se excelentes candidatos para aplicação em medicina regenerativa e engenharia de tecidos. Em particular, os materiais à base de grafeno vem sendo utilizados com sucesso na engenharia de tecidos cardíacos, neurais, ósseos, cartilagens, músculos esqueléticos e de tecido adiposo da pele [65].

2.3.4 Entrega de fármacos e genes

Área superficial específica elevada, empilhamento π - π , interações eletrostáticas, são algumas das características dos nanomateriais a base de grafeno que vem sendo exploradas para o carregamento de diferentes agentes terapêuticos como siRNA, DNA, anticorpos, proteínas, genes e fármacos [44].

Grande parte dos estudos concentram-se na entrega de agentes quimioterápicos, principalmente doxorrubicina, para o tratamento de câncer de mama, câncer cervical e câncer hepático. Outros tipos de câncer como linfoma, câncer de colón, próstata, pulmão, pele, gliomas e glioblastomas também foram estudados utilizando diferentes fármacos conjugados com grafeno, óxido de grafeno ou óxido de grafeno reduzido [66].

O sucesso dos sistemas de entrega de fármacos baseados na nanotecnologia é dependente de três fatores. O primeiro é a construção de um carreador com alta capacidade de carregamento. O segundo é construir um sistema que seja capaz de liberar o fármaco de forma controlada e em um local específico. Para esta finalidade, a estratégia normalmente utilizada é a conjugação do carreador com ligantes que possuem reconhecimento específico, como a transferrina. Por último, é necessário confirmar a biocompatibilidade e toxicidade do sistema, um pré requisito fundamental antes da realização de testes pré-clínicos [67].

2.4 Nanotoxicidade

Nas últimas décadas, com o surgimento da nanotecnologia e o crescimento exponencial do uso de nanomateriais em produtos de diversos segmentos industriais, médicos e biotecnológicos, uma nova subárea surgiu, a nanotoxicologia [68].

A determinação da toxicidade de um nanomaterial é dependente das suas características físico-químicas, dose, via de administração e tempo de exposição [69].

Neste contexto, um importante ponto a ser destacado, é a dificuldade de comparação entre os resultados dos estudos toxicológicos de nanomateriais, devido não apenas à grande variedade de métodos de síntese, mas também à falta de trabalhos sistemáticos relatando uma adequada caracterização físico-química do nanomaterial utilizado no estudo. Soma-se a isso, ainda, a ausência mundial de regulamentações e protocolos que estabeleçam quais metodologias devem ser utilizadas para avaliações nanotoxicológicas [4, 70].

Normalmente, o primeiro *screening* toxicológico de novos nanomateriais é realizado a nível celular (*in vitro*) e posteriormente são realizados testes utilizando animais (*in vivo*). Os estudos *in vivo* fornecem resultados mais próximos para determinação da equivalência terapêutica em humanos, uma vez que os testes *in vitro* ainda não são capazes de contemplar importantes aspectos como biodistribuição, metabolização, excreção, e a influência dos nanomateriais sobre o sistema imunológico [71].

Diversas publicações abordando a toxicidade dos nanomateriais à base de grafeno utilizando modelos celulares e animais estão disponíveis [72-75]. Não é possível dar uma resposta clara à questão se os nanomateriais da família do grafeno são seguros ou tóxicos, mas há fortes evidências de que os efeitos tóxicos são particulares de cada nanomaterial. Além disso, uma generalização sobre a toxicidade dos nanomateriais da família do grafeno deve ser evitada pois os riscos associados com estes nanomateriais são dependentes do processo de desenvolvimento do nanomaterial e das aplicações específicas avaliadas [72].

Basicamente, dependendo das suas dimensões, os nanomateriais à base de grafeno podem ser internalizados por diferentes mecanismos (Fig. 9). Após internalização, estudos tem relatado que estes nanomateriais podem induzir estresse oxidativo, aumentando a produção de espécies reativas de oxigênio (EROs), o que pode gerar mudanças no potencial da membrana mitocondrial, danos no DNA e liberação de citocinas pró-inflamatórias. Como consequência do estresse oxidativo, inflamação e danos no DNA pode ocorrer morte celular programada ou apoptose. Além disso, os nanomateriais à base de grafeno podem atuar como receptores de elétrons inibindo assim a cadeia de transporte de elétrons e diminuindo o nível de ATP [75].

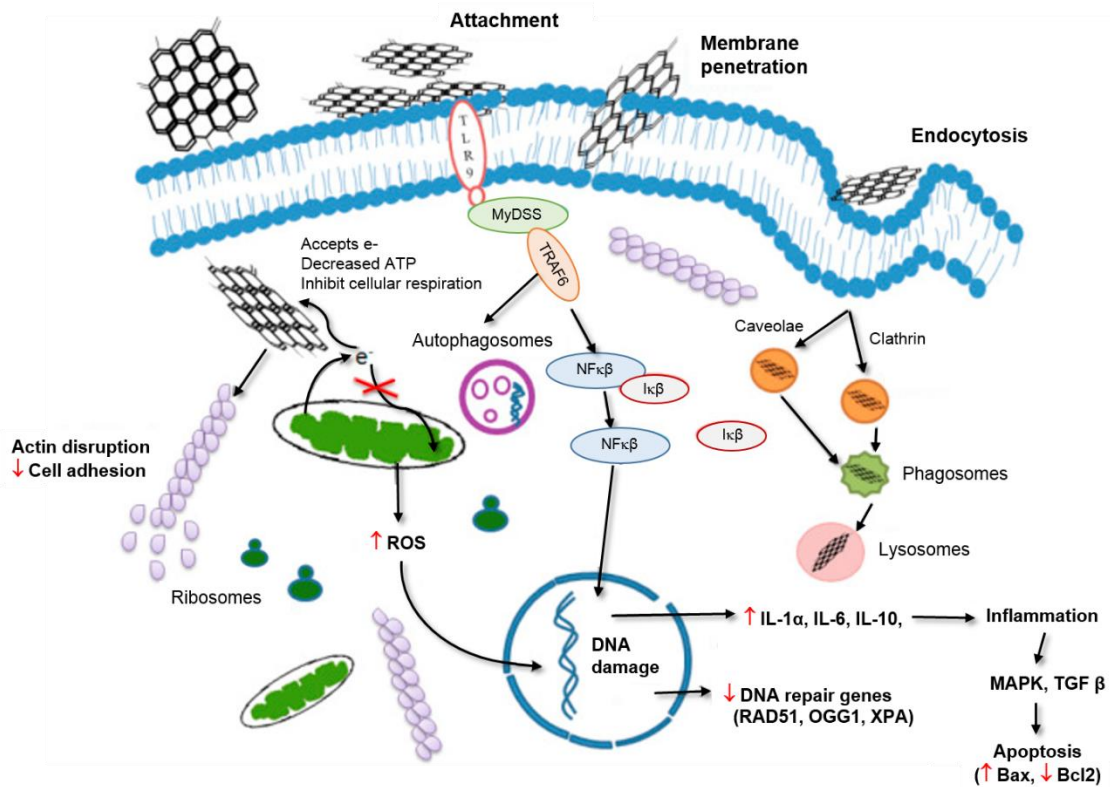


Fig. 9 Mecanismo de toxicidade dos nanomateriais da família do grafeno. Adaptado de [75].



II OBJETIVOS

2 Objetivo geral

O presente trabalho se propôs a investigar os efeitos do óxido de grafeno reduzido no sistema nervoso central, em particular, na BHE de ratos Wistar adultos, assim como determinar seu perfil nanotoxicológico.

2.1 Objetivos específicos

- a) Caracterizar os nanomateriais quanto aos seus aspectos físico-químicos.
- b) Determinar a distribuição do nanomaterial no parênquima cerebral, 15 minutos, 1 hora, 3 horas e 7 dias após injeção sistêmica única de rGO.
- c) Avaliar a integridade da BHE utilizando o corante azul de Evans e microscopia eletrônica de transmissão.
- d) Avaliar os mecanismos relacionados ao transporte de substâncias através da BHE envolvendo a via paracelular, controlada pelas junções interendoteliais; a via transcelular, uma rota de transporte vesicular; o transporte por proteínas (influxo de glicose) e a influência sobre a bomba de efluxo P-gp.
- e) Avaliar *in vivo* a toxicidade aguda e subcrônica de rGO.
- f) Avaliar os efeitos da pegulação sobre funcionalidade e toxicidade de rGO *in vitro* e *in vivo*.



III CAPÍTULOS

Esta dissertação está baseada na informação CCPG/001/98 UNICAMP que regulamenta o formato alternativo para dissertações e teses e permite a inserção de artigos científicos de autoria ou co-autoria do candidato.

Desta forma, esta dissertação é composta de três artigos, os quais foram publicados e submetidos para publicação, conforme descrito abaixo:

Capítulo I - Reduced graphene oxide induces transient blood-brain barrier opening: an *in vivo* study. J Nanobiotechnology. 2015; 13: 78. doi: 10.1186/s12951-015-0143-z.

Capítulo II - Reduced graphene oxide: nanotoxicological profile. J Nanobiotechnology. 2016; 14: 53. doi: 10.1186/s12951-016-0206-9.

Capítulo III - PEGylation of reduced graphene oxide enhanced toxicity in blood-brain barrier components: *in vitro* and *in vivo* studies.

Capítulo I

Mendonça et al. *J Nanobiotechnol* (2015) 13:78
DOI 10.1186/s12951-015-0143-z



RESEARCH

Open Access



Reduced graphene oxide induces transient blood–brain barrier opening: an in vivo study

Monique Culturato Padilha Mendonça^{1,2*}, Edilene Siqueira Soares², Marcelo Bispo de Jesus², Helder José Ceragioli³, Mônica Siqueira Ferreira⁴, Rodrigo Ramos Catharino⁴ and Maria Alice da Cruz-Höfling^{1,2*}

Abstract

Background: The blood–brain barrier (BBB) is a complex physical and functional barrier protecting the central nervous system from physical and chemical insults. Nevertheless, it also constitutes a barrier against therapeutics for treating neurological disorders. In this context, nanomaterial-based therapy provides a potential alternative for overcoming this problem. Graphene family has attracted significant interest in nanomedicine because their unique physicochemical properties make them amenable to applications in drug/gene delivery and neural interface.

Results: In this study, reduced graphene oxide (rGO) systemically-injected was found mainly located in the thalamus and hippocampus of rats. The entry of rGO involved a transitory decrease in the BBB paracellular tightness, as demonstrated at anatomical (Evans blue dye infusion), subcellular (transmission electron microscopy) and molecular (junctional protein expression) levels. Additionally, we examined the usefulness of matrix-assisted laser desorption/ionization (MALDI) mass spectrometry imaging (MSI) as a new imaging method for detecting the temporal distribution of nanomaterials throughout the brain.

Conclusions: rGO was able to be detected and monitored in the brain over time provided by a novel application for MALDI-MSI and could be a useful tool for treating a variety of brain disorders that are normally unresponsive to conventional treatment because of BBB impermeability.

Keywords: Blood–brain barrier, Paracellular pathway, Nanomaterials, MALDI-MSI

Background

The blood–brain barrier (BBB) has an intricate physical and molecular structure that provides a proper microenvironment for neuronal cell activity. The physical structure consists of a fenestration-free continuous endothelium and a surrounding basement membrane covered by a sheath of distal end-feet of astrocytes processes and pericytes. The molecular structure consists of a collection of membrane receptors and highly selective carriers that regulate the bi-directional trans-endothelial movement of molecules across the blood–brain interface. The inter-endothelial trafficking of molecules is

prevented by an elaborate, closely applied junctional contact that is provided by tight junctional and adhesion transmembrane proteins, some of which are anchored to the cell cytoskeleton. Such an intricate arrangement results in brain endothelial lining that has a very high electrical resistance compared to peripheral vascular endothelium [1]. The BBB is a highly dynamic structure that responds to minimal changes in the circulating blood and brain microenvironment through self-adjusting mechanisms that serve to protect neuronal activity. However, the complexity of the physical and molecular arrangement of the BBB precludes the accessibility of many drugs to the central nervous system. As a consequence, various neurological disorders remain untreatable and this can be an important cause of precocious death.

*Correspondence: monique.cpm@gmail.com; hofling@unicamp.br

² Department of Biochemistry and Tissue Biology, Institute of Biology, State University of Campinas, Campinas, SP, Brazil
Full list of author information is available at the end of the article



© 2015 Mendonça et al. This article is distributed under the terms of the Creative Commons Attribution 4.0 International License (<http://creativecommons.org/licenses/by/4.0/>), which permits unrestricted use, distribution, and reproduction in any medium, provided you give appropriate credit to the original author(s) and the source, provide a link to the Creative Commons license, and indicate if changes were made. The Creative Commons Public Domain Dedication waiver (<http://creativecommons.org/publicdomain/zero/1.0/>) applies to the data made available in this article, unless otherwise stated.

The emerging interdisciplinary field of nanotechnology could provide a means of overcoming the restrictive nature of the BBB with regard to drug entry into the brain. There has been considerable effort in searching for nanoscale-dimensional materials amenable to crossing the BBB and delivering drugs to specific sites of injury [2]. Among these nanomaterials, graphene and derivatives, such as reduced graphene oxide (rGO), have attracted significant interest; their free π electrons and extremely high surface area allow interaction with a variety of biomolecules, making them particularly amenable to applications in tissue engineering, molecular imaging, drug/gene delivery [3] and neural interfaces [4, 5].

An important aspect in the development of drug nanocarriers is that of ascertaining their fate in the brain and determining the amount and the way they reached the target. A number of *in vivo* techniques have been developed to detect and measure the uptake of drug nanocarriers in the brain. Usually, scanning and transmission electron microscopy (TEM), fluorescence microscopy, confocal laser microscopy and pharmacokinetic and biodistribution studies have been used for this purpose [6]. However, these techniques present substantial technical challenges and monitoring the spatial distribution of nanomaterials over time is not always easy or fast.

In recent years, matrix-assisted laser desorption/ionization (MALDI) mass spectrometry imaging (MSI) has emerged as a powerful methodology to investigate the spatial distribution of specific biomolecules in tissue sections [7]. MALDI-MSI has been used to visualize atoms and small molecules at spatial resolutions below one micron [8, 9], which is close to that of nanoparticles with at least one dimension ≤ 100 nm [10]. The present study was undertaken to test the hypothesis that MALDI-MSI could be used to detect and follow the spatial density of rGO in the brain. For comparative purposes, we also assessed the detection of rGO by confocal laser microscopy.

Another highly significant aspect to consider when studying drug transport and delivery to the brain via nanomaterials relates to the integrity of the BBB throughout treatment. To address this matter, we used three approaches to examine BBB integrity, namely: (a) gross anatomical observation based on the peripheral infusion of Evans blue dye, (b) sub-cellular evaluation by TEM in conjunction with the extracellular tracer lanthanum nitrate to determine whether the tracer escaped into the brain parenchyma, and (c) western blotting (WB) to assess possible cell-cell or cell-matrix disarray in endothelial tight and adhesion junctional proteins and laminin in brain tissue homogenates.

Results and discussion

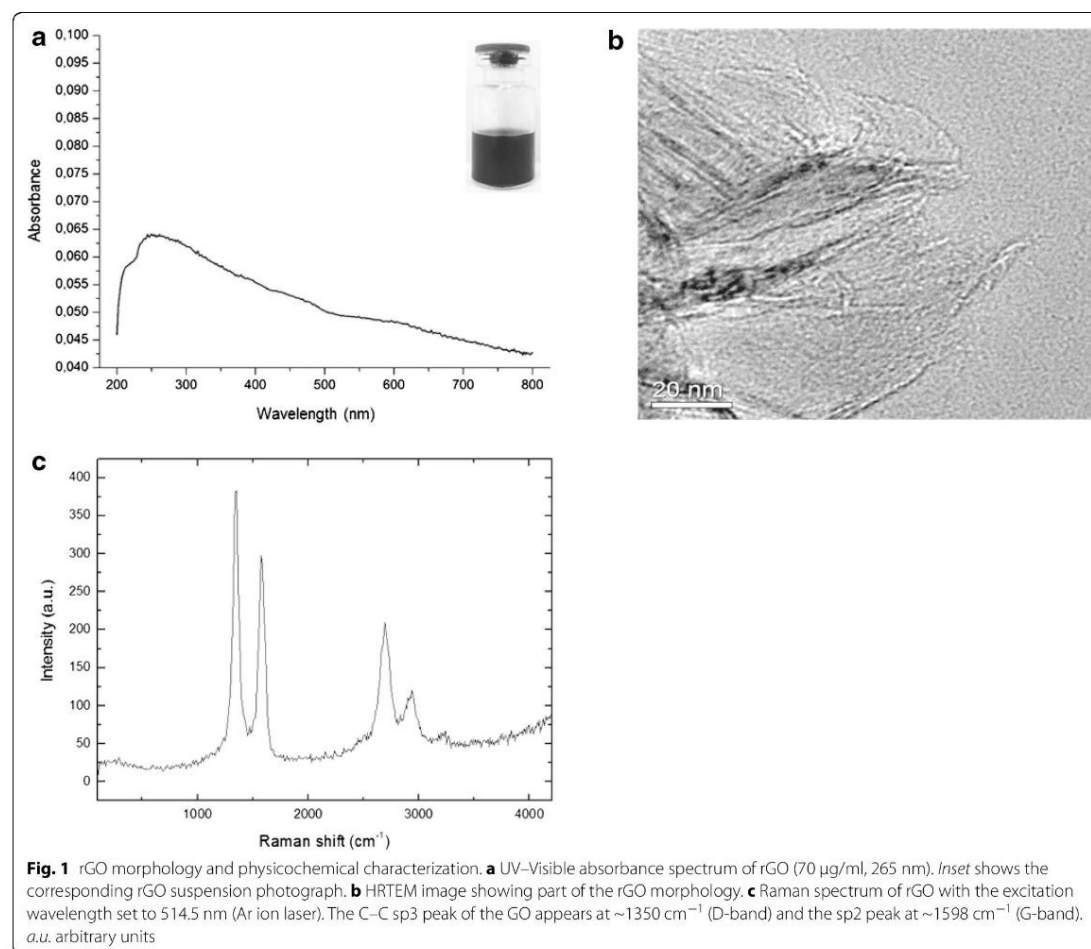
Physicochemical characterization of rGO

The uptake of nanoscale materials from the circulation and their internalization by the brain depends on their physicochemical characteristics, such as morphology, composition, uniformity, size and surface charge [11]. Graphene is composed of a single-atom-thick sheet of sp^2 -bonded carbon atoms hexagonally arranged in a two-dimensional structure that creates a large surface area on both sides of the planar axis. Graphene family-based nanomaterials include single- or few-layer-graphene, ultrathin graphite, graphene oxide, and rGO [12].

rGO was the product of treating graphene oxide under reducing conditions (chemical, thermal, microwave, photo-chemical, photo-thermal or microbial/bacterial) in order to reduce its oxygen content [13]. The reduction degree of the rGO engineered in our laboratory was investigated using UV-Visible spectroscopy. rGO in water results in a black suspension (inset Fig. 1a), which is characteristic of the reduced form of graphene oxide [14]. UV-Visible spectrum (Fig. 1a) exhibited an absorption peak at 265 nm, red-shifted when compared with graphene oxide, which exhibits a π - π^* absorption band at 230 nm [15]. The red-shift effect can be explained by a partial restoration of the π network among carbons in rGO, due to removal of the oxygen-containing bonds resulting in electronic conjugation within reduced sheets [16].

rGO was stable in sterile distilled water for over a month without forming agglomerates or changing its physicochemical characteristics. This relatively stable aqueous suspension of rGO can be attributed to the electrostatic repulsion due to the negatively charged sheets (zeta potential of -25 ± 0.18 mV) and the presence of residual oxygen functional groups at defect sites [17]. For the experiments, freshly-suspended rGO was characterized with regard to particle size, zeta potential and polydispersity index (PDI) by dynamic light scattering analysis at pH 7.6 and 25 °C; rGO showed an average diameter of 342 ± 23.5 nm and a PDI of 0.56 ± 0.03 . These results indicate that although the rGO was nanosize scale it was polydispersed, as indicated by the PDI value.

The surface morphology and structural parameters of the samples were determined by high resolution transmission electron microscopy (HRTEM) and Raman spectroscopy, respectively. Raman spectroscopy is one of the most powerful techniques for characterizing graphene-based materials [18]. The rGO sheet seen by HRTEM (Fig. 1b) had a relatively large surface area and its morphology resembled a thin curtain. The Raman spectrum of rGO displayed two main bands, D (1350 cm^{-1}) and G (1598 cm^{-1}) (Fig. 1c). These vibrational band signatures



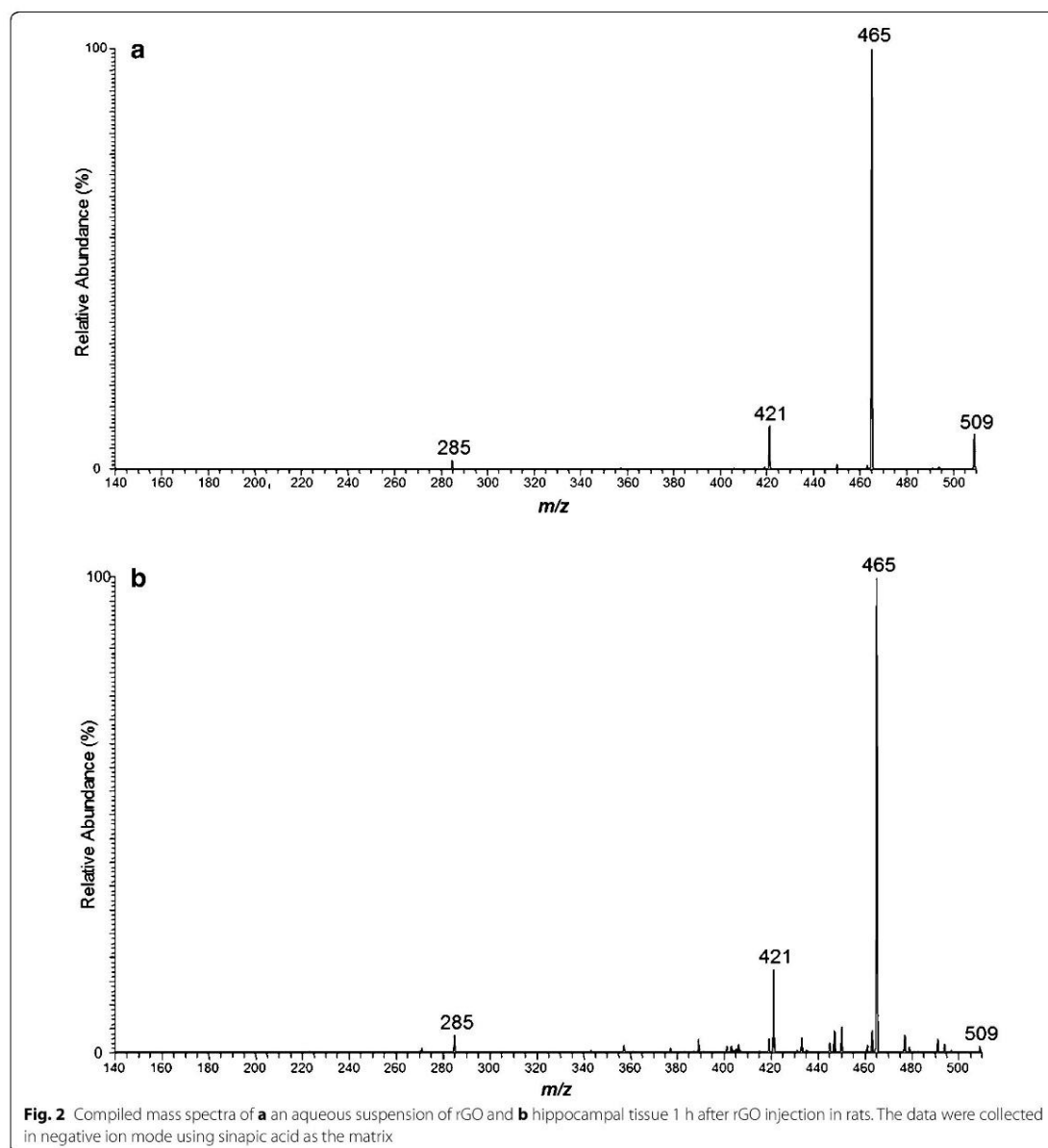
are shared by all sp²-bonded carbon atoms and correspond to the defects or edges (D-band) and to the first order Raman scattering in the E₂ g mode (G-band) [19].

rGO distribution in the brain as determined by MALDI-MSI
MALDI-MSI has previously been used to locate drugs [20, 21] and lipids [22] in rodent brains. In the present study, MALDI-MSI was used to demonstrate the presence, distribution and density of rGO within the brain over time. To map rGO by MALDI-MSI, we used a protocol established for general sample processing that included matrix-assisted laser desorption/ionization, mass analysis and image registration. A detailed step-by-step description and discussion of the MALDI-MSI technique has been published [23, 24]. Although common to all MSI platforms, the general procedure described here

requires optimization of the experimental conditions to suit the biological samples in order to obtain the best results.

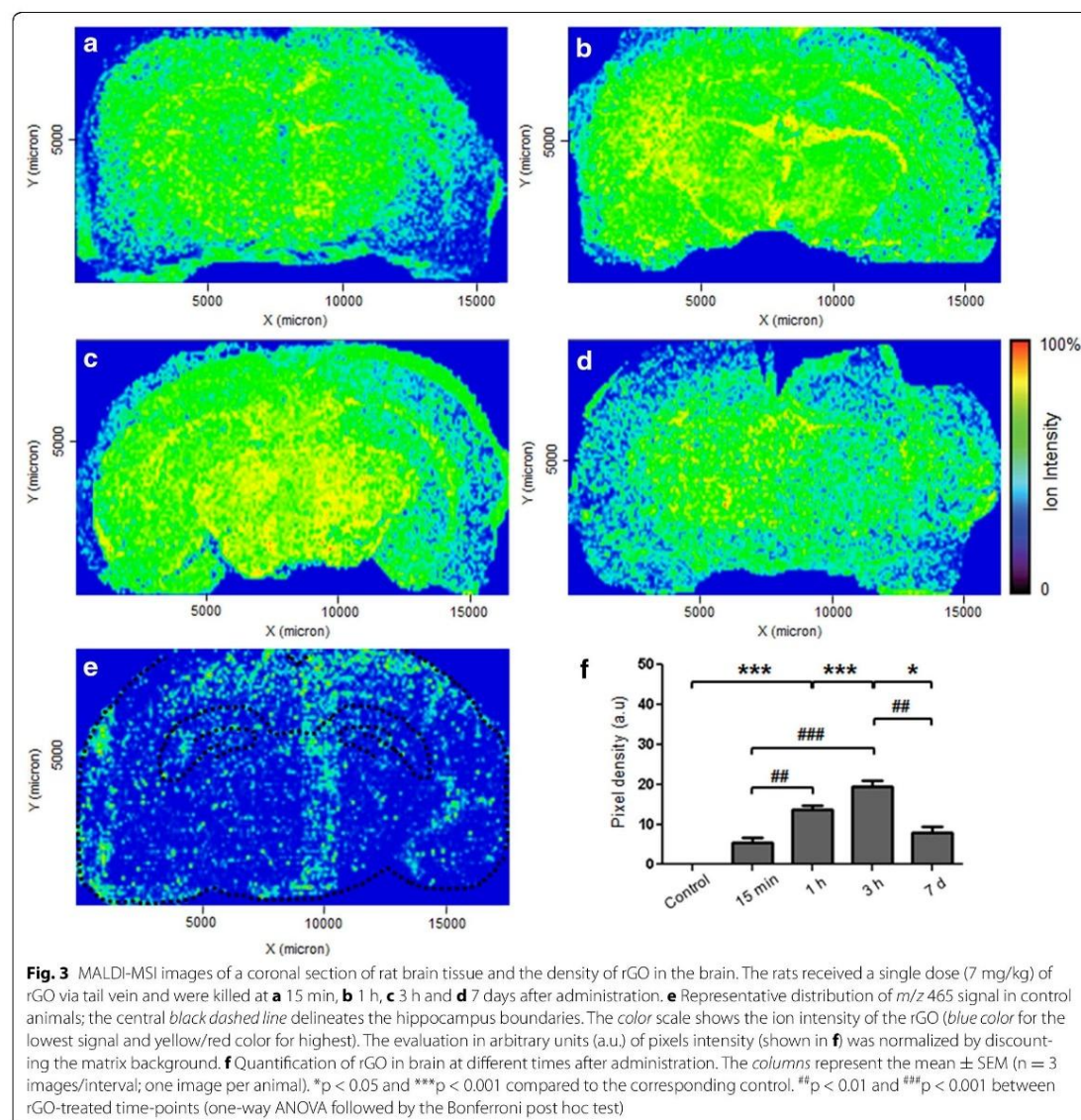
After adjusting our experimental model with regard to sample preparation and matrix application, the fragmentation pattern of the rGO was confirmed. The laser scanning of the tissue sections revealed four dominant peaks at mass-to-charge (*m/z*) ratios of 285, 421, 465 and 509 (Fig. 2). The fragmentation pattern was the same for every rGO administration.

Based on the mass-to-charge ratios of the ions detected, composite images were constructed by mapping the distribution of rGO throughout the rat brain over time (data not shown). The yellow points in Fig. 3 represent the abundance of ions with the molecular mass *m/z* 465 located in rat coronal brain sections (Fig. 3a–d).



MALDI-MSI revealed the uptake of rGO and demonstrated their spatial and temporal distribution. At 15 min post-administration, rGO was distributed throughout the brain, with the highest concentration being located mainly in two brain regions, the thalamus and hippocampus. Quantitative analysis of the mean of pixel densities (ion intensity) as a function of the rGO density

and measured in the two brain regions revealed a significant progressive increase in rGO content during the first 3 h (Fig. 3f); this increase indicated a continuous movement of rGO from peripheral blood into the brain; 7 days after rGO administration the nanomaterial content was still significantly higher than in the control, and an increase equal in magnitude to that seen 15 min after



administration. This reduction in content at 7 days indicated rGO clearance from the brain.

The large size of rGO (342 ± 23.5 nm) was apparently not an obstacle to their entrance into the brain. Very few reports have described the presence of large particles (~200–400 nm) inside the brain [25, 26] and none of them provides a clear explanation of the mechanism by which nanoparticles reach the brain. An understanding of how larger particles enter the brain is of interest

because this would allow better efficiency in drug loading, greater dispersion of drugs, and drug release over longer periods of time [27, 28].

rGO detection by confocal laser microscopy

The presence of rGO inside the brain as detected by MALDI images was corroborated by using confocal laser microscopy. After using two-photon excitation with 780-nm laser pulses, rGO emits fluorescence, mostly in the

orange-red region of the visible spectrum. The presence of rGO was detected throughout the brain parenchyma, but their density was highest in the thalamus and also with relevant density in hippocampus, with the intensity of fluorescence indicating the spatial abundance. Figure 4 illustrates the presence of fluorescent rGO in the hippocampus, with predominance of rGO clusters in the dentate gyrus.

Evaluation of BBB integrity

We next examined whether the time-related movement of rGO into the brain of treated rats, as documented by MALDI-MSI and confocal laser microscopy, involved breakdown of the BBB. Figures 3 and 4 gave evidences of the presence of rGO inside the brain parenchyma but did not show the nanoparticles crossing the BBB. As mentioned earlier, the mechanism by which nanoparticles reach the brain is of medical interest [29]. We hypothesized that for rGO to get access into the brain, the BBB had to have been disrupted once the BBB is the fence interposed between the peripheral blood stream (through which the nanoparticles were administered through the tail vein) and the brain. In addition, it would be necessary to determine which transport route was affected. To examine such questions, three-resolution level investigations were implemented.

Gross anatomical evaluation level

BBB integrity was initially assessed based on gross anatomical observation after peripheral i.v. infusion of the vital dye Evans blue. Since infused Evans blue dye cannot permeate an intact BBB [30], any entry of the dye into and spread within the brain is indicative of a leaky

BBB. The systemic infusion of Evans blue in treated control rats did not alter the typical pink color of fresh brain (Fig. 5a). In contrast, in rats administered rGO, the brain was stained a bluish gray color, indicating leakage of the dye from peripheral bloodstream into the brain parenchyma; this staining provided unmistakable evidence of BBB opening (Fig. 5b). This disruptive effect on the BBB was transient and reversible, since dye leakage was observed at 15 min, 1 and 3 h following administration of rGO, but was absent at 7 days. Staining with Evans blue has long been used in different experimental models as a reliable method for assessing BBB integrity and/or leakiness [31, 32].

Subcellular evaluation level of BBB opening based on TEM

TEM was used to assess whether hippocampal capillaries were permeable to the infusion of an electron dense extracellular tracer (lanthanum nitrate) after systemic administration of rGO. Figure 6 shows capillaries in the hippocampal parenchyma of control and rGO-treated rats that were systemically perfused with fixative containing the electron opaque extracellular tracer. In control rats, lanthanum nitrate was confined to the capillary lumen and the surrounding neuropile showed mitochondria, unmyelinated axons and synaptic contacts apparently normal-looking (Fig. 6a). In contrast, in capillaries of treated rats the extracellular tracer infiltrated the endothelial cleft, indicating a decrease in the paracellular tightness of the barrier after exposure to rGO (Fig. 6b; insets show details of the interendothelial cleft filled with tracer). This feature was more frequent at 3 h and was not observed at 7 days after rGO administration. The perivascular end-feet processes of astrocytes

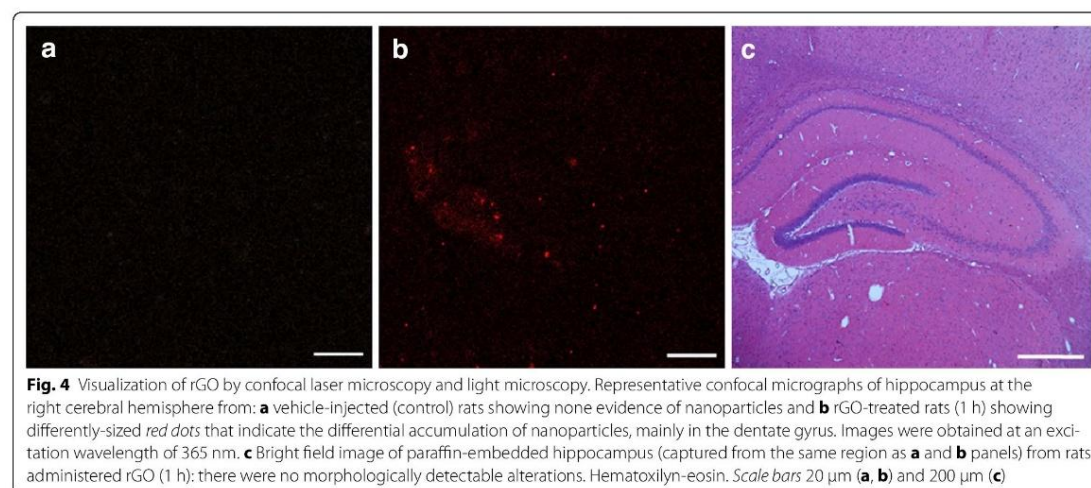


Fig. 4 Visualization of rGO by confocal laser microscopy and light microscopy. Representative confocal micrographs of hippocampus at the right cerebral hemisphere from: **a** vehicle-injected (control) rats showing none evidence of nanoparticles and **b** rGO-treated rats (1 h) showing differently-sized *red dots* that indicate the differential accumulation of nanoparticles, mainly in the dentate gyrus. Images were obtained at an excitation wavelength of 365 nm. **c** Bright field image of paraffin-embedded hippocampus (captured from the same region as **a** and **b** panels) from rats administered rGO (1 h); there were no morphologically detectable alterations. Hematoxylin-eosin. Scale bars 20 μm (**a**, **b**) and 200 μm (**c**)

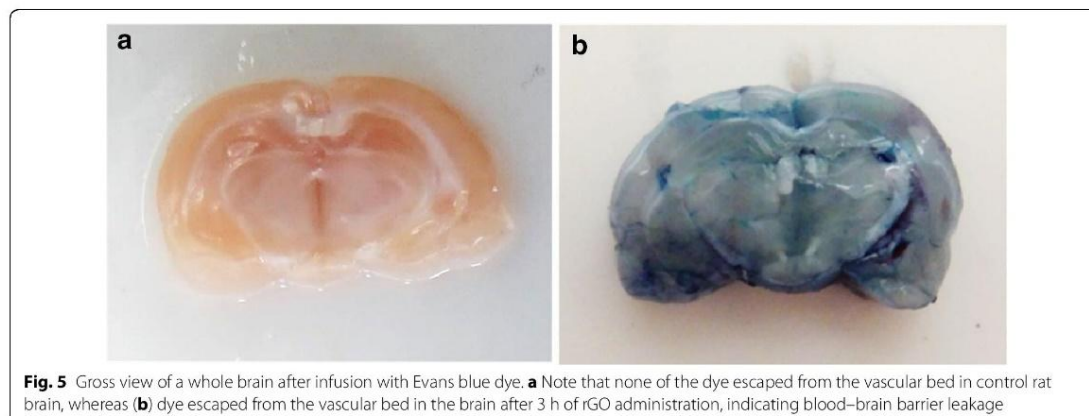


Fig. 5 Gross view of a whole brain after infusion with Evans blue dye. **a** Note that none of the dye escaped from the vascular bed in control rat brain, whereas **(b)** dye escaped from the vascular bed in the brain after 3 h of rGO administration, indicating blood–brain barrier leakage

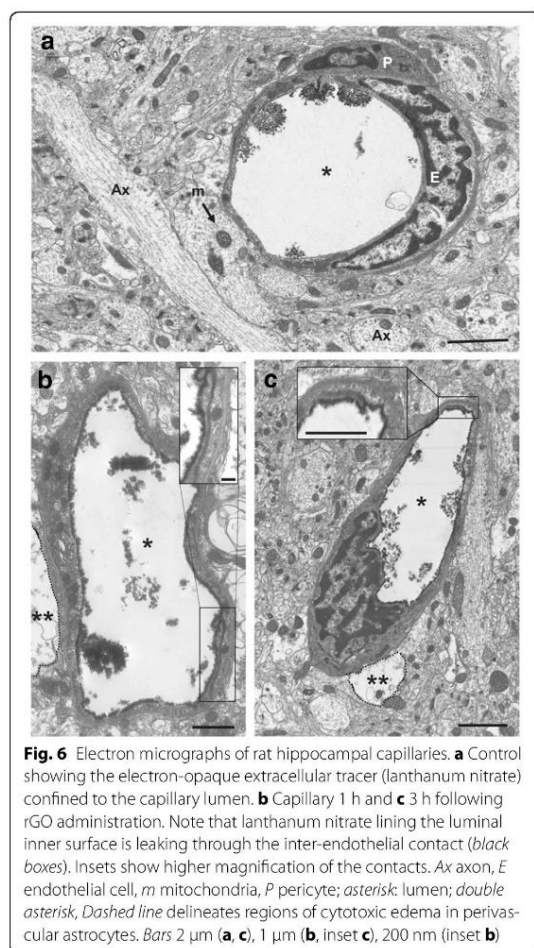


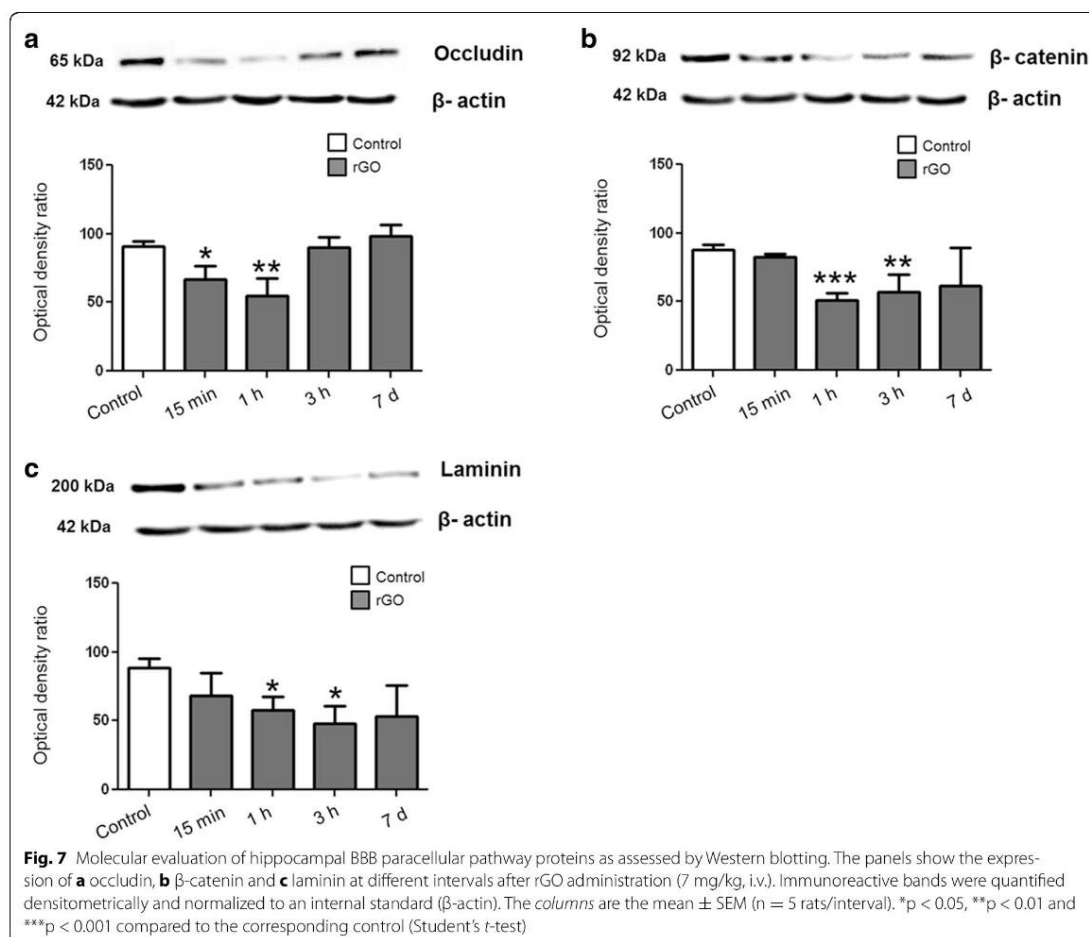
Fig. 6 Electron micrographs of rat hippocampal capillaries. **a** Control showing the electron-opaque extracellular tracer (lanthanum nitrate) confined to the capillary lumen. **b** Capillary 1 h and **c** 3 h following rGO administration. Note that lanthanum nitrate lining the luminal inner surface is leaking through the inter-endothelial contact (black boxes). Insets show higher magnification of the contacts. Ax axon, E endothelial cell, m mitochondria, P pericyte; asterisk: lumen; double asterisk, Dashed line delineates regions of cytotoxic edema in perivascular astrocytes. Bars 2 μm (**a**, **c**), 1 μm (**b**, inset **c**), 200 nm (inset **b**)

encircling leaked capillaries appeared swollen and were suggestive of cytotoxic edema. This was yet another indication that the BBB permeability was altered by the i.v. peripheral injection of rGO [33]. However, despite these changes, no extracellular tracer was observed filling the basement membrane or spreading through the neuropil interstitium. This finding suggested that rGO-induced alterations in the BBB did not cause vasogenic edema but simply induced abnormal astrocyte osmoregulation [34].

Detailed ultrastructural observations showed that leakage of the paracellular barrier was regionally highly heterogeneous since in some capillaries of rGO-treated rats the lanthanum nitrate was confined to the lumen, as in the controls. This finding suggested that the tightness of the BBB varied throughout the hippocampal parenchyma; regional heterogeneity in the permeability of the brain vasculature and tightness of the BBB, even in the same vascular segment, is not uncommon and has been well-documented [35].

Molecular evaluation level by WB of hippocampal BBB paracellular pathway proteins

The western blotting analysis showing that the proteins associated with the impermeability of the BBB were down-regulated corroborated the TEM findings showing the extravasation of extracellular tracer at 1 h and 3 h post-rGO injection (Fig. 7). The expression of tight junction protein occludin, adherens junction protein β -catenin, and laminin from basal lamina was down-regulated at the same periods after rGO injection as shown by TEM. Occludin was the first protein to be affected, with significant downregulation (36 %) 15 min after rGO administration that reached 66 % after 1 h. β -catenin and laminin were decreased by 72 and 51 % at 1 h and 54 and 84 %, at 3 h, respectively.

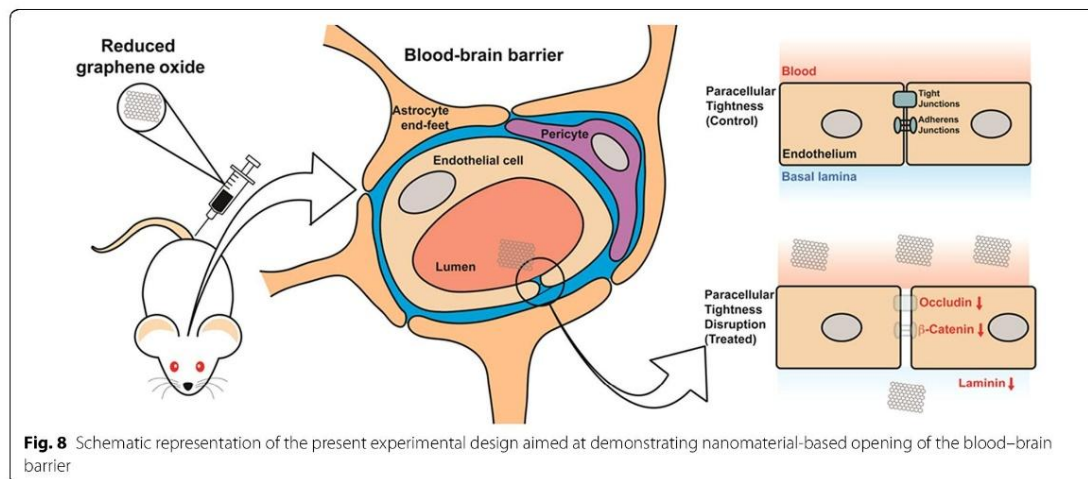


The immediate decrease in the levels of occludin and the ensuing decrease of laminin and β -catenin indicated that the systemic administration of rGO was able to disturb the paracellular permeability of the BBB. By day 7, the expression of all proteins had returned to control levels (Fig. 7a–c). These findings agreed with the progressive entry of rGO (15 min to 3 h) into the brain and their tendency to decrease to baseline (7 days) seen with MALDI-MSI. The short-lived disruption seen here indicated the reversible nature of the interference in BBB permeability caused by the rGO and confirmed a protective role for the BBB in normal brain function. In addition, the persistence of rGO within the brain for at least 1 week (as measured by MALDI-MSI) represents a good prospect for therapeutic strategies aimed at the long-term delivery

of drugs [36] while at the same time reducing possible side-effects. Based on the findings of this study, we suggest that the use of rGO could be advantageous relative to other non-invasive approaches that disrupt the BBB, such as the use of ultrasound [37], hyperosmolar osmotic solutions (mannitol) [38] and pharmacological agents (histamine and bradykinin) [39] because of their ability to simultaneously modulate BBB permeability and act as drug delivery promoters.

Conclusions

We have characterized rGO produced in our laboratory and have described a novel application for MALDI-MSI in detecting the possible presence and temporal distribution of these particles in the brain after intravenous administration in rats. Although



the crossing of rGO at the BBB was not shown, multiple resolution scale assessment revealed that in rGO-treated rats the BBB was time-dependently permeabilized through the weakening of the paracellular pathway. The transitory BBB breakdown after rGO injection was demonstrated by the passage of Evans blue dye from peripheral circulation to the brain, by lanthanum nitrate infiltration into the inter-endothelial cleft and by down-regulation of tight junction, adhesion junction and basement membrane proteins. Together, these findings indicate that administration of rGO decreases the paracellular tightness of the BBB (Fig. 8).

Although we still have to assess the toxicological effects of rGO, the results presented here suggest that rGO could be useful in providing nanomaterial-based therapy. Mainly, this could be potentially useful tool for treating a variety of brain disorders that are normally unresponsive to conventional treatment because of BBB impermeability.

Methods

rGO preparation and characterization

rGO was produced from catalytic conversion using hot-filament chemical vapor deposition process. Briefly, titanium substrate was immersed in 1 ml of polyaniline diluted in 2 ml of N-dimethylformamide, after which it was allowed drying for 2 h at room temperature. Then, 0.2 ml of nickel nitrate dissolved in 1 ml of pure acetone was added to the preparation. In the chemical vapor deposition chamber, tungsten filaments were heated (1500 °C) to decompose the reactive gases and heat the substrate. The hydrocarbons used as a carbon source were acetone, camphor and citric acid (1:1:1), which

were dragged by hydrogen flow. The catalytic conversion is conducted under 10 Torr pressure and 65 sccm of nitrogen and 20 sccm of oxygen. The growth temperature (450 °C) was kept for 1 min in only hydrogen atmosphere in order to reduce the graphene oxide. After reduction, rGO was suspended in sterile distilled water (1 mg/ml) and sonicated for 5 min immediately prior to its use in experiments.

Morphological analysis of the sample was done with HRTEM. A drop of rGO aqueous suspension was deposited on carbon-coated copper grid. The excess water was removed by a filter paper; then, the samples were left to dry under ambient air and analyzed using a JEOL JSM-6330F microscope operated at 300 kV. The molecular structure was characterized by inVia Raman microscope (Renishaw, Wotton-under-Edge, UK) using the 514 nm wavelength of an argon-ion laser. All samples were deposited onto glass slides in powdered form without using vehicle. Absorption spectrum (800–200 nm) of rGO (70 µg/ml) was recorded at room temperature using a Varian Cary 5. rGO size distribution was measured by light scattering using a ZetaPALS Zeta Potential Analyzer (Brookhaven Instruments, NY, USA) at standard settings, typically 10 sub-runs of 30 s. Particle size and PDI were estimated using built-in software. The zeta potential was subsequently measured in the same sample using a conditioned electrode and was typically based on 10 runs in which the relative residual from model fitting was used. Each sample was measured three times consecutively.

Animal care and rGO systemic administration

Male Wistar rats (*Rattus norvegicus*, 6 week-old, 180 ± 40 g) obtained from the Multidisciplinary Center

for Biological Investigation at the State University of Campinas were housed 5/cage at 23 °C on a 12 h light/dark cycle, with lights on at 6 a.m. and access to water and food ad libitum. The animal experiments were approved by the institutional Committee for Ethics in Animal Use (protocol no. 2884-1) and were done in accordance with the ethical guidelines of the Brazilian Society of Laboratory Animal Science.

For toxicological assessment of nanomaterials involving intravenous (i.v.) administration, the stock solution concentrations of water-dispersible carbon nanostructures are generally ≤ 10 mg/ml and the maximum permissible dose is < 10 mg/kg [40, 41]. Based on these guidelines, rats were injected via tail vein with a rGO suspension (7 mg/kg; 1.0–1.5 ml) or vehicle (sterile distilled water, control group) and, after 15 min, 1 and 3 h and 7 days, the rats ($n = 3$ per time interval for MALDI-MSI/confocal laser microscopy; $n = 3$ per time interval for Evans blue; $n = 3$ per time interval for TEM and $n = 5$ per time interval for WB) were killed with an overdose of a mixture (3:1) of ketamine chloride (Dopalen[®], 100 mg/kg body weight) and xylazine chloride (Anasedan[®], 10 mg/kg body weight) (Vetbrands, Jacarei, SP, Brazil) or CO₂. A single control group killed 1 h after vehicle injection was used for comparison ($n = 14$) since preliminary experiments showed no time-related differences in the responses of control rats.

Detection of rGO in the brain

MALDI-MSI analysis

At the time intervals indicated above, rats were anesthetized with an intraperitoneal injection of a mixture of ketamine chloride and xylazine chloride and perfused via the left ventricle with physiological saline followed by 4 % paraformaldehyde (PFA) in 0.1 M phosphate buffered saline (PBS), pH 7.4. The brains were quickly removed, post-fixed for 2 h in the same fixative and afterward successively cryo-protected in 15 and 30 % sucrose solutions (24 h each) at 4 °C. Since brain tissue is very friable, the samples were embedded in OCT-Tissue Tek (Sakura Finetek, Torrance, CA, USA) and frozen in n-hexane (Dinâmica, São Paulo, SP, Brazil), cooled with liquid nitrogen and stored at -80 °C until cryo-sectioning (Leica CM 1850 Cryostat; Milton Keynes, UK). Cryosections 10 μ m thick were collected on glass microscope slides that were then covered with a matrix solution (synaptic acid, 10 mg/ml in 60:40 acetonitrile:H₂O) using a commercial airbrush. Images and mass spectra were acquired in a MALDI-LTQ-XL MSI instrument (Thermo Scientific, Carlsbad, CA, USA) equipped with a laser (Nd:YAG, 355 nm) at *minimum* focus setting and a quadrupole-ion-trap analyzing system in negative ion mode. For image acquisition, a 100 μ m raster width was

selected. The data were standardized using collision-induced energy to 35 eV. Helium was used as the collision gas. All imaging data were processed using ImageQuest software v.1.0.1 (Thermo Scientific).

Mass and intensity values for each spectrum were included in the Principal Component Analysis (PCA), which was performed using Unscrambler v.9.7 (CAMO Software, Trondheim, Norway). After discrimination by PCA, MS/MS reactions were performed to generate their fragmentation pattern.

The quantification and distribution of rGO in the brain were assessed using GNU Image Manipulation Program (GIMP) 2.8 software that converted the digitized MALDI images to grayscale images ($n = 3$ images/time, i.e., one image per rat; $n = 3$ rats/time) after yellow color-based selection [42]; in each image, the range of yellows shading the dots, and representing the rGO depth into tissue, were selected dynamically by the program which thus converted them to digitized grayscale dots and further to pixels' intensity. The mean of the sum of pixels in each time point was plotted as histogram. The red dots were not computed in terms of pixels given its paucity and minimal distribution. Figure 9 illustrates the appearance of spatial distribution of yellow dots representing rGO nanoparticles following computer-based image conversion to digitized grayscale.

Confocal laser microscopy analysis

The same samples prepared for MALDI-MSI analysis were examined using a Zeiss LSM 780-NLO confocal imager fitted on an Axio Observer Z.1 microscope (Carl Zeiss AG, Germany) equipped with a 60 \times oil immersion lens. The images were acquired using the pinholes set to 1 airy unit for each channel in a sequential manner and analyzed using ImageJ 1.45 s software (NIH, Bethesda, USA). The images of rGO were obtained using two-photon excitation with 780-nm laser pulses and emission spectra were recorded between 611 and 735 nm [43, 44].

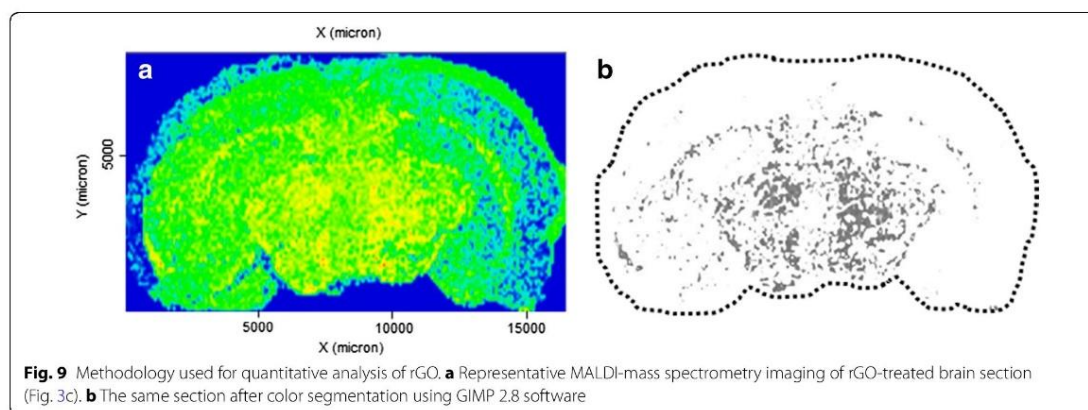
Evaluation of BBB integrity

Gross analysis by Evans blue peripheral infusion

BBB integrity was first examined by assessing Evans blue dye extravasation [45]. Briefly, 10 min prior the end of each time course, Evans blue dye solution was injected (10 mg/kg of 2 % dye in 0.9 % NaCl) intravenously through the tail vein. Animals were killed with an overdose of anesthetic and the brains were rapidly removed and photographed.

Ultrastructural analysis of extracellular tracer leakage

One hour after vehicle administration and at various intervals after rGO injection, rats were anesthetized with ketamine/xylazine and killed by transcardial perfusion



with 80 ml of 0.9 % NaCl followed by 250 ml of fixative solution (2.5 % PFA, 2.5 % glutaraldehyde plus 2 % lanthanum nitrate in 0.1 M sodium cacodylate, pH 7.2) as described in previous study [46, 47]. The rats were maintained at 4 °C for 12–18 h to allow adequate fixation before brain dissection and processing in order to minimize tissue artifacts. The brain was then excised and the hippocampi were dissected. Hippocampi were selected for analysis because this was a brain region in which an appreciable concentration of rGO was found by MALDI-MSI. Tissue samples 0.5–1 mm thick were immersed in the same fixative (lanthanum nitrate-free) for 2 h. After rinsing, the samples were post-fixed in 1 % osmium tetroxide plus 1 % potassium ferricyanide in glucose solution (0.2 M sucrose plus 0.1 M NaCl) for 1 h, washed three times and dehydrated in a graded ethanol series (50–100 %), ethanol:acetone (1:1) and 100 % acetone, followed by infiltration with acetone:Epon (1:1) and embedding in Epon 812 (Sigma Aldrich, St. Louis, MO, USA) resin for 24 h at room temperature. The samples were subsequently transferred to fresh resin for polymerization (72 h at 60 °C). The areas of interest were chosen by histological analysis of semi-thin sections (0.5 μm thick) stained with 0.5 % toluidine blue. Ultrathin (70 nm thick) sections from selected areas were placed on 200-mesh copper grids, double contrasted with 2 % uranyl acetate (in 70 % methanol) followed by 0.5 % lead citrate aqueous solution before examination in a Zeiss LEO 906 transmission electron microscope (Carl Zeiss MicroImaging GmbH, Göttingen, Germany) operated at 60 kV.

Western blotting of proteins associated with the BBB in hippocampal homogenates

At 15 min, 1 h, 3 h and 7 days after rGO i.v. injection or 1 h after vehicle injection, the rats were anesthetized by

CO₂ inhalation and killed by decapitation. Protein was extracted from hippocampus as previously described [48]. After electrotransfer, the membranes were incubated with 5 % skimmed milk to block non-specific sites prior followed by washing with TBS-T (0.1 % Tris-buffered saline with 0.05 % Tween 20, pH 7.4). Subsequently, the membranes were incubated with primary antibodies against β-catenin (1:500; sc-7963, Santa Cruz Biotechnology, Santa Cruz, CA, USA), occludin (1:500; sc-5562, Santa Cruz) and laminin (1:500; L9393, Sigma Aldrich) followed by washing with TBS-T and incubation with HRP-labeled anti-mouse (for anti-β-catenin and anti-β-actin) or anti-rabbit (anti-occludin and anti-laminin) secondary antibody (1:1000, Sigma Aldrich). Immunoreactive bands were visualized using a chemiluminescence kit (Super Signal West Pico Chemiluminescent Substrate; Pierce Biotechnology, Rockford, IL, USA). The blots were subsequently stripped and probed with anti-β-actin (1:1000; A2228, Sigma Aldrich); β-actin was used as an internal control to monitor protein loading, the efficiency of blot transfer, and nonspecific changes in protein levels. The luminescent signal of each band was captured with a G:BoxiChemi camera (Syngene, Cambridge, UK) and band intensity was quantified using ImageJ 1.45 s software (NIH, Bethesda, MD, USA).

Statistical analysis

Quantitative data were expressed as the mean ± standard error of the mean (SEM). Statistical significance was determined by one-way ANOVA followed by the Bonferroni post hoc test for multiple variant analysis and Student's *t* test for pairwise analyses. A value of $p < 0.05$ indicated significance. All analyses were done using Prism software, version 5 (GraphPad Inc., La Jolla, CA, USA).

Abbreviations

AJ: adherens junction; ANOVA: analysis of variance; BBB: blood–brain barrier; HRTEM: high-resolution transmission electron microscopy; MALDI-MSI: matrix-assisted laser desorption/ionization mass spectrometry imaging; PBS: phosphate buffered saline; PCA: Principal Component Analysis; PDI: polydispersity index; PFA: paraformaldehyde; rGO: reduced graphene oxide; SEM: standard error of the mean; TEM: transmission electron microscopy; TJ: tight junction; WB: western blotting.

Authors' contributions

HJC carried out the nanoparticles synthesis; MBJ participated in the characterization of rGO and carried out confocal microscopy analysis. MSF and RRC carried out the MALDI-MSI experiments. MCPM, ESS and MACH designed and performed experiments, analyzed data and wrote the paper. All authors discussed the results and commented on the manuscript. All authors read and approved the final manuscript.

Author details

¹ Department of Pharmacology, Faculty of Medical Sciences, State University of Campinas, Campinas, SP, Brazil. ² Department of Biochemistry and Tissue Biology, Institute of Biology, State University of Campinas, Campinas, SP, Brazil. ³ Department of Semiconductors, Instruments and Photonics, Faculty of Electrical and Computer Engineering, State University of Campinas, Campinas, SP, Brazil. ⁴ Department of Medicine and Experimental Surgery, Faculty of Medical Sciences, State University of Campinas, Campinas, SP, Brazil.

Acknowledgements

This work was supported by the Brazilian funding agencies Fundação de Amparo à Pesquisa do Estado de São Paulo (FAPESP) (grant nos. 11/50400-0 and 2012/24782-5) and Conselho Nacional de Desenvolvimento Científico e Tecnológico (CNPq) (grant nos. 305099/2011-6 and 486142/2012-4). We thank the National Institute of Science and Technology on Photonics Applied to Cell Biology (INFABIC) at UNICAMP for providing access to equipment. INFABIC is co-funded by FAPESP (grant no. 08/57906-3) and CNPq (grant no. 573913/2008-0). We are indebted to Prof. Stephen Hyslop for English editing. This work is dedicated to Professor Vitor Baranauskas *"In memoriam"*.

Competing interests

The authors declare that they have no competing interests.

Received: 7 September 2015 Accepted: 27 October 2015

Published online: 30 October 2015

References

- Abbott NJ, Patabendige AA, Dolman DE, Yusof SR, Begley DJ. Structure and function of the blood–brain barrier. *Neurobiol Dis.* 2010;37:13–25.
- Masserini M. Nanoparticles for brain drug delivery. *ISRN Biochem.* 2013;2013:238428. doi:10.1155/2013/238428.
- Goenka S, Sant V, Sant S. Graphene-based nanomaterials for drug delivery and tissue engineering. *J Control Release.* 2014;173:75–88.
- Li N, Zhang X, Song Q, Su R, Qi Z, Kong T, et al. The promotion of neurite sprouting and outgrowth of mouse hippocampal cells in culture by graphene substrates. *Biomaterials.* 2011;32:9374–82.
- Kim SM, Joo P, Ahn G, Cho IH, Kim DH, Song WK, et al. Transparent conducting films based on reduced graphene oxide multilayers for biocompatible neuronal interfaces. *J Biomed Nanotechnol.* 2013;9:403–8.
- Van Rooy I, Cakir-Tascioglu S, Hennink WE, Storm G, Schiffelers RM, Mastrobattista E. In vivo methods to study uptake of nanoparticles into the brain. *Pharm Res.* 2011;28:456–71.
- McDonnell LA, Heeren RMA. Imaging mass spectrometry. *Mass Spectrom Rev.* 2007;26:606–43.
- Zimmerman TA, Monroe EB, Tucker KR, Rubakhin SS, Sweedler JV. Imaging of cells and tissues with mass spectrometry: adding chemical information to imaging. *Methods Cell Biol.* 2008;89:361–90.
- Fujimura Y, Miura D. MALDI mass spectrometry imaging for visualizing in situ metabolism of endogenous metabolites and dietary phytochemicals. *Metabolites.* 2014;4:319–46.
- Buzea C, Pacheco II, Robbie K. Nanomaterials and nanoparticles: sources and toxicity. *Biointerphases.* 2007;2:17–71.
- de Jesus MB, Kapila YL. Cellular mechanisms in nanomaterial internalization, intracellular trafficking, and toxicity. In: Durán N, Guterres SS, Alves OL, editors. *Nanomedicine and Nanotoxicology*. New York: Springer; 2014. p. 201–27.
- Sanchez VC, Jachak A, Hurt RH, Kane AB. Biological interactions of graphene-family nanomaterials: an interdisciplinary review. *Chem Res Toxicol.* 2012;25:15–34.
- Bianco A, Cheng HM, Enoki T, Gogotsi Y, Hurt RH. All in the graphene family—A recommended nomenclature for two-dimensional carbon materials. *Carbon.* 2013;65:1–6.
- Tian J, Li H, Xing Z, Wang L, Luo Y, Asiri AM, et al. One-pot green hydrothermal synthesis of CuO–Cu₂O–Cu nanorod-decorated reduced graphene oxide composites and their application in photocurrent generation. *Catal Sci Technol.* 2012;2:2227–30.
- Yang S, Yue W, Huang D, Chen C, Lin H, Yang X. A facile green strategy for rapid reduction of graphene oxide by metallic zinc. *RSC Adv.* 2012;2:8827–32.
- Li D, Müller MB, Gilje S, Kaner RB, Wallace GG. Processable aqueous dispersions of graphene nanosheets. *Nat Nanotechnol.* 2008;3:101–5.
- Konios D, Stylianakis MM, Stratakis E. Kymakis Dispersion behaviour of graphene oxide and reduced graphene oxide. *J Colloid Interface Sci.* 2014;430:108–12.
- Ferrari AC, Basko DM. Raman spectroscopy as a versatile tool for studying the properties of graphene. *Nat Nanotechnol.* 2013;8:235–46.
- Ferrari AC, Meyer JC, Scardaci V, Casiraghi C, Lazzeri M, Mauri F, et al. Raman spectrum of graphene and graphene layers. *Phys Rev Lett.* 2006;97:187401.
- Hsieh Y, Casale R, Fukuda E, Chen J, Knemeyer I, Wingate J, et al. Matrix-assisted laser desorption/ionization imaging mass spectrometry for direct measurement of clozapine in rat brain tissue. *Rapid Commun Mass Spectrom.* 2006;20:965–72.
- Liu X, Ide JL, Norton I, Marchionni MA, Ebling MC, Wang LY, et al. Molecular imaging of drug transit through the blood–brain barrier with MALDI mass spectrometry imaging. *Sci Rep.* 2013;3:2859.
- Berry KA, Hankin JA, Barkley RM, Spraggins JM, Caprioli RM, Murphy RC. MALDI imaging of lipid biochemistry in tissues by mass spectrometry. *Chem Rev.* 2011;111:6491–512.
- Chughtai K, Heeren RMA. Mass spectrometric imaging for biomedical tissue analysis. *Chem Rev.* 2010;110:3237–77.
- Norris JL, Caprioli RM. Analysis of tissue specimens by matrix-assisted laser desorption/ionization imaging mass spectrometry in biological and clinical research. *Chem Rev.* 2013;113:2309–42.
- Schroeder U, Sommerfeld P, Sabel BA. Efficacy of oral dalargin-loaded nanoparticle delivery across the blood–brain barrier. *Peptides.* 1998;19:777–80.
- Selvi BR, Jagadeesan D, Suma BS, Nagashankar G, Arif M, Balasubramanyam K, et al. Intrinsically fluorescent carbon nanospheres as a nuclear targeting vector: delivery of membrane-impermeable molecule to modulate gene expression in vivo. *Nano Lett.* 2008;8:3182–8.
- Nance EA, Woodworth GF, Sailor KA, Shih TY, Xu Q, Swaminathan G, et al. A dense poly(ethylene glycol) coating improves penetration of large polymeric nanoparticles within brain tissue. *Sci Transl Med.* 2012;4:149.
- Misra A, Ganesh S, Shahiwala A, Shah SP. Drug delivery to the central nervous system: a review. *J Pharm Pharm Sci.* 2003;6:252–73.
- Jaffer H, Adjei IM, Labhasetwar V. Optical imaging to map blood–brain barrier leakage. *Sci Rep.* 2013;1:3117.
- Kaya M, Ahishali B. Assessment of permeability in barrier type of endothelium in brain using tracers: Evans blue, sodium fluorescein, and horseradish peroxidase. *Methods Mol Biol.* 2011;763:369–82.
- Radu M, Chernoff J. An in vivo assay to test blood vessel permeability. *J Vis Exp.* 2013;73:50062.
- Berezowski V, Fukuda AM, Cecchelli R, Badaut J. Endothelial cells and astrocytes: a concerto en duo in ischemic pathophysiology. *Int J Cell Biol.* 2012;2012:176287. doi:10.1155/2012/176287.
- Saubaméa B, Cochois-Guégan V, Cisternino S, Scherrmann JM. Heterogeneity in the rat brain vasculature revealed by quantitative confocal analysis of endothelial barrier antigen and P-glycoprotein expression. *J Cereb Blood Flow Metab.* 2012;32:81–92.

34. Klatzo I. Pathophysiological aspects of brain edema. *Acta Neuropathol (Berl)*. 1987;72:236–9.
35. Raleigh DR, Marchiando AM, Zhang Y, Shen L, Sasaki H, Wang YM, et al. Tight junction-associated MARVEL proteins marvelD3, tricellulin, and occludin have distinct but overlapping functions. *Mol Biol Cell*. 2010;21:1200–13.
36. Stamatovic SM, Keep RF, Andjelkovic AV. Brain endothelial cell-cell junctions: how to “open” the blood brain barrier. *Curr Neuropharmacol*. 2008;6:179–92.
37. Konofagou EE, Tung YS, Choi J, Deffieux T, Baseri B, Vlachos F. Ultrasound-induced blood-brain barrier opening. *Curr Pharm Biotechnol*. 2012;13:1332–45.
38. Kroll RA, Neuwelt EA. Outwitting the blood-brain barrier for therapeutic purposes: osmotic opening and other means. *Neurosurgery*. 1998;42:1083–100.
39. Martin JA, Maris AS, Ehtesham M, Singer RJ. Rat model of blood-brain barrier disruption to allow targeted neurovascular therapeutics. *J Vis Exp*. 2012;30:e50019.
40. Kanakia S, Toussaint JD, Mullick Chowdhury S, Tembulkar T, Lee S, Jiang YP, et al. Dose ranging, expanded acute toxicity and safety pharmacology studies for intravenously administered functionalized graphene nanoparticle formulations. *Biomaterials*. 2014;35:7022–31.
41. Yang K, Li Y, Tan X, Peng R, Liu Z. Behavior and toxicity of graphene and its functionalized derivatives in biological systems. *Small*. 2013;9:1492–503.
42. Solomon RW. Free and open source software for manipulation of digital images. *Am J Roentgenol*. 2009;192:330–4.
43. Chien CT, Li SS, Lai WJ, Yeh YC, Chen HA, Chen IS, et al. Tunable photoluminescence from graphene oxide. *Angew Chem Int Ed Engl*. 2012;51:6662–6.
44. Vempati S, Uyar T. Fluorescence from graphene oxide and the influence of ionic, p–p interactions and heterointerfaces: electron or energy transfer dynamics. *Phys Chem Chem Phys*. 2014;16:21183–203.
45. Nag S. Blood-brain barrier permeability using tracers and immunohistochemistry. *Methods Mol Med*. 2003;89:133–44.
46. De Paula Le Sueur L, Kalapothakis E, da Cruz-Höfling MA. Breakdown of the blood-brain barrier and neuropathological changes induced by *Phoneutria nigriventer* spider venom. *Acta Neuropathol*. 2003;105(2):125–34.
47. Le Sueur LP, Collares-Buzato CB, da Cruz-Höfling MA. Mechanisms involved in the blood-brain barrier increased permeability induced by *Phoneutria nigriventer* spider venom in rats. *Brain Res*. 2004;1027(1–2):38–47.
48. Mendonça MC, Soares ES, Stávale LM, Raposo C, Coope A, Kalapothakis E, et al. Expression of VEGF and Flk-1 and Flt-1 receptors during blood-brain barrier (BBB) impairment following *Phoneutria nigriventer* spider venom exposure. *Toxins (Basel)*. 2013;5:2572–88.

Submit your next manuscript to BioMed Central and take full advantage of:

- Convenient online submission
- Thorough peer review
- No space constraints or color figure charges
- Immediate publication on acceptance
- Inclusion in PubMed, CAS, Scopus and Google Scholar
- Research which is freely available for redistribution

Submit your manuscript at
www.biomedcentral.com/submit



Capítulo II

Mendonça et al. *J Nanobiotechnol* (2016) 14:53
DOI 10.1186/s12951-016-0206-9

Journal of Nanobiotechnology

RESEARCH

Open Access



Reduced graphene oxide: nanotoxicological profile in rats

Monique Culturato Padilha Mendonça^{1,2*}, Edilene Siqueira Soares², Marcelo Bispo de Jesus², Helder José Ceragioli³, Silvia Pierre Irazusta⁴, Ângela Giovana Batista⁵, Marco Aurélio Ramirez Vinolo⁶, Mário Roberto Maróstica Júnior⁵ and Maria Alice da Cruz-Höfling^{1,2*}

Abstract

Background: We have previously demonstrated that reduced graphene oxide (rGO) administered intravenously in rats was detected inside the hippocampus after downregulation of the tight and adherens junction proteins of the blood–brain barrier. While down-regulators of junctional proteins could be useful tools for drug delivery through the paracellular pathway, concerns over toxicity must be investigated before clinical application. Herein, our purpose was to trace whether the rGO inside the hippocampus triggered toxic alterations in this brain region and in target organs (blood, liver and kidney) of rats at various time points (15 min, 1, 3 h and 7 days).

Results: The assessed rGO-treated rats (7 mg/kg) were clinically indistinguishable from controls at all the time points. Hematological, histopathological (neurons and astrocytes markers), biochemical (nephrotoxicity and hepatotoxicity assessment) and genotoxicological based tests showed that systemic rGO single injection seemed to produce minimal toxicological effects at the time points assessed. Relative to control, the only change was a decrease in the blood urea nitrogen level 3 h post-treatment and increases in superoxide dismutase activity 1 h and 7 days post-treatment. While no alteration in leukocyte parameters was detected between control and rGO-treated animals, time-dependent leukocytosis (rGO-1 h versus rGO-3 h) and leukopenia (rGO-3 h versus rGO-7 days) was observed intra-treated groups. Nevertheless, no inflammatory response was induced in serum and hippocampus at any time.

Conclusions: The toxic effects seemed to be peripheral and transitory in the short-term analysis after systemic administration of rGO. The effects were self-limited and non-significant even at 7 days post-rGO administration.

Keywords: Nanoparticles, Blood–brain barrier, Toxicity

Background

Graphene is a single layer of densely packed, regular sp^2 -bonded carbon atoms arranged in a hexagonally two-dimensional structure [1]. Graphene and derivatives, such as graphene oxide (GO) and reduced graphene oxide (rGO), have attracted significant interest in many technological fields due to their unique electronic, optical, magnetic, thermal and mechanical properties. These properties have led to broad-spectrum material and biomedical applications, such as the use in biosensors,

optical imaging, drug/gene delivery, photothermal therapy and tissue engineering [2–6].

With regard to rGO, the results of toxicological studies appear to be inconclusive, as there is no broad consensus on whether it is non-toxic and biocompatible [7–9]. These discrepancies have been attributed to many aspects related to the physicochemical properties (e.g., size, shape, surface chemistry, composition and aggregation) of the nanomaterial [10], and the experimental design used [11].

In our pioneer work with rGO, we demonstrated that rGO administered intravenously (i.v) through the tail vein of rats was further detected inside the brain tissue and particularly concentrated in the thalamus and hippocampus. We also found that Evans blue vital stain

*Correspondence: monique.cpm@gmail.com; hofling@unicamp.br

¹ Department of Pharmacology, Faculty of Medical Sciences, State University of Campinas, Campinas, SP 13083-881, Brazil

Full list of author information is available at the end of the article



infusion in rGO-treated rats escaped from the peripheral circulation and entered the brain, indicating blood-brain barrier (BBB) disruption. With focus in hippocampus, we found that the possible entrance door of rGO into this brain region might have been in the course of a transient downregulation of the junctional proteins of the capillary endothelium [12]. The elaborate organization of such proteins maintains tightly attached to each other the capillary endothelial cells preventing the passage of substances through the paracellular pathway [13]. Such temporary decrease of the paracellular tightness of the BBB, the presence of rGO inside the hippocampus and the unnoticeable negative effect to animals' exploratory behavior was predictor of a positive outcome in studies related to the toxicity of rGO.

In general, the toxicity of nanomaterials has been evaluated through their capacity to interfere in cellular mechanisms related to allergy, fibrosis, organ failure, hemocompatibility, neurotoxicity, nephrotoxicity and hepatotoxicity [14].

In the present study, we used the same experimental design and animal model as in our previous study [12] to delineate a possible toxic profile of rGO. The focus of the study was the hippocampus, and the peripheral organs (blood, kidney and liver) recognized as impact organs against xenobiotics. The purpose of the present study was to expand the understanding of rGO-tissue interactions *in vivo*, promoting safe and responsible use of rGO-based technology for future therapeutic application studies.

Results and discussion

rGO did not induce clinical signs of neurotoxicity in rats

A clinical evaluation was performed in rats before and after rGO injection in search of possible evidence of side-effects. Signs of tremor, piloerection, salivation, lacrimation, dyspnea, convulsions, hindlimb and forelimb grip strength, or other motor abnormalities were examined as symptoms of neurotoxic insult [15]. Animals from the rGO-treated groups did not show any of the signs described in Table 1 at any of the time-frame of the study (15 min, 1, 3 h and 7 days). The liveliness and exploratory

behavior, typical of healthy rats, was equally observed in the control and rGO-treated animals.

Differently, Zhang and collaborators [16] reported that rGO nanosheets orally administered to mice caused a short-term decrease in locomotor activity and neuromuscular coordination. Other signs such anxiety-like, exploratory, or spatial learning and memory behaviors remained unnoticed. We suggest that the differences in relation to our findings are attributed to some aspects: (1) while we administered a single *i.v.* dose (7 mg/kg) to rats, Zhang et al. used high-dose (60 mg/kg administered orally for five consecutive days) to mice; (2) while our rGO was 342 ± 23.5 nm in size, theirs were small (87.97 ± 30.83) and large-sized (472.08 ± 249.17 nm). We conclude that experimental design, animal model and physicochemical characteristics of the nanomaterials have a key role in the development of toxic manifestations.

rGO did not alter the neuronal viability marker and did not promote astrogliosis in the hippocampus of rats

Since rGO *i.v.* administration was shown to downregulate the junctional proteins responsible for the tight apposition of the endothelial cells of the BBB and was detected inside the brain [12], the next step was to investigate possible neurotoxic effects in the tissue. Firstly, we performed a histological evaluation of hematoxylin-eosin-stained hippocampus in search of tissue damage, inflammation or necrosis. Secondly, we evaluated the nuclear antigen protein (NeuN)—a marker of neuron maturation and viability—and the glial fibrillary acidic protein (GFAP), a protein of the intermediate filament of astrocytes and a marker of reactivity by triggering mechanical strength of the glia cytoskeleton in response to noxious stimuli to the brain. The relevancy of analyzing neurons and astrocytes rely on the fact that together with capillary endothelial cells and pericytes they constitute the neurovascular unit, a concept highlighting the functional cell–cell interactions which support BBB function [17, 18].

The histological analysis of the hippocampus of treated animals showed that morphologically it did not differ

Table 1 Summary of clinical signs and behavioral response destined to evaluate neurotoxicity before and after rGO *i.v.* administration (7 mg/kg)

Autonomic nervous system	Peripheral nervous system (neuromuscular)	Behavioral (activity)	Central nervous system (excitability)
Lacrimation	Righting reflex	Motor activity	Clonic movements
Salivation	Hindlimb grip strength	Home cage posture	Tonic movements
Excretion	Forelimb grip strength	Rearing	
Piloerection			

All the parameters evaluated in rGO-treated rats showed no discrepancy relative to the observed in rats treated with vehicle (control)

n = 3–5 per time of sampling; n = 5 control group

from that observed in the control group regardless of the time following administration of rGO (Fig. 1a, b). Considering the neurons, NeuN immunolabeling showed that the nucleus of pyramidal neurons of the *Cornu ammonis* (CA) subfields (Fig. 1c, d) and the granule neurons of the dentate gyrus (not shown) of the hippocampus were typically reactive, not differing among treated and control animals. However, the NeuN content evaluated by immunoblotting in the hippocampal homogenates of rGO-treated animals (Fig. 1g) showed an immediate but episodic rise of 37 % ($p < 0.05$) in the protein expression level at 15 min. Thereafter, at 1, 3 h and 7 days NeuN immunolabeling and protein content returned to control basal levels. It is probable that a feeble mechanism of neurotoxicity had been immediately triggered after rGO injection, but it did not result in major change in the expression of NeuN. The increases in NeuN expression suggests enhanced or at least maintained neuronal viability. In addition, it means hippocampus plasticity, in which transitory migration of neurons may occur in response to local insult, resulting in fleeting increases of NeuN level.

With regard to the hippocampal astrocytes, a possible reaction against rGO would be by hypertrophy of the cytoskeleton and/or cell hyperplasia, a process known as reactive gliosis or astrogliosis [19]. Figure 1 illustrates GFAP labeling in the hippocampal CA1 region of a rat treated with a vehicle (panel E) and 15 min after rGO administration (panel F). Regardless of time post-rGO exposure, we observed soma and processes of the hippocampal astrocytes GFAP-positive, similar to that observed in control group. Likewise, the other hippocampal subfields, CA2, CA3, and dentate gyrus showed no difference between rGO-treated and control animals (data not shown). Quantitative analysis of the hippocampal homogenate by western blotting showed that treatment with rGO resulted in no significant alterations in GFAP levels over time, revealing absence of reactive astrogliosis (Fig. 1h). This indicates that rGO systemic injection did not induce substantial reactive response in astrocytes.

rGO did not alter hematological parameters relative to control

In order to retain their engineered functions in vivo, nanomaterials used for biomedical applications should be

compatible with blood [8]. No significant changes in any of the hematological parameters were observed in comparison with the control group. However, intra-group analysis revealed differences in the number of white blood cells (WBC) (Table 2). The rGO-3 h group showed a 59 % increase in the number of WBC relative to the rGO-15 min group, thus characterizing a time-dependent intra-rGO group leukocytosis ($p < 0.05$). This effect was transient as it was followed by a 115 % decrease when comparing the rGO-3 h group with the rGO-7 day group, hence characterizing an intra-rGO group time-dependent leukopenia ($p < 0.01$). All the other parameters showed steady figures over time with values at 7 days practically the same as those exhibited by control group.

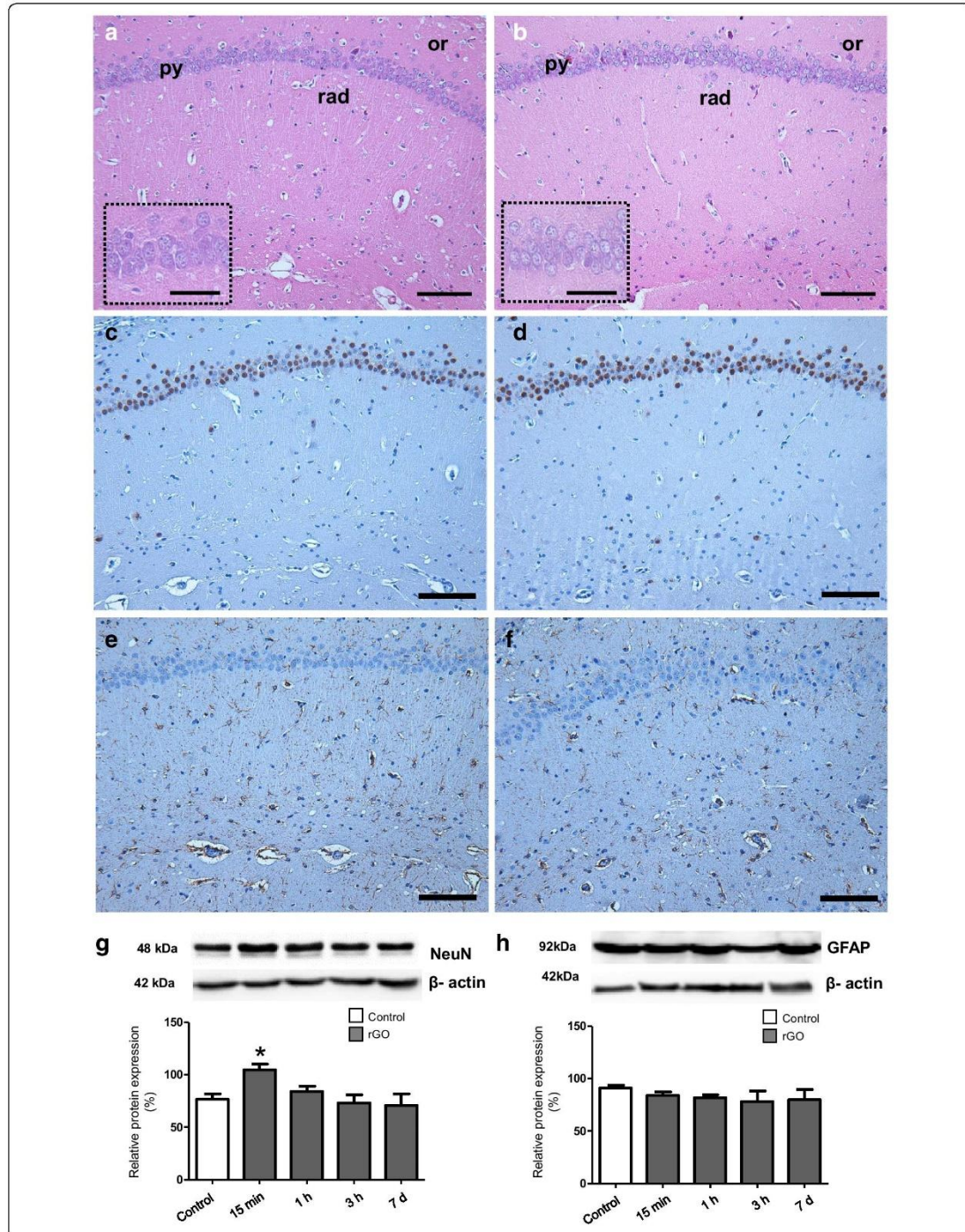
It has been demonstrated that graphene-based nanomaterials were compatible with blood and did not cause hemolysis, platelet activation and changes in coagulation or abnormalities in hematological parameters [20]. In contrast, Singh et al. [21] reported that intravenous administration of GO (250 $\mu\text{g}/\text{kg}$ body weight) caused strong platelet aggregation and extensive thromboembolism in mice. Interestingly, much less platelet aggregation occurred with rGO, which may be correlated to difference in surface charge distribution from GO as the same concentration and animal model were used.

In rodents, several types of stimulus such as exercise, environmental factors, nutrition (food and water) and inflammatory response [22], can influence WBC levels [23]. In comparison with the control group, our results showed that rGO-treated animals did not alter significantly leukocytes number. The variability seen among rGO groups on WBC counts might be considered rather moderate, as the values observed here are still within the reference ranges found in rats [23, 24].

To confirm that the time-dependent leukocytosis (from 15 min to 3 h) did not represent an inflammatory reaction in response to rGO we assessed the levels of interleukin 6 (IL-6) and tumor necrosis factor- α (TNF- α) pro-inflammatory cytokines in serum (ELISA assay) and the expression of TNF- α and interferon- γ (IFN- γ) in the hippocampal homogenates (WB data). IL-6 and TNF- α was undetectable in the serum of rGO-treated rats. All samples measured less than the lowest rat standard levels, 62.5 pg/mL for IL-6 and 125 pg/ml for TNF- α . Likewise,

(See figure on next page.)

Fig. 1 Light micrographs of CA1 hippocampal subfield of rats 1 h after i.v. injection of vehicle (**a**) and 15 min after i.v. injection of rGO (**b**), Hematoxylin-eosin. Insets show greater magnification of hippocampal pyramidal neurons with preserved euchromatic nuclei and visible nucleoli both in control and treated samples. Or *stratum oriens*; Py *stratum pyramidale*; Rad *stratum radiatum*. NeuN and GFAP labeling of 1 h-control rats (**c**, **e**) and 15 min after i.v. injection of rGO (**d**, **f**), respectively. Western blot signals of NeuN (**g**) and GFAP (**h**) after administration of rGO (7 mg/kg) in hippocampal tissue lysates were quantified densitometrically and normalized to an internal standard protein (β -actin). The results were shown as a percentage of control (100 %), and represent mean \pm SEM ($n = 5$ rats/interval). * $p < 0.05$ indicates significant difference relative to control. One-way ANOVA, Bonferroni post hoc test; Bars 100 μm (**a-f**), 50 μm (insets)



no significant change was observed in the expression of either inflammatory marker over time (Fig. 2). Based on these results and in the absence of inflammatory cell infiltration (Fig. 1b), it appears that the increase in the number of WBC cells intra-rGO-treated groups cannot be associated to any inflammatory process.

Morphological and functional evaluations show minimal effects of rGO in liver and kidney

To better analyze the safety of using rGO, hepatotoxicity and nephrotoxicity were evaluated to determine whether or not rGO caused alterations in liver and kidney morphology and function. These organs are important components for detoxification and clearance of nanoparticles, respectively [25].

rGO systemic administration did not produce detectable changes in the lobular architecture of the liver, which was preserved and remained normal in all treated rats at the studied time-frame (Fig. 3a, b) even 7 days after rGO administration (data not shown). Likewise, no immunopositive apoptotic cells were detected (Fig. 3c, d). Typically, collagen fiber density was only visible in the hepatic portal venous system and this was unchanged in control and rGO-treated tissue (insets Fig. 3e, f); equally no alterations in the connective tissue were detectable in the peri-sinusoidal space in rGO-treated samples stained with Masson's trichrome (Fig. 3f) compared to control (Fig. 3e). The data suggest that in these experimental conditions there were absence of hepatocytes apoptosis and tissue fibrosis.

Table 2 rGO effects on hematological parameters of male Wistar rats

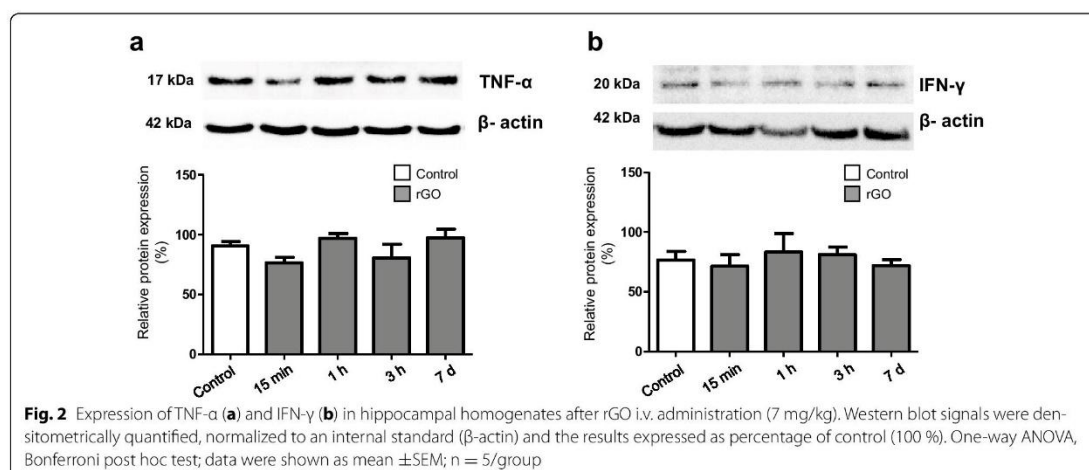
Group	Unit	Control	rGO 15 min	rGO 1 h	rGO 3 h	rGO 7 days
RBC	$10^6/\mu\text{l}$	7.32 ± 0.09	7.16 ± 0.17	7.45 ± 0.02	7.27 ± 0.11	7.48 ± 0.04
Hb	g/dl	14.27 ± 0.24	13.73 ± 0.12	14.37 ± 0.14	14.00 ± 0.24	14.32 ± 0.37
Hct	%	46.87 ± 0.52	46.13 ± 0.88	48.83 ± 0.57	47.58 ± 0.24	47.70 ± 0.40
MCV	fl	64.00 ± 0.60	64.60 ± 0.23	65.53 ± 1.02	65.44 ± 0.66	63.44 ± 0.49
MCH	pg	19.03 ± 0.23	19.03 ± 0.32	19.27 ± 0.24	19.22 ± 0.21	19.24 ± 0.26
MCHC	g/dl	29.80 ± 0.40	29.57 ± 0.40	29.43 ± 0.08	29.42 ± 0.42	30.38 ± 0.33
PLT	$10^3/\mu\text{l}$	638.3 ± 5.84	650.0 ± 6.92	649.0 ± 10.69	624.2 ± 25.81	636.2 ± 59.19
WBC	$10^3/\mu\text{l}$	7.63 ± 0.60	$6.80 \pm 1.41^*$	7.10 ± 0.30	$10.83 \pm 0.55^{* \#}$	$5.03 \pm 0.56^{\#}$

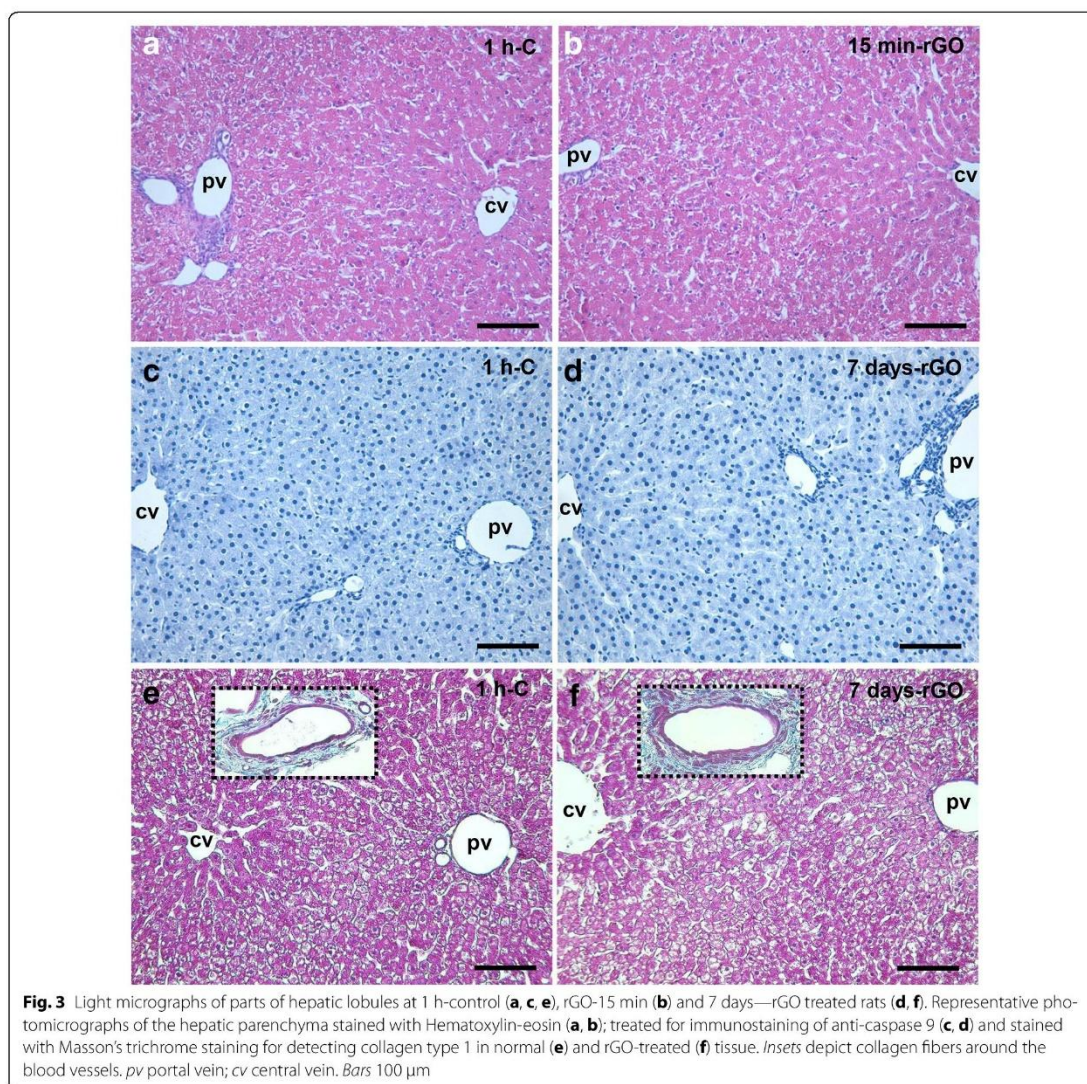
The same symbol in each column indicates a significant difference between groups

One-way ANOVA, Bonferroni post hoc test; data were shown as mean \pm SEM, $n = 3-5$ in each group

RBC red blood cell; Hb hemoglobin; Hct hematocrit; MCV mean corpuscular volume; MCH mean corpuscular hemoglobin; MCHC mean corpuscular hemoglobin concentration; PLT platelet; WBC white blood cell

* $p < 0.05$; # $p < 0.01$





With regard to kidneys, the tubular, glomerular tufts and renal corpuscles and interstitium of rGO-treated rats were normal in appearance and did not differ from control (Fig. 4a, b). Caspase-9 immunostaining allowed identifying dispersed nephron segments with apoptotic cells (brown-labeled cells) both in control (Fig. 4c) and rGO-treated rats (Fig. 4d). As is common, the renal parenchyma shows minimal connective tissue support in physiologic condition (Fig. 4e), and no alteration was apparent in rGO-treated animals (Fig. 4h).

Additionally, we evaluated the levels of aminotransferases, alanine aminotransferase (ALT) and aspartate aminotransferase (AST), in serum, as in drug safety studies these enzymes are key indicators of drug-induced liver toxicity involving laboratory animals and patients. These enzymes are abundant within hepatocytes and catalyze the formation of glutamate through the transfer of an amino group [26]. Thus, increased levels of these enzymes in the blood are one of the first laboratory signs of hepatic dysfunction. As shown in Table 3, no alteration

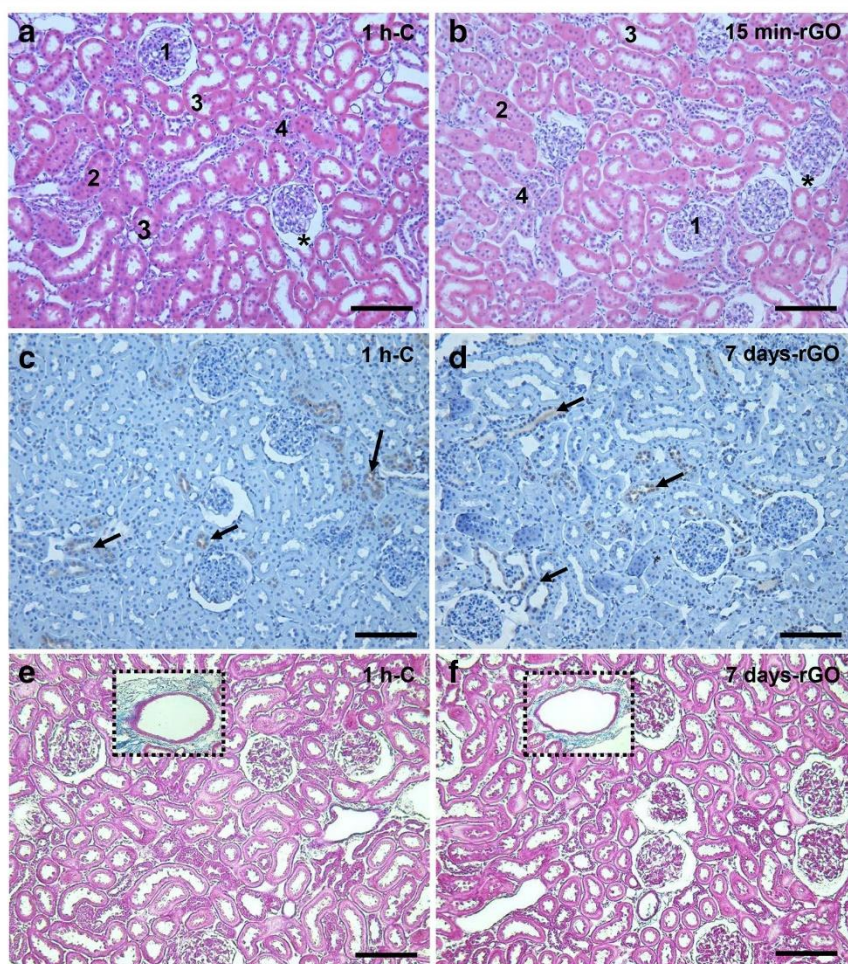


Fig. 4 Renal cortical sections stained with Hematoxylin-eosin (**a, b**), immunostained for caspase 9 (**c, d**) and stained with Masson's trichrome (**e, f**). The sections were obtained from vehicle-treated (control—1 h) rats (**a, c, e**) and 15 min (**b**) and 7 days (**d, f**) after intravenous injection of rGO. Note that there is no change between the aspect of control and rGO-treated sections in each of the staining assessments. The widening of the tubular lumen and capsular space was observed in control and rGO samples due to perfusion fixation. *Insets* depict that collagen density (just in large blood veins of renal stroma) was the same for control and rats treated with rGO. 1 Renal glomeruli; 2 proximal tubule; 3 distal tubule; 4 collecting tubule; * Bowman's space of the renal corpuscle. *Arrows* point to the immuno-positive apoptotic cells (*brown*). *Bars* 100 μm for all panels

was found in the enzyme levels in comparison with control over the time-frame scheduled.

Next, renal glomerular function was estimated by assessing creatinine and blood urea nitrogen (BUN) levels, two markers of renal function [27]. We did not observe alterations in creatinine levels; but found a transitory and unexpected 37 % decrease in BUN levels at 3 h in the rGO-treated animals, compared with the control group ($p < 0.05$, Table 3). Decreases in BUN level were

also found as time post-rGO exposure advanced: 27 % ($p < 0.05$) decrease in rGO-15 min versus rGO-1 h and 63 % ($p < 0.001$) decrease in rGO-15 min versus rGO-3 h. One week after rGO treatment, BUN levels had returned to the control rate, which may indicate that in case of hepatotoxicity or nephrotoxicity occurrence they were short-lived. Moreover, the histopathological examination of kidney and liver morphology showed none abnormality in the rGO-treated group.

Table 3 Effects of rGO on biochemical parameters of hepatic and renal function

	Unit	Control	rGO 15 min	rGO 1 h	rGO 3 h	rGO 7 days
ALT	U/L	44 ± 3.5	56 ± 3.9	54 ± 0.5	44 ± 3.2	48 ± 2.3
AST	U/L	148 ± 9.9	177 ± 8.4	152 ± 7.5	156 ± 9.5	151 ± 6.6
BUN	mg/dL	48 ± 2.2 [#]	57 ± 3.2 ^{#,∇}	45 ± 3.3 [*]	35 ± 0.7 ^{#,∇}	48 ± 1.8
Creatinine	mg/dL	0.31 ± 0.003	0.35 ± 0.017	0.29 ± 0.021	0.30 ± 0.017	0.34 ± 0.020

Values are mean ± SEM of 3–5 animals in each group. The same symbol in each column indicates a significant difference between groups

One-way ANOVA, Bonferroni post hoc test

ALT alanine aminotransferase; AST aspartate aminotransferase; BUN blood urea nitrogen

^{#,*} p < 0.05; [∇] p < 0.001

BUN analysis also provides information about hepatic functioning, as the nitrogen from ammonia produced by the liver will participate in urea formation which will be further excreted by the kidney as a waste metabolism product. Increases in BUN levels indicate that either the kidney or the liver may not be functioning properly. In humans, low levels of BUN have been observed in several morbid conditions such as those caused by trauma, surgery, malnutrition and opioids and anabolic steroid use and fluid excess [27, 28], whereas low levels are not common and not usually reported in animals.

Evaluation of oxidative stress and DNA damage generated by rGO

As one of the most important mechanisms explored in graphene-based nanomaterials studies, oxidative stress has been the focus of toxicological studies [9, 29]. It is well known that the generation and elimination of reactive oxygen species (ROS) is dynamically balanced inside cells, and severe increases in ROS levels may induce genotoxicity, protein inactivation, lipid peroxidation, mitochondrial dysfunction, and eventually cell death by apoptosis or necrosis [30–32].

Herein, the influence of rGO in the response of biomarkers of oxidative stress was assessed through the expression and activities of the antioxidant enzymes superoxide dismutase (SOD) and catalase (CAT), known to be involved in the detoxification of hydrogen peroxide (H₂O₂). SOD converts the superoxide radical into H₂O₂

while CAT converts H₂O₂ into water [33]. We further evaluated the thiobarbituric acid reactive substances (TBARS), as a marker of lipid peroxidation.

rGO systemic single injection induced upregulation in serum SOD activity, while CAT activity was unaffected. Likewise, no significant differences were detected in serum TBARS levels between rGO-treated and control animals, indicating that lipid peroxidation was unaltered (Table 4). SOD activity rose progressively from 15 min up to 7 days. Relative to control, SOD activity increased at 1 h (54 %, p < 0.05) and at 7 days (69 %, p < 0.01), after the injection of rGO. Intra-group analysis revealed a significant increase (57 %, p < 0.01) in rGO-7 days relative to rGO-15 min.

Western blot analyses did not show significant difference in SOD-1 or CAT protein expression over the time course analyzed (Fig. 5a, b), suggesting that rGO did not alter transduction signal.

Therefore, we decided to investigate whether the generation of oxidant compounds by systemic rGO injection, as inferred by the increase in the SOD activity, had induced genotoxicity and cell death under the influence of rGO.

As shown in Table 5, rGO did not induce cytogenetic damage. There was no difference in the frequency of micronucleated erythrocytes in the circulating blood of control rats and in the blood collected from rats 7 days after a single i.v. injection of rGO. In human glioblastoma cell lines U87 and U118, GO and rGO decreased cell

Table 4 rGO effects on serum SOD, catalase and TBARS levels in male Wistar rats

	Unit	Control	rGO 15 min	rGO 1 h	rGO 3 h	rGO 7 days
SOD	U/ml	13 ± 0.4 ^{#,*}	14 ± 0.8 [∇]	20 ± 0.6 [#]	20 ± 2.6	22 ± 1.1 ^{#,∇}
CAT	nmol/min/ml	129 ± 2.8	151 ± 12.5	112 ± 28.8	88 ± 17.3	120 ± 6.1
TBARS	nmol/ml	7.6 ± 1.0	7.7 ± 1.7	7.4 ± 2.4	6.2 ± 0.3	5.7 ± 1.3

Values are mean ± SEM of 3–4 animals in each group. The same symbol in each column indicates a significant difference between groups

One-way ANOVA, Bonferroni post hoc test

SOD superoxide dismutase; CAT catalase; TBARS thiobarbituric acid reactive substances

[#]p < 0.05; [∇]p < 0.01

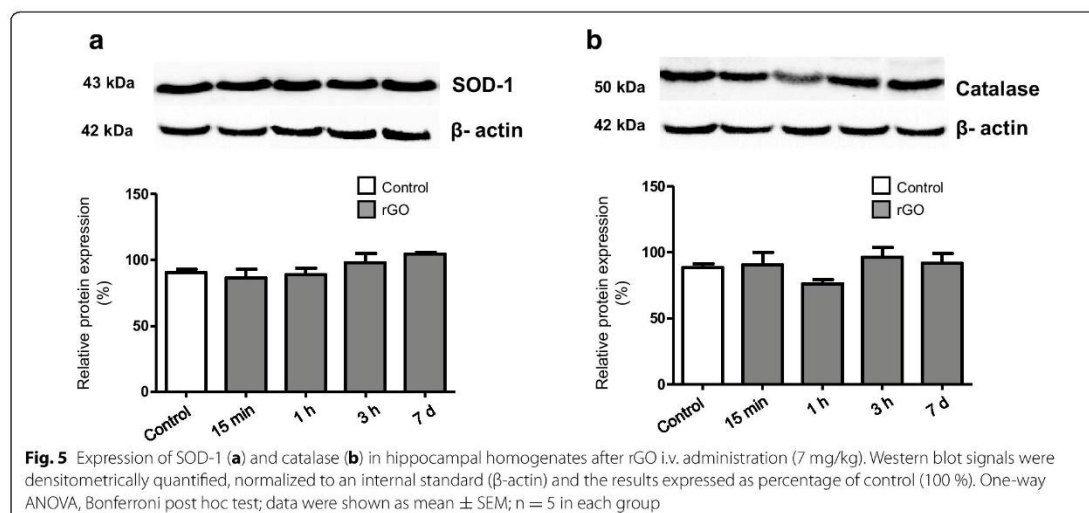


Table 5 Effect of rGO on the frequency of polychromatic erythrocytes with micronuclei in the peripheral blood and caspase-3 expression

	Control	rGO 15 min	rGO 1 h	rGO 3 h	rGO 7 days
Micronucleus index	0.68 ± 0.13	NA	NA	NA	0.64 ± 0.19
Caspase 3	92.46 ± 2.88	101.3 ± 11.66	91.71 ± 8.00	89.05 ± 15.99	95.97 ± 14.46

Protein expression levels were expressed as percentage of control (100 %) after normalization to an internal standard (β-actin). One-way ANOVA, Bonferroni post hoc test; data were shown as mean ± SEM; n = 5 in each group

NA not assessed

viability and proliferation, however rGO was more toxic than GO. In rGO-treated U87 tumors the expression of caspase-3 was 96 % higher compared with controls [34]. Herein, no substantial differences were observed in caspase 3 levels in the hippocampal homogenates between controls and animals treated with rGO.

We suggest that induction of oxidative stress by rGO was moderate and that the reductive defense system provided by SOD activity was triggered to restore the oxidant/antioxidant balance.

Conclusions

Overall, the intravenous administration of rGO (7 mg/kg single dose) led to minor signs of toxicity in the blood, liver and kidney after 7 days with no sign of inflammation process in course. These effects were transitory and did not lead to permanent damage. Also, no perceptible change was observed in hippocampal neurons or astrocytes response, despite a previous study demonstrating BBB disruption and detecting rGO distribution inside this brain region [12]. The activity of control and rGO-treated animals in their cages was the same, with no

apparent clinical signs of toxic manifestation. In conclusion, the data suggests that systemic administration offers no significant health risk for rats in these experimental conditions. Nevertheless, it seems clear that the interactions between graphene-based materials with biological systems are highly dependent on the experimental design used and the physicochemical properties of the nanomaterial. For the development of graphene-based nanomedicine, it is important the development of systematic toxicological investigations to fully understand the biological effects and address safety concerns before the practical application of any graphene-based materials in the clinic. The present study provides a basis for further toxicological studies of rGO after long-term in vivo exposure, and is an incentive for studies of the mechanisms underlying rGO and cell/biological system interaction.

Methods

Preparation and characterization of rGO

The processing for rGO was the same described before to maintain identical properties as the used in our previous study [12]. Briefly, rGO was prepared after catalytic

conversion using a copper substratum to which was added 1 ml of polyaniline diluted in dimethylformamide (Synth, São Paulo, SP, Brazil), after which it was allowed drying for 2 h at room temperature. After, 0.2 ml of nickel nitrate dissolved in pure acetone (Synth) was added to the preparation which was subsequently placed within a chemical vapor deposition reactor assisted by a hot filament. The hydrocarbons used as a carbon source were camphor and acetone. Raman spectrometry (Renishaw, Wotton-under-Edge, UK) for molecular structure characterization, Field Emission Scanning Electron Microscopy (JEOL JSM-6330F, Japan) for morphological description and dynamic light scattering for measurement of size, zeta potential and polydispersity index (PDI) (ZetaPALS Zeta Potential Analyzer, Brookhaven Instruments, NY, USA) confirmed that rGO characteristics were the same exhibited in our previous study (sized 342 ± 23.5 nm, -25 ± 0.18 mV zeta potential, 0.56 ± 0.03 PDI).

In this work, we performed additional information about physicochemical properties of rGO. The average thickness of the rGO sheet measured by Field Emission Scanning Electron Microscope (FE-SEM) (Zeiss Supra 55 VP-SEM) was estimated to be ~ 5 nm (Fig. 6a). rGO showed remarkable stability in water and different physiological solutions including 0.9 % saline solution, Dulbecco's Modified Eagle Medium (DMEM), and bovine serum albumin (BSA) (Fig. 6b).

Animal treatment

Experiments were carried out in accordance with the Brazilian Society of Laboratory Animal Science guidelines and approved by the Institutional Committee for Ethics in Animal Use (CEUA/IB/UNICAMP, protocol n. 2884-1). The experimental animals used in our previous study [12] were the same used in the present one. We used healthy male Wistar rats (average weight 180–220 g;

6 weeks old; $n = 3-5$ in each group) for evaluating the nanotoxicity of rGO.

Animals (*Rattus norvegicus*) received a single tail vein injection of rGO (7 mg/kg dose; concentration of 1 mg/ml) [35], while the control group was given the same volume of vehicle (sterile distilled water). Fifteen minutes, 1, 3 h and 7 days after the i.v. administration of rGO, the animals were euthanized by carbon dioxide (CO_2) inhalation (western blotting analysis) or anesthetics overdose [3:1 mixture of ketamine chloride (Dopalen[®], 100 mg/kg body weight, Fortvale, Valinhos, SP, Brazil) and xylazine chloride (Anasedan[®], 10 mg/kg body weight, Fortvale)] and the target samples (blood, brain, liver and kidneys) immediately removed. Animals of the control group received an i.v. injection of vehicle and were euthanized 1 h later. A single control group was used as preliminary experiments showed no time difference relative to data.

Neurotoxicity evaluation

The clinical and behavioral signs were evaluated in control and rGO-treated rats using the functional observation battery described by Moser [36]. All observations were performed by the same trained observer who was unaware of treatments.

Systemic toxicological profile of rGO

Fifteen minutes, 1, 3 h and 7 days after treatment with rGO, the animals were deeply anesthetized and blood samples were collected via cardiac puncture immediately prior to transcardial perfusion and divided into two parts, (1) collected into EDTA-containing tubes and used for hematological and genotoxicity studies, and (2) collected into serum separator gel tubes and used for enzyme-linked immunosorbent assay (ELISA), biochemical studies and analysis of the activity of antioxidant enzymes.

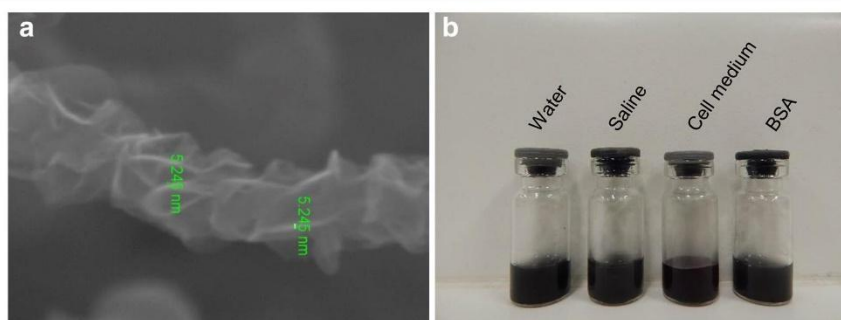


Fig. 6 FE-SEM image of rGO sheet with a thickness of ~ 5 nm (a). rGO suspension in water, 0.9 % saline, DMEM cell medium and BSA displaying great stability (b)

Hematological studies

Hematological parameters—numbers of red blood cells, hemoglobin, hematocrit, mean cell volume, mean corpuscular hemoglobin, mean corpuscular hemoglobin concentration, platelet and white blood cell count—were determined using an automated hematology analyzer (Coulter T540 hematology system; Fullerton, CA, USA).

ELISA

Blood samples were centrifuged for 10 min at 3000 rpm and the resulting serum was stored at -80°C . The cytokines IL-6 and of TNF- α were determined using Rat DuoSet ELISA kits (R&D Systems; Minneapolis, MN, USA) following the instructions supplied by the manufacturer. The limit of detection of these kits was 125 pg/ml for IL-6 and 62.5 pg/ml for TNF- α .

Biochemical parameters

The blood samples for biochemical analyses were centrifuged at 3000 rpm for 10 min, the serum aspirated and analyzed by an automated analyzer Cobas[®] 6000 (Roche Diagnostics, Mannheim, Germany) for the determination of AST and ALT activities and the concentration of BUN and creatinine.

Antioxidant enzymes activity and lipid peroxidation evaluation

Lipid peroxidation was evaluated using TBARS technique described by Ohkawa, Ohishi, and Yagi [37] and adapted by Batista et al. [38], in which malondialdehyde and the final products of lipid peroxidation react with thiobarbituric acid, forming a pink-colored complex.

The enzyme antioxidant systems (SOD and CAT) in the serum samples were measured using colorimetric methods. The SOD activity in serum was obtained after reaction with hypoxanthine, nitroblue tetrazolium and 0.07 U of xanthine oxidase as described in detail before [38].

The CAT activity method was carried out based on the reaction of the enzyme with methanol and H_2O_2 . Purpald (4-amino-3-hydrazino-5-mercapto-1,2,4-triazole) was used as chromogen and the resultant formaldehyde products was measured at 540 nm (adapted from [39]).

Genotoxicity assay

The genotoxic potential of rGO was evaluated by micronuclei assay in peripheral blood. The assay was performed in accordance with the Redbook 2000: IV.C.1.d Mammalian Erythrocyte Micronucleus Test [40]. Briefly, after fixation in methanol for 10 min, three good-quality smears prepared from each blood sample ($n = 3$ blood samples; total $n = 9$ smear slide/time) were left to air-dry, stained with Leishman solution for 12–15 min and

then analyzed using an Olympus BX51 photomicroscope (Japan) at 400 \times or 1000 \times magnification, as required.

From each smear slide, the frequency of micronuclei were determined by counting a total of at least 1000 erythrocytes and expressed as per 1000 cells (%). Since the occurrence of possible mutagenesis was not observable at earlier periods of times (15 min, 1 and 3 h), the analysis was solely performed in the 7 day-samples.

Histopathological and immunohistochemistry assessment

Immediately after blood collection, the rats were perfused with physiological saline followed by 4 % paraformaldehyde in 0.1 M PBS, pH 7.4. The brains and peripheral organs (liver and kidney) of rGO-injected rats and controls were removed and routinely processed for paraffin embedding [41]. Coronal 5 μm thick sections of brain, liver and kidney were stained with Hematoxylin-eosin for histological evaluation, Masson's trichrome technique to visualize collagen fibers or immunostained using primary antibodies (see Table 6) using standard protocols. Briefly, the endogenous peroxidase activity was quenched with 3 % hydrogen peroxide, (two cycles of 10 min) and epitope retrieval was accomplished with 10 mM sodium citrate buffer, pH 6.0, in a steamer ($95-99^{\circ}\text{C}$) for 30 min. Non-specific antigen binding was blocked with 5 % skimmed milk powder for 1 h. Slides were incubated with the primaries antibodies for 16–18 h in a humidified chamber at 4°C . After washing twice with phosphate-buffered saline (PBS, pH 7.4), the slides were incubated with biotinylated anti-rabbit secondary antibody (EnVision_HRP link, Dako Cytomation, CA, USA) for 30 min at room temperature. Color was developed with a diaminobenzidine chromogenic solution (DAB+, Dako Cytomation) and nuclei were counterstained with Harry's hematoxylin; after ethanol dehydration slides were mounted in Canada balsam. Negative control was done by replacing the primary antibody with 1 % PBS-bovine

Table 6 Primary antibodies used in this study

Antibody	Dilution	Supplier	Reference	Application
Caspase 3	1:400	Santa Cruz	Sc-7148	WB
Caspase 9	1:50	Sigma Aldrich	C7729	IHC
Catalase	1:400	Santa Cruz	sc-271242	WB
GFAP	1:100	Dako	Z0334	IHC
GFAP	1:500	Dako	Z0334	WB
IFN- γ	1:500	Santa Cruz	sc-9344	WB
NeuN	1:500	Merck Millipore	ABN78	IHC
NeuN	1:1000	Merck Millipore	ABN78	WB
SOD-1	1:500	Santa Cruz	sc-11407	WB
TNF- α	1:1000	Cell signaling	#11948	WB
β -Actin	1:1000	Sigma Aldrich	A2228	WB

serum albumin. Images were captured on an Olympus BX51 photomicroscope (Japan).

Western blotting

Western blotting was performed in hippocampal homogenates ($n = 5$ for each time, including single control) as previously described [12]. After electrotransfer, the membranes were incubated with 5 % skimmed milk powder to block non-specific sites prior followed by washing with TBS-T (0.1 % Tris-buffered saline with 0.05 % Tween 20, pH 7.4). Subsequently, the membranes were incubated with primary antibodies (see Table 6). Then, the membrane were washed with TBS-T and incubated with HRP-labeled anti-mouse (for anti-catalase and anti- β -actin), anti-goat (for anti-IFN- γ) or anti-rabbit (anti-caspase 3, SOD-1, anti-GFAP, anti-NeuN and anti-TNF- α) secondary antibody (1:1000, Sigma Aldrich). Bands were visualized using a chemiluminescence kit (Super Signal West Pico Chemiluminescent Substrate; Pierce Biotechnology, Rockford, IL, USA) according to the manufacturer's instructions. The luminescent signal from bands was captured by a G:BoxiChemi camera (Syngene, Cambridge, UK) and band intensities were quantified using Image J 1.45S (NIH, Bethesda, MD, USA). Blots were stripped and reprobed for β -actin to monitor protein loading the efficiency of blot transfer, and non-specific changes in protein levels.

Statistical analysis

One-way ANOVA followed by Bonferroni post hoc test was performed for multiple variant analyses. Differences were considered statistically significant at $p < 0.05$. All values were expressed as the mean \pm standard error of the mean (SEM). All analyses were done using Prism software, version 5 (GraphPad Inc., La Jolla, CA, USA).

Abbreviations

ALT: alanine aminotransferase; AST: aspartate aminotransferase; BBB: blood-brain barrier; BUN: blood urea nitrogen; CA: *cornu ammonis*; CAT: catalase; ELISA: enzyme-linked immunosorbent assay; GFAP: glial fibrillary acidic protein; GO: graphene oxide; Hb: hemoglobin; Hct: hematocrit; IFN- γ : interferon- γ ; IL-6: interleukin-6; MCH: mean corpuscular hemoglobin; MCHC: mean corpuscular hemoglobin concentration; MCV: mean corpuscular volume; NeuN: nuclear antigen protein; PDI: polydispersity index; PLT: platelet; RBC: red blood cell; rGO: reduced graphene oxide; ROS: reactive oxygen species; SOD: superoxide dismutase; TBARS: thiobarbituric acid reactive substances; TNF- α : tumor necrosis factor- α ; WBC: white blood cell.

Authors' contributions

HJC carried out the nanomaterial synthesis. AGB and MRMJ carried out oxidative stress experiments, SPI carried out genotoxicity analysis and MARV performed ELISA assay. MCPM, ESS, MBJ and MACH designed and performed experiments, analyzed data and wrote the paper. All authors discussed the results and commented on the manuscript. All authors read and approved the final manuscript.

Author details

¹ Department of Pharmacology, Faculty of Medical Sciences, State University of Campinas, Campinas, SP 13083-881, Brazil. ² Department of Biochemistry and Tissue Biology, Institute of Biology, State University of Campinas, Campinas, SP, Brazil. ³ Department of Semiconductors, Instruments and Photonics, School of Electrical and Computer Engineering, State University of Campinas, Campinas, SP, Brazil. ⁴ Faculty of Technology of Sorocaba, State Center of Paula Souza Technological Education, Sorocaba, SP, Brazil. ⁵ Department of Food and Nutrition, State University of Campinas, Campinas, SP, Brazil. ⁶ Department of Genetics, Evolution and Bioagents, Institute of Biology, State University of Campinas, Campinas, SP, Brazil.

Acknowledgements

This work was supported by the Brazilian funding agencies Fundação de Amparo à Pesquisa do Estado de São Paulo (FAPESP) (Grant 2012/24782-5) and Conselho Nacional de Desenvolvimento Científico e Tecnológico (CNPq) (Grant nos. 305099/2011-6 and 486142/2012-4).

Competing interests

The authors declare that they have no competing interests.

Received: 3 February 2016 Accepted: 14 June 2016

Published online: 24 June 2016

References

- Novoselov KS, Geim AK, Morozov SV, Jiang D, Zhang Y, Dubonos SV, Grigorieva IV, Firsov AA. Electric field effect in atomically thin carbon films. *Science*. 2004;306:666–9.
- Sanchez VC, Jachak A, Hurt RH, Kane AB. Biological interactions of graphene-family nanomaterials: an interdisciplinary review. *Chem Res Toxicol*. 2012;25:15–34.
- Yang Y, Asiri AM, Tang Z, Du D, Lin Y. Graphene based materials for biomedical applications. *Mater Today*. 2013;16:365–73.
- Goenka S, Sant V, Sant S. Graphene-based nanomaterials for drug delivery and tissue engineering. *J Control Release*. 2014;173:75–88.
- Miao W, Shim G, Kang CM, Lee S, Choe YS, Choi HG, Oh YK. Cholesteryl hyaluronic acid-coated, reduced graphene oxide nanosheets for anti-cancer drug delivery. *Biomaterials*. 2013;34:9638–47.
- Kim H, Lee D, Kim J, Kim TI, Kim WJ. Photothermally triggered cytosolic drug delivery via endosome disruption using a functionalized reduced graphene oxide. *ACS Nano*. 2013;7:6735–46.
- Bianco A. Graphene: safe or toxic? The two faces of the medal. *Angew Chem Int Ed Engl*. 2013;52:4986–97.
- Ma Y, Shen H, Tu X, Zhang Z. Assessing in vivo toxicity of graphene materials: current methods and future outlook. *Nanomedicine (Lond)*. 2014;9:1565–80.
- Seabra AB, Paula AJ, de Lima R, Alves OL, Duran N. Nanotoxicity of graphene and graphene oxide. *Chem Res Toxicol*. 2014;27:159–68.
- de Jesus MB, Kapila YL. Cellular mechanisms in nanomaterial internalization, intracellular trafficking, and toxicity. In: Durán N, Guterres SS, Alves OL, editors. *Nanomedicine and nanotoxicology*. New York: Springer; 2014. p. 201–27.
- Nehoff H, Parayath NN, Taurin S, Greish K. In vivo evaluation of acute and chronic nanotoxicity. In: Sahu SC, Casciano DA, editors. *Handbook of nanotoxicology, nanomedicine and stem cell use in toxicology*. Chichester: Wiley; 2014.
- Mendonça MC, Soares ES, de Jesus MB, Ceragioli HJ, Ferreira MS, Catharino RR, Cruz-Höfling MA. Reduced graphene oxide induces transient blood-brain barrier opening: an in vivo study. *J Nanobiotechnol*. 2015;13:78.
- Abbott NJ, Patabendige AA, Dolman DE, Yusof SR, Begley DJ. Structure and function of the blood-brain barrier. *Neurobiol Dis*. 2010;37(1):13–25.
- Gatoo MA, Naseem S, Arfat MY, Dar AM, Qasim K, Zubair S. Physicochemical properties of nanomaterials: implication in associated toxic manifestations. *Biomed Res Int*. 2014;2014:498420.

15. Moser VC. Functional assays for neurotoxicity testing. *Toxicol Pathol.* 2011;39:36–45.
16. Zhang D, Zhang Z, Liu Y, Chu M, Yang C, Li W, Shao Y, Yue Y, Xu R. The short- and long-term effects of orally administered high-dose reduced graphene oxide nanosheets on mouse behaviors. *Biomaterials.* 2015;68:100–13.
17. Hawkins BT, Davis TP. The blood-brain barrier/neurovascular unit in health and disease. *Pharmacol Rev.* 2005;57:173–85.
18. Luissint AC, Artus C, Glacial F, Ganeshamoorthy K, Couraud PO. Tight junctions at the blood brain barrier: physiological architecture and disease-associated dysregulation. *Fluids Barriers CNS.* 2012;9:23.
19. Eng LF, Ghirnikar RS, Lee YL. Glial fibrillary acidic protein: GFAP-thirty-one years (1969–2000). *Neurochem Res.* 2000;25:1439–51.
20. Pinto AM, Gonçalves IC, Magalhães FD. Graphene-based materials biocompatibility: a review. *Colloids Surf B Biointerfaces.* 2013;111:188–202.
21. Singh SK, Singh MK, Nayak MK, Kumari S, Shrivastava S, Grácio JJ, Dash D. Thrombus inducing property of atomically thin graphene oxide sheets. *ACS Nano.* 2011;5(6):4987–96.
22. Nourshargh S, Alon R. Leukocyte migration into inflamed tissues. *Immunity.* 2014;41:694–707.
23. Kampfmann I, Bauer N, Johannes S, Moritz A. Differences in hematologic variables in rats of the same strain but different origin. *Vet Clin Pathol.* 2012;41:228–34.
24. Lindstrom NM, Moore DM, Zimmerman K, Smith SA. Hematologic assessment in pet rats, mice, hamsters, and gerbils: blood sample collection and blood cell identification. *Vet Clin North Am Exot Anim Pract.* 2015;18(1):21–32.
25. Longmire M, Choyke PL, Kobayashi H. Clearance properties of nano-sized particles and molecules as imaging agents: considerations and caveats. *Nanomedicine (Lond).* 2008;3:703–17.
26. Tarrant J, Meyer D, Katavolos P. Use of optimized aminotransferase methods in regulated preclinical studies. *Vet Clin Pathol.* 2013;42:535–8.
27. Gowda S, Desai PB, Kulkarni SS, Hull VV, Math AAK, Vernekar SN. Markers of renal function tests. *N Am J Med Sci.* 2010;2:170–3.
28. Pagana KD, Pagana TJ. *Mosby's manual of diagnostic and laboratory tests.* 4th ed. St. Louis: Mosby Elsevier; 2010.
29. Jarosz A, Skoda A, Dudek I, Szukiewicz D. Oxidative stress and mitochondrial activation as the main mechanisms underlying graphene toxicity against human cancer cells. *Oxid Med Cell Longev.* 2016. doi:10.1155/2016/5851035.
30. Yang K, Li Y, Tan X, Peng R, Liu Z. Behavior and toxicity of graphene and its functionalized derivatives in biological systems. *Small.* 2013;9(9–10):1492–503.
31. Manke A, Wang L, Rojanasakul Y. Mechanisms of nanoparticle-induced oxidative stress and toxicity. *BioMed Res Int.* 2013. doi:10.1155/2013/942916.
32. Khanna P, Ong C, Bay B, Baeg G. Nanotoxicity: an interplay of oxidative stress, inflammation and cell death. *Nanomaterials.* 2015;5:1163–80.
33. Droge W. Free radicals in the physiological control of cell function. *Physiol Rev.* 2002;82:47–95.
34. Jaworski S, Sawosz E, Kutwin M, Wierzbicki M, Hinzmann M, Grodzik M, Winnicka A, Lipińska L, Włodyga K, Chwałbóg A. In vitro and in vivo effects of graphene oxide and reduced graphene oxide on glioblastoma. *Int J Nanomedicine.* 2015;10:1585–96.
35. Kanakia S, Toussaint JD, Mullick Chowdhury S, Tembulkar T, Lee S, Jiang YP, Lin RZ, Shroyer KR, Moore W, Sitharaman B. Dose ranging, expanded acute toxicity and safety pharmacology studies for intravenously administered functionalized graphene nanoparticle formulations. *Biomaterials.* 2014;35:7022–31.
36. Moser VC. Observational batteries in neurotoxicity testing. *Int J Toxicol.* 2000;19:407–11.
37. Ohkawa H, Ohishi N, Yagi K. Assay for lipid peroxides in animal-tissues by thiobarbituric acid reaction. *Anal Biochem.* 1979;95:351–8.
38. Batista AG, Lenquiste SA, Cazarin CBB, da Silva JK, Luiz-Ferreira A, Bogusz Junior S, Hantao LW, de Souza RN, Augusto F, Prado MA, Maróstica Junior MR. Intake of jaborcaba peel attenuates oxidative stress in tissues and reduces circulating saturated lipids of rats with high-fat diet-induced obesity. *J Funct Foods.* 2014;6:450–61.
39. Johansson LH, Borg LAH. A spectrophotometric method for determination of catalase activity in small tissue samples. *Anal Biochem.* 1988;174:331–6.
40. Mammalian erythrocyte micronucleus test, In: redbook 2000: toxicological principles for the safety assessment of food ingredients. U.S. FDA. 2000. <http://www.fda.gov>. Accessed 25 Jan 2016.
41. Mendonça MC, Soares ES, Stávale LM, Irazusta SP, Cruz-Höfling MA. Upregulation of the vascular endothelial growth factor, Flt-1, in rat hippocampal neurons after envenoming by *Phoneutria nigriventer*; age-related modulation. *Toxicol.* 2012;60:656–64.

Submit your next manuscript to BioMed Central and we will help you at every step:

- We accept pre-submission inquiries
- Our selector tool helps you to find the most relevant journal
- We provide round the clock customer support
- Convenient online submission
- Thorough peer review
- Inclusion in PubMed and all major indexing services
- Maximum visibility for your research

Submit your manuscript at
www.biomedcentral.com/submit



Capítulo III - PEGylation of reduced graphene oxide induces toxicity in cells of the blood-brain barrier: an *in vitro* and *in vivo* study

Monique Culturato Padilha Mendonça^{1,2}, Edilene Siqueira Soares², Marcelo Bispo de Jesus², Helder José Ceragioli³, Ângela Giovana Batista⁴, Ádám Nyúl-Tóth⁵, Judit Molnár⁵, Imola Wilhelm⁵, Mário Roberto Maróstica Júnior⁴, István Krizbai^{5,6}, Maria Alice da Cruz-Höfling^{1,2*}

¹ Department of Pharmacology, Faculty of Medical Sciences; State University of Campinas, Campinas, SP, Brazil

² Department of Biochemistry and Tissue Biology, Institute of Biology; State University of Campinas, Campinas, SP, Brazil

³ Department of Semiconductors, Instruments and Photonics, Faculty of Electrical and Computer Engineering; State University of Campinas, Campinas, SP, Brazil

⁴ Department of Food and Nutrition, School of Food Engineering, State University of Campinas, Campinas, SP, Brazil

⁵ Institute of Biophysics, Biological Research Centre, Hungarian Academy of Sciences, Szeged, Hungary

⁶ Vasile Goldis Western University, Arad, Romania.

*Corresponding author: mo_padilha@hotmail.com; +55 (19) 3521-6250; Department of Pharmacology, Faculty of Medical Sciences, State University of Campinas, 13083-881, Campinas, SP, Brazil.

Abstract

Polyethylene glycol (PEG) is frequently used to coat and improve the pharmacokinetic behavior of nanoparticles. Studies which contribute to our understanding of the effects of PEGylation on the toxicity of nanoparticle formulation are therefore highly relevant. In the present study, reduced graphene oxide (rGO) was functionalized with PEG and its effects on key components of the blood-brain barrier, such as astrocytes and endothelial cells, were analyzed in culture and in an *in vivo* rat model. The *in vitro* studies demonstrated concentration-dependent toxicity. The highest concentration (100 µg/ml) of non-PEGylated rGO had a lower toxic influence on cell viability in primary cultures of astrocytes and rat brain endothelial cells (RBECs), while PEGylated rGO induced deleterious effects and cell death. We assessed hippocampal BBB integrity *in vivo* by evaluating astrocyte activation and the expression of the endothelial tight and adherens junctions. From 1 h to 7 days post-rGO-PEG systemic injection, a notable and

progressive down-regulation of proteins related to astrocytes (GFAP, connexin-43), the endothelial tight (occludin) and adherens (β -catenin) junctions, and basal lamina (laminin) were observed. The formation of intracellular ROS and an increase in the enzymatic antioxidant system induced by PEGylated rGO indicated oxidative stress-mediated damage. Under the experimental conditions and design of the present study the PEGylation of rGO did not improve interaction with components of the blood-brain barrier. In contrast, the attachment of PEG to rGO induced deleterious effects in comparison with the effects caused by non-PEGylated rGO.

Keywords

PEGylation; graphene-based nanomaterials; central nervous system; Nanotoxicity

Abbreviations

¹³C NMR: carbon 13 nuclear magnetic resonance; BBB: blood-brain barrier; CAT: catalase; CI: cell index; CM-H2DCFDA: 5-(6)-chloromethyl-2',7'-dichlorodihydrofluorescein diacetate, acetyl ester; CNS: central nervous system; Cx43: connexin-43; DOC: sodium deoxycholate; FTIR-ATR: Fourier-transform infrared spectroscopy in the attenuated total reflectance mode; GFAP: glial fibrillary acidic protein; GJ: gap-junction; GO: graphene oxide; HRTEM: high resolution transmission electron microscopy; MALDI-MSI: matrix-assisted laser desorption/ionization mass spectrometry imaging; PDI: polydispersity index; PEG: Polyethylene glycol; RBECs: rat brain endothelial cells; rGO: reduced graphene oxide; RO-201724: 4-(3-butoxy-4-methoxybenzyl)imidazolidin-2-one; ROS: reactive oxygen species; SEM: standard error of the mean; SOD: superoxide dismutase; TBARS: thiobarbituric acid reactive substances; TEM: transmission electron microscopy.

Introduction

Since its discovery in 2004, graphene and its derivatives, such as graphene oxide (GO) and reduced graphene oxide (rGO), have been extensively studied in many different fields. Their remarkable electronic, optical, magnetic, thermal and mechanical properties lead to the broad-spectrum application of these nanomaterials in neuroscience, biomedicine, bioimaging, biosensor development, drug/gene delivery, photothermal therapy and tissue engineering (Zhang et al. 2012; Byun 2015; John et al. 2015; Guo et al 2016).

Typically, the nanomaterial surface can be tailored through chemical modification to enhance such properties. One of the most common of these modifications is PEGylation, which is the process of the covalent and non-covalent attachment of polyethylene glycol (PEG) molecules to the surface of nanomaterials. PEG is a polymer composed of repetitive subunits of ethylene ether, available in different molecular masses, variable branched chain lengths and terminal functional groups. The attachment of PEG improves the stability and solubility of nanomaterials in physiological solutions and reduces their accumulation in the reticuloendothelial system, thus prolonging blood circulation half-life and improving pharmacokinetic behavior (Bottini et al. 2011; Jokerst et al. 2011). Conversely, some studies have identified minimal benefits and even described negative effects such as improving nanoparticle circulation half-life (Verhoef and Anchordoquy 2013), nanoparticle uptake and reductions in overall *toxicity* (Soenen et al. 2014; Moret et al. 2015).

The interplay between PEGylated graphene-based nanomaterials and the central nervous system (CNS) are poorly understood, and details about their toxicological characteristics to support the rational design and development of new nanomaterials are lacking.

We have previously demonstrated that water-suspended rGO injected in rats through the tail vein (i.v.) induces a transient disruption of the paracellular tightness of the blood-brain barrier (BBB) in the hippocampus (Mendonça et al. 2015), with a relatively low toxicity for the vital organs (Mendonça et al. 2016). The BBB is a dynamic interface that separates the peripheral circulating blood and the CNS environment. The BBB plays a major role in the maintenance of the homeostasis of the brain by regulating ion traffic, entry of xenobiotics or potentially harmful molecules, and at the same time mediates the transport of nutrients to the brain parenchyma. Formed by specialized non-fenestrated vascular endothelial cells, the BBB is tightly controlled by astrocytes, pericytes embedded in the vascular basement membrane, microglia and neurons. The neurovascular unit consists of endothelium, astrocytes, pericytes and neurons, highlighting the close interconnection between the BBB and neural functionality (Hawkins and Davis 2005; Luissint et al. 2012).

In the present study, we functionalized rGO with PEG and investigated its *in vitro* and *in vivo* effects on the BBB. By investigating the response of astrocytes and rat brain endothelial cells (RBECs) to non-PEGylated and PEGylated rGO we hope to provide a better understanding of the interactions between these graphene derivatives in living cells

and organisms. The study will also contribute to an improved characterization of the effects of PEGylation on graphene-based nanomaterials.

Material and methods

Chemicals

All chemicals used in rGO-PEG synthesis and cell culture were obtained from Sigma-Aldrich, unless stated otherwise.

rGO-PEG Synthesis and Characterization

The detailed synthesis of rGO was described previously (Mendonça et al. 2015). Here, we aimed to functionalize rGO with PEG. Briefly, an aqueous solution of PEG 6,000 (1 mg/ml) was prepared. The mixture was bath-sonicated for 15 min and the aqueous suspension of rGO (1 mg/ml) was added to the solution. After incubation under ultrasonication for 30 min at room temperature, the solution contained the rGO-PEG final product.

The PEGylation was further confirmed by Fourier-transform infrared spectroscopy in attenuated total reflectance mode (FTIR-ATR) using a FTIR Spectrophotometer (Shimadzu-8400S, Kyoto, Japan). Forty scans were taken with the resolution of 4 cm⁻¹ in the region of 4000-400 cm⁻¹. The nuclear magnetic resonance (NMR) spectra of ¹³C were recorded at room temperature under magic angle spinning with a Bruker Avance 300 spectrometer operating at 75 MHz. Dynamic light scattering (DLS) technique was used for the measurement of size, polydispersity index (PDI) and zeta potential of the rGO-PEG suspension using a ZetaSizer Nano ZS 90 instrument (Malvern Instruments Ltd., Worcestershire, UK). The results were expressed as the average of three measurements.

Morphological analysis of the sample was done with high-resolution transmission electron microscopy (HRTEM) using a JEOL JSM-6330F microscope operated at 300 kV as previously described (Mendonça et al. 2015).

Cell culture

Isolation of astrocytes and RBECs was carried out following the national and international recommendations for the care and use of laboratory animals.

Astrocytes. Astrocytes were prepared from newborn Wistar rats (*Rattus norvegicus*) by mechanical dissociation of the brain tissue and filtering through a cell strainer of 40 μm pore size. Cells were cultured until confluence on poly-L-lysine-coated dishes and frozen in Bambanker cell freezing medium (Nippon Genetics). Before use, cells were plated into poly-L-lysine-coated 96-well plates or 8-well microscopy culture chambers (for immunofluorescence assays) and cultured until confluence. Cells were used at passage number P1.

RBECs. RBECs were prepared from three-week-old Wistar rats. Under sterile conditions, brains were gently dissected, and forebrains collected in ice-cold phosphate buffered saline (PBS). The meninges were carefully removed using sterile chromatography paper, cut into small pieces and digested in two enzymatic steps: (1) collagenase type 2 and DNase I in DMEM/F12 (Life Technologies, Budapest, Hungary) at 37°C for 75 minutes, and (2) collagenase/dispase and DNase I in DMEM/F12 at 37°C for 50 minutes. Myelin was removed by centrifugation on 20% bovine serum albumin (BSA) between the two digestion steps. The digested microvessel fragments were separated on a continuous 33% Percoll gradient and plated onto fibronectin/collagen type IV-coated dishes; 96-well plates, E-plates (ACEA Biosciences, San Diego, USA) or Transwell (#3470; Corning Life Sciences, Corning, USA) permeable polyester filters (0.4 μm pore size, 0.33-cm² surface area). Cells were maintained in DMEM/F12 containing 10% plasma-derived serum (PDS, First Link, Wolverhampton, UK), 1 ng/ml basic fibroblast growth factor (Sigma Aldrich), 100 $\mu\text{g/ml}$ heparin, and 5 $\mu\text{g/ml}$ insulin-transferrin-selenite at 37°C and 5% CO₂. In the first two days, 4 $\mu\text{g/ml}$ puromycin was added to remove contaminating cells. Three days after isolation, RBECs reached confluence and were treated with 550 nM hydrocortisone, 250 μM CTP-cAMP and 17.5 μM 4-(3-butoxy-4-methoxybenzyl)imidazolidin-2-one (RO-201724) to induce BBB characteristics (Wilhelm et al. 2011).

Toxicity measurements

The *in vitro* concentration of rGO-PEG (100 $\mu\text{g/ml}$) was selected as a function of the concentration already used for *in vivo* experiments (7 mg/kg) (Mendonça et al. 2015, 2016). For the calculation, we considered a 200 g rat with blood volume average of 14 ml (Lindstrom et al. 2015). We also used a concentration 10 times lower than the threshold concentration, able to induce oxidative stress and DNA damage in some cell lines (Guo and Mei 2014).

EZ4U assay. Cell viability was detected using EZ4U assay (Biomedica Medizinprodukte, Vienna, Austria). Cells were seeded in 96-well coated plate (Corning Technologies, Corning, NY, USA) and after reaching confluence the cells were treated with culture medium (negative control), rGO-PEG or vehicle (PEG 6,000) for 3 h 30 min (RBECs) or 24 h (Astrocytes). For the sake of comparison, we also treated the cells with an aqueous suspension of rGO and its vehicle (sterile distilled water) using the same concentrations as for other treatments. After washing the cells with phenol-red free DMEM, the EZ4U assay was performed according to the manufacturer's instructions. The method is based on the reduction of tetrazolium salt to colored formazan by the mitochondria of living cells. The absorbance was recorded using a microplate reader (FLUOstar Optima; BMG Labtechnologies, Offenburg, Germany) at 492 nm and values were compared to control cells. To confirm that rGO-PEG was not able to spontaneously metabolize the EZ4U substrate, we also measured the response of rGO-PEG in the absence of cells. rGO-PEG alone was not able to reduce uncolored tetrazolium salts into intensely colored formazan derivate.

Cell impedance measurements. Cell impedance was detected using the xCELLigence system (ACEA, San Diego, CA, USA). It is a cell-based label-free method that measures in real time electrical impedance across gold electrodes placed at the bottom of a 96-well plate (E-plate 96, ACEA Biosciences). Further, the xCELLigence software (version 1.2.1) converts the electrical impedance to a cell index (CI) value (arbitrary units). In general, under the same physiologic conditions, if more cells are attached to the electrodes, the impedance value is higher, leading to increased CI. Contrarily, in the absence of cells, i.e., cell death or toxicity-induced cell detachment; a lower CI value is obtained. The impedance depends on the tightness of the junctions as well.

Cells were seeded in E-plates and the impedance was continuously monitored until cells reached a steady phase (confluence and well-formed tight junctions in the case of RBECs), when they were treated with rGO or rGO-PEG. Impedance was monitored every 1 h during 24 h.

Immunofluorescence (IF)

Cells were fixed in 95% ethanol/5% acetic acid at -20°C for 5 minutes. After blocking with 3% BSA- for 30 min, samples were incubated overnight with primary antibodies (Table 1). The staining was visualized using Alexa 594- (GFAP), Alexa 488-

(Aquaporin-4, Occludin) or Cy5-conjugated (Claudin-5) secondary antibodies. Nuclear staining of the cells was carried out using Hoechst 33342. Images were recorded by a Nikon Eclipse TE2000U photomicroscope with epifluorescent capabilities connected to a digital camera (Spot RT KE).

Table 1. Primary antibodies used in this study.

Antibody	Dilution	Supplier	Reference	Application
Aquaporin-4	1:100	Santa Cruz	Sc-20812	IF
β -catenin	1:500	Santa Cruz	sc-7963	WB
Catalase (CAT)	1:400	Santa Cruz	sc-271242	WB
Claudin-5	1:100	Invitrogen	35-2500	IF
Connexin-43 (Cx43)	1:500	Santa Cruz	sc-9059	WB
GFAP	1:500	Dako	Z0334	WB
GFAP	1:10000	Sigma Aldrich	G3893	IF
Laminin	1:500	Sigma Aldrich	L9393	WB
Occludin	1:500	Santa Cruz	sc-5562	WB
Occludin	1:100	Invitrogen	71-1500	IF
Superoxide dismutase-1 (SOD-1)	1:500	Santa Cruz	sc-11407	WB
β -actin	1:1000	Sigma Aldrich	A2228	WB

ROS measurements

Cells were treated in 96-well plates for 3h 30 min (RBECs) and 24 h (Astrocytes), washed with Ringer-HEPES and incubated for 1 h in Ringer-HEPES containing 2 μ M CM-H₂DCFDA (Molecular Probes/Thermo Fisher Scientific) and 25 μ g/ml Pluronic F-. CM-H₂DCFDA passively diffuses into cells, where it is modified by intracellular esterases and thiols while subsequent oxidation results in a fluorescent product. Fluorescence was monitored using a FLUOstar Optima microplate reader equipped with a 492/520 nm excitation/emission filter set.

Animal care and rGO-PEG systemic administration

All *in vivo* experiments were carried out at State University of Campinas and approved by the institutional Committee for Ethics in Animal Use (protocol no. 2884-1) and followed the Brazilian Society of Laboratory Animal Science guidelines. Male Wistar rats (*Rattus norvegicus*, 6 week-old, 180 \pm 40 g) received a single i.v. injection of rGO-PEG (7 mg/kg; concentration 1 mg/ml) (Mendonça et al. 2015, 2016), while the control group was given the same volume of vehicle (PEG 6,000). For the sake of comparison, we

treated the cells with an aqueous suspension of rGO and its vehicle, using the same concentrations.

All animals were euthanized by carbon dioxide (CO₂) or anesthetics overdose (3:1 mixture of ketamine chloride (Dopalen[®], 100 mg/kg body weight,) and xylazine chloride (Anasedan[®], 10 mg/kg body weight, Fortvale, Valinhos, SP, Brazil) 15 min, 1 h, 3 h and 7 days after the i.v. administration of rGO-PEG. Animals of the control group were euthanized 1 h later. A single control group was used as preliminary experiments showed no time difference relative to data.

Western blotting

Western blotting was performed in hippocampal homogenates (n = 5 for each time, including single control) as previously described [10]. Briefly, after being blocked with 5% (v/v) skimmed milk in TBS-T (0.1 % Tris-buffered saline with 0.05 % Tween 20, pH 7.4) for 1 h at room temperature; the membranes were incubated at 4°C overnight with primary antibody (Table 1). After washing with TBS-T, the membranes were incubated for 2 h at room temperature with the respective HRP-labeled secondary antibody (1:1000). Immunoreactive bands were visualized using a chemiluminescence kit (Super Signal West Pico Chemiluminescent Substrate; Pierce Biotechnology, Rockford, IL, USA) and recorded with a G:BoxiChemi camera (Syngene, Cambridge, UK). The blots were subsequently stripped and probed with anti-β-actin to monitor protein loading, the efficiency of blot transfer, and nonspecific changes in protein levels. Bands intensities were quantified using ImageJ 1.45s software (NIH, Bethesda, MD, USA).

Evaluation of oxidative stress parameters

The blood samples were collected via cardiac puncture in serum separator gel tube (n = 3-5 for each time, including single control). The enzyme antioxidant systems (SOD and CAT) in the serum samples were measured using colorimetric methods. The SOD activity in serum was obtained after reaction with hypoxanthine, nitroblue tetrazolium and 0.07 U of xanthine oxidase as described in detail before (Batista et al. 2014). The CAT activity method was carried out based on the reaction of the enzyme with methanol and H₂O₂. Purpald (4-amino-3-hydrazino-5-mercapto-1,2,4-triazole) was used as chromogen and the resultant formaldehyde products were measured at 540 nm (adapted from Johansson and Borg (1988)).

Lipid peroxidation was determined by measuring TBARS using a spectrophotometric method described by Ohkawa et al. (1979) and adapted by Batista et al. (2014) in which malondialdehyde and the final products of lipid peroxidation react with thiobarbituric acid, forming a pink-colored complex.

Statistical analysis

All data are expressed as mean \pm SEM. Statistically significant differences were assessed by Student's t test or One-way ANOVA followed by Tukey multiple comparison post-hoc test with a p-value < 0.05 considered significant. Graphs were prepared with Prism software, version 5 (GraphPad Inc., La Jolla, CA, USA) and all of the data are expressed as mean \pm SEM.

Results and Discussion

Preparation and characterization of PEGylated rGO

Table 2 summarizes the main physicochemical characteristics of the non-PEGylated and PEGylated rGO measured by DLS.

Table 2. Physicochemical characteristics of non-PEGylated and PEGylated rGO.

Samples	Size (nm)	Zeta potential (mV)	PDI
Non-PEGylated rGO	342 \pm 23.5	-25 \pm 0.18	0.56 \pm 0.03
PEGylated rGO	910 \pm 32.7	-4.2 \pm 3.8	0.39 \pm 0.04

A comparison of zeta potential revealed that the charge associated with the non-PEG rGO had a greater negative zeta potential (-25 ± 0.18 mV) than the PEGylated rGO (-4.2 ± 3.8 mV). This suggests the existence of positive amino-ended branches, resulting in a lesser negative electrostatic charge for PEGylated rGO than rGO (Vila et al. 2012). The PEGylation of rGO leads to a decrease in PDI values (0.56 ± 0.03 to 0.39 ± 0.04), resulting in the diminished polydispersity of particles, probably due to a lower susceptibility to aggregate formation.

A significant increase in size, from 342 ± 23.5 nm up to 910 ± 32.7 nm, was found after PEGylation. Although this increase offers evidence for the PEGylation of nanoparticles, confirmation of the attachment of PEG to rGO is essential. For this purpose, FTIR-ATR and ^{13}C NMR were carried out. As shown in Fig. 1A, the PEGylated

rGO spectrum exhibited characteristic bands at 1080 cm^{-1} (-C-O-C stretching), 1641 cm^{-1} (C=O stretching) and 3359 cm^{-1} (O-H stretching), indicating cross-linking between PEG and rGO (Gupta et al. 2016). The ^{13}C NMR spectrum of rGO-PEG exhibited a peak at 70 ppm corresponding to $-\text{O}-\text{CH}_2$ of PEG. All ethylene glycol carbons have approximately the same microenvironment, and are thus expected to have similar chemical shift values at around 70 ppm (Zinkevich et al. 2016).

The morphology and structure of rGO-PEG analyzed by transmission electron microscopy and high-resolution transmission electron microscopy also showed wrinkles, lateral corrugations and a scrolled appearance of rGO-PEG (Fig. 1C, D). The surface morphology and structural parameters of non-PEGylated rGO have been previously demonstrated (Mendonça et al. 2015, 2016).

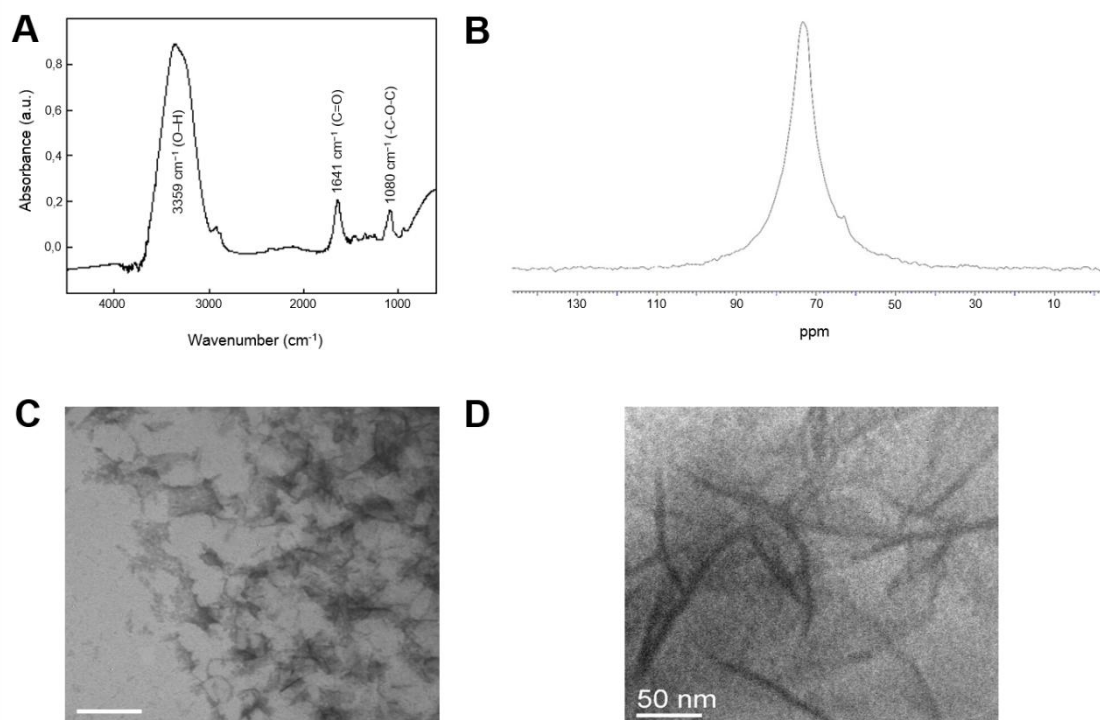


Fig. 1 rGO-PEG characterization. (A) Fourier-transform infrared spectroscopy in the attenuated total reflectance mode (FTIR-ATR); (B) ^{13}C NMR spectra of rGO-PEG; (C) TEM and (D) HRTEM images of rGO-PEG. A.u = Arbitrary units.

PEGylation of rGO increased its toxicity in astrocytes and RBECs

We began by investigating the effects of rGO-PEG exposure on the viability of primary rat astrocytes and RBECs using EZ4U assay and the xCELLigence system. This system measures electrical impedance across the cell monolayer using a high-density electrode array that coats the bottom of the well, and converts the impedance values to a

Cell Index. These cell index values directly correspond to the change in the status of a cell, such as its viability (Ke et al. 2011).

The viability of astrocytes was assessed after exposure to culture medium for 24 h (negative control), rGO-PEG or vehicle (PEG), at concentrations of 10 $\mu\text{g/ml}$ and 100 $\mu\text{g/ml}$. For the sake of comparison, we treated the cells with an aqueous suspension of rGO and its vehicle, using the same concentrations as the other treatments.

As shown in Figure 2, both vehicles (sterile distilled water and PEG) had no toxic effect on astrocytes, whereas PEG (100 $\mu\text{g/ml}$) induced a significant increase in cell viability compared to all the other groups ($p < 0.001$). No substantial differences were observed between controls and cells treated with non-PEGylated rGO. Surprisingly, the viability of astrocytes decreased from 126% to 16% ($p < 0.001$) when the astrocytes were treated with 100 $\mu\text{g/ml}$ of rGO-PEG (Fig. 2A).

Similar dose-dependent toxic effects of rGO, dispersed with PEG, Pluronic P123 or sodium deoxycholate (DOC), were reported by Wojtoniszak et al. (2012). These studies were carried out using L929 mouse fibroblasts and rGO concentrations ranging from 3.125 to 100 $\mu\text{g/ml}$. The authors found that rGO-PEG exhibited the greatest biocompatibility with respect to Pluronic P123 and DOC. Cells exposed to the suspension of rGO-PEG at concentrations between 3.125 $\mu\text{g/mL}$ and 25 $\mu\text{g/mL}$ displayed relatively high viability; however, when the concentration exceeded 25 $\mu\text{g/mL}$, viability was abruptly reduced.

In another work, Vila et al. (2012) conducted a comparative study of how the number of branches of the PEG molecule affects the cellular uptake and cytotoxicity of GO. The cellular uptake of linear PEGylated GO (sized 95 nm) was significantly higher than that of branched PEGylated GO (sized 190 nm) in osteoblasts, fibroblasts and macrophages. Moreover, branched PEG (75 $\mu\text{g/mL}$) induced more changes in cellular function than its linear counterpart.

All experiments using xCELLigence were performed using only the highest concentration (100 $\mu\text{g/ml}$) of rGO and rGO-PEG, which was responsible for the reduction in astrocyte viability. The xCELLigence system with real-time technology allows us to dynamically observe the decrease of the cell index curve.

Very similar toxicity patterns were observed for the PEGylated rGO-treated cells using both techniques. Although alterations in the viability of astrocytes treated with non-PEGylated rGO were not found using EZ4U assay (Fig. 2A), the cell index of rGO-

treated cells was lower than the control vehicle (Fig. 2B). This may be the result of minor morphological changes in the cells affecting the cell index (Khoet al. 2015).

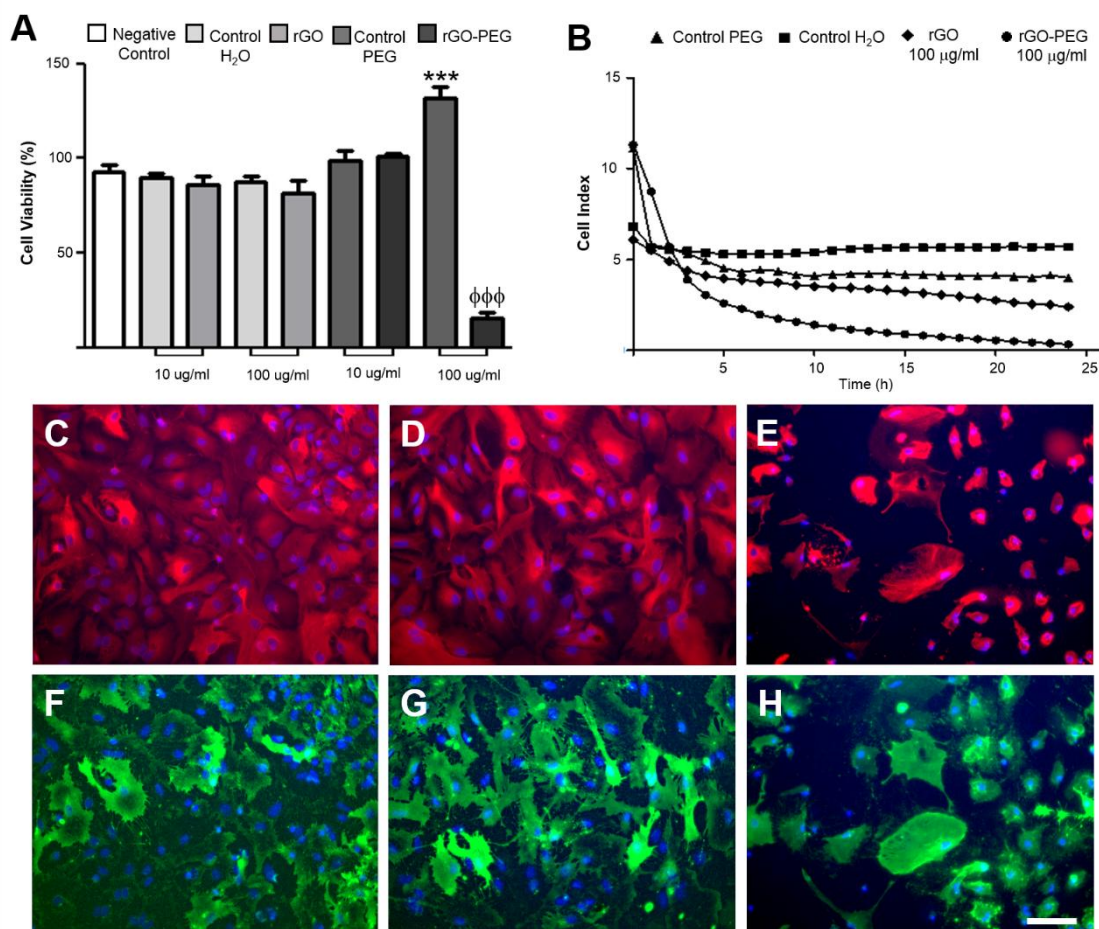


Fig. 2 Effect of rGO and rGO-PEG treatment on cultures of rat astrocytes. Astrocytes were incubated with different concentrations (10 µg/ml and 100 µg/ml) of (A) rGO and rGO-PEG during 24 h. Culture medium was used as negative control. The rGO vehicle (sterile distilled water) and rGO-PEG vehicle (PEG) were used as controls. The viability of the cells was measured using EZ4U assay 24 h after rGO or rGO-PEG treatment. The percentage is given in relation to control medium and the columns are the mean ± SEM (n=4). (B) Analysis of cell viability using xCELLigence system. The curves represent the average of four individual well ± SEM of a representative experiment. (C-H) Representative immunofluorescence images for glial fibrillary acidic protein (GFAP) (red) and Aquaporin-4 (green) after (C) sterile distilled water, (F) PEG, (D, G) rGO 100 µg/ml, and (E, H) rGO-PEG 100 µg/ml treatment. Nuclei were stained with Hoechst (blue). ***p<0.001 vs. all other groups; φφφp<0.001 vs. all other groups (One-way ANOVA plus Tukey post-comparison test). Bar: 100 µm.

Immunostaining of the astrocytic markers GFAP and Aquaporin-4 was used to analyze morphological alterations in the astrocytes exposed for 24 h to non-PEGylated and PEGylated-rGO. Immunostaining resulted in clear immunoreactivity for both

proteins, with an almost total overlap. When compared to the control cells (Fig. 2C, F), both rGO and rGO-PEG produced morphological changes in the rat astrocytes. Astrocytes treated with rGO presented moderate body and process retraction (Fig. 2D, G), while astrocytes treated with rGO-PEG exhibited a complete absence of normal cell structure, the loss of cell-to-cell contact, and a noticeable reduction in the number of astrocytes (Fig. 2E, H).

The cultured astrocytes presented atrophy and cell death after 24 h of exposure to PEGylated rGO. It is well known that CNS injury activates astrocytes in a process known as reactive gliosis or astrogliosis, which is manifested through astrocyte hyperplasia or hypertrophy of cell processes caused by variable up-regulation of cytoskeletal-forming GFAP (Sofroniew and Vinters 2010). However, Zhao et al. (2003) have reported that damage to or death of astrocytes can occur in the early periods after brain injury, with concomitant down-regulation of GFAP immunoreactivity, which can be followed in later periods by reactive GFAP upregulation and the formation of glia scars to protect the injured region of the brain.

As rGO-PEG displayed cytotoxic effects on astrocytes, we subsequently assessed the impact of rGO-PEG upon RBECs with BBB phenotype. After 24 h of incubation with supplements which enhanced the BBB phenotype, once the growth of the RBECs reached a steady plateau, we began treatment with nanomaterials. As the brain endothelial cells are more sensitive to injury than astrocytes, the viability of the RBECs was assessed after exposure to treatments for 3 h 30 min.

As with the astrocytes, no substantial differences were observed in cells treated with non-PEGylated rGO. The 10 $\mu\text{g/ml}$ and 100 $\mu\text{g/ml}$ PEG groups had significantly higher levels than all the other groups ($p < 0.001$). Cell viability also decreased in RBECs incubated with 100 $\mu\text{g/ml}$ of rGO-PEG ($p < 0.001$) (Fig. 3A).

Cell index values were monitored continuously for 24 h. While rGO induced a slight decrease in the cell index, rGO-PEG treatment led to a rapid reduction within 5 h. This drop was much more pronounced than that seen in astrocytes in response to similar treatment. This suggests that astrocytes are more resistant to toxic insult than endothelial cells. This finding is in line with earlier results showing that cerebral endothelial cells had a higher susceptibility to oxidative stress than astrocytes (Bresgen et al. 2006). PEG alone did not affect the cell index during long-term treatment (Fig. 3A), indicating that the polymer has no damaging effects on RBECs. In some cases, PEG can even enhance the properties of the endothelial barrier (Chiang et al. 2009).

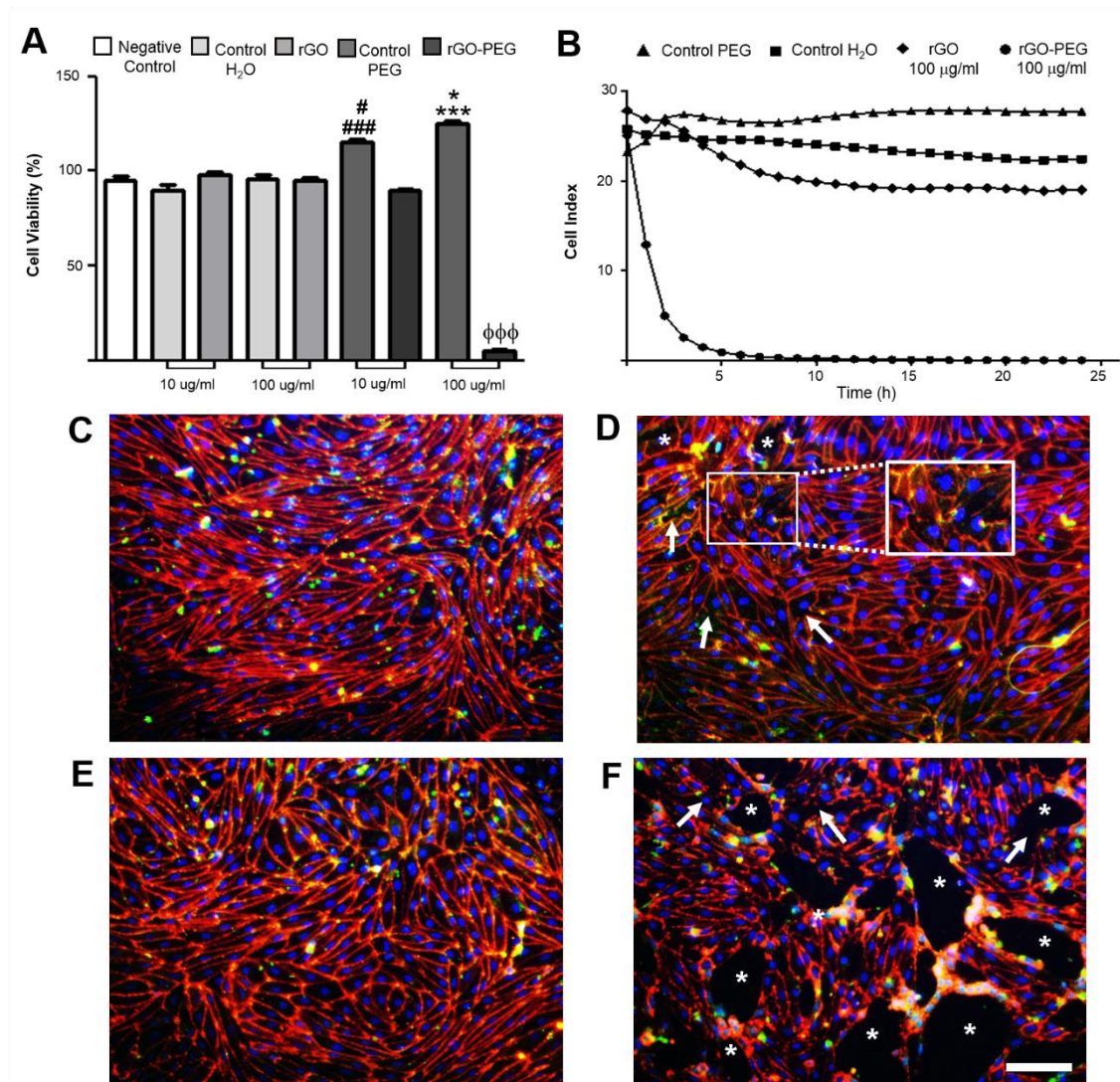


Fig. 3 Effects of rGO and rGO-PEG treatment on RBECs. Analysis of cell viability using (A) EZ4U assay and (B) xCELLigence system. Culture medium was used as negative control. The rGO vehicle (sterile distilled water) and rGO-PEG vehicle (PEG) were used as blank controls. The viability of the cells was measured using EZ4U assay 3 h 30 min after rGO or rGO-PEG treatment. The percentage is given in relation to control medium and the columns are the mean \pm SEM ($n=5$). (B) Analysis of cell viability using xCELLigence system. The curves represent the average of four individual well \pm SEM of a representative experiment. (C-F) Double immunostaining for claudin-5 (red) and occludin (green) performed 5 h after treatment with 100 $\mu\text{g/ml}$ of (C) sterile distilled water, (D) rGO, (E) PEG and (F) rGO-PEG. Nuclei were stained with Hoechst (blue). Asterisks show holes formed between endothelial cells. Arrows indicate fragmentation and loss of junctional immunostaining. # $p<0.05$ vs. control PEG 100 $\mu\text{g/ml}$; ### $p<0.001$ vs. all other groups; * $p<0.05$ vs. control PEG 10 $\mu\text{g/ml}$; *** $p<0.001$ vs. all other groups; φφφ $p<0.001$ vs. all other groups (One-way ANOVA plus Tukey post-comparison test). Bar: 100 μm .

Immunofluorescent studies using antibodies directed against junctional proteins shed light on the molecular background of decreased functionality of the cerebral

endothelium in response to rGO-PEG treatment. Under control conditions, fine, continuous membrane staining was observed (Fig. 3C, E). However, the expression patterns of the TJ proteins were significantly altered in the rGO- and rGO-PEG-treated groups. The rGO group showed irregular and discontinuous expression of occludin and claudin 5 (Fig. 3D, inset), while rGO-PEG induced widespread disruption of the RBEC monolayer, which is indicative of cell-cell junction damage (Fig. 3F).

Occludin and claudins are transmembrane proteins of the tight junctions, and control paracellular permeability. In cerebral endothelial cells claudin-5 plays a more important role, with a lack of this protein leading to the opening of the BBB for substances with a molecular weight of less than 800 Da (Nitta et al. 2003). Our results indicate that rGO-PEG has a barrier damaging effect when used in high concentrations.

rGO-PEG induced BBB breakdown and in vivo astrocyte dysfunction

While *in vitro* models are practical and cost-effective methods for screening the toxicity of potential drug carriers, they cannot completely replace the complexity of animal and human responses. Therefore, the following step was carried out to investigate the *in vivo* effects of rGO-PEG.

We had previously detected the presence of rGO inside the thalamus and hippocampus by matrix-assisted laser desorption/ionization (MALDI) mass spectrometry imaging (MSI). We also found that intravenous (i.v.) injection of rGO induced a transient blood-brain barrier opening in the hippocampus. We found downregulation of junctional proteins (the tight junction protein occluding and the adherens junction protein β -catenin) and laminin. When taken together, these are co-responsible for maintaining the paracellular tightness of the BBB (Mendonça et al. 2015). In the present study, we used the same rat model and experimental design to evaluate the expression of these three BBB-associated proteins in the rat hippocampus after rGO-PEG i.v. administration.

The rGO-PEG caused a significant decrease in occludin (32%, $p < 0.01$), β -catenin (85%, $p < 0.001$) and laminin (134%, $p < 0.01$) levels 3 h after administration. This did not increase thereafter; instead, by day 7, the proteins had reached their highest level of down-regulation ($p < 0.001$) (Fig. 4).

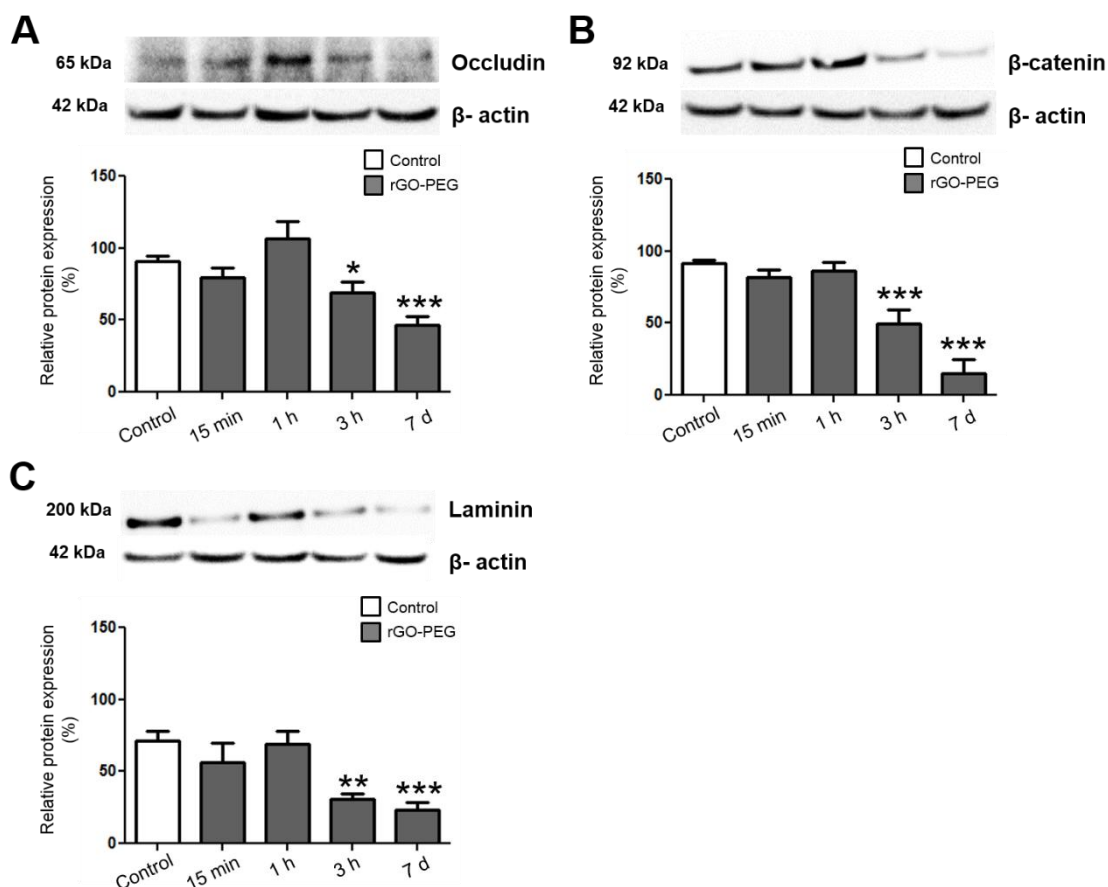


Fig. 4 Expression of proteins associated with BBB in the hippocampus as assessed by western blotting. The panels show the expression of (A) occludin, (B) β -catenin and (C) laminin at different intervals after rGO-PEG administration (7 mg/kg, i.v.). Immunoreactive bands were quantified densitometrically and normalized to an internal standard (β -actin). The results were shown as percentage of control (100%), and represent mean \pm SEM ($n = 5$ rats/interval). * $p < 0.05$, ** $p < 0.01$ and *** $p < 0.001$ compared to the control (Student's t-test).

The significant and long-lasting downregulation of BBB-associated proteins induced by PEGylated rGO implies impaired BBB function and probably a homeostatic disturbance of the hippocampal milieu. In contrast, non-PEGylated rGO induced a transient and slighter down-regulation of BBB-associated proteins which was resolved seven days post-rGO exposure (Mendonça et al. 2015), an indication that rGO is more qualified than GO-PEG in terms of being explored in the field of neuroscience research.

Analysis of hippocampal homogenates from non-PEGylated rGO-treated rats did not show significant changes in the levels of GFAP (Fig. 5A) and Cx43 (Fig. 5B). Unexpectedly, the stimulus generated by rGO-PEG did not increase the expression of GFAP, either acutely or in late periods following administration. Instead, it induced a decrease in the expression of GFAP at 3 h (47%, $p < 0.05$) and 7 days (95%, $p < 0.001$) post-

rGO-PEG injection (Fig. 5A), in comparison with the control vehicle. An explanation for this data is given by the findings obtained for *in vitro*-cultured astrocytes, which unarguably demonstrated a significant decrease in astrocyte viability through EZ4U assay and xCELLigence. Therefore, we can state that the decrease of GFAP expression in the hippocampus of rats i.v. injected with rGO-PEG, but not with non-PEGylated rGO, was due to the death of a number of astrocytes.

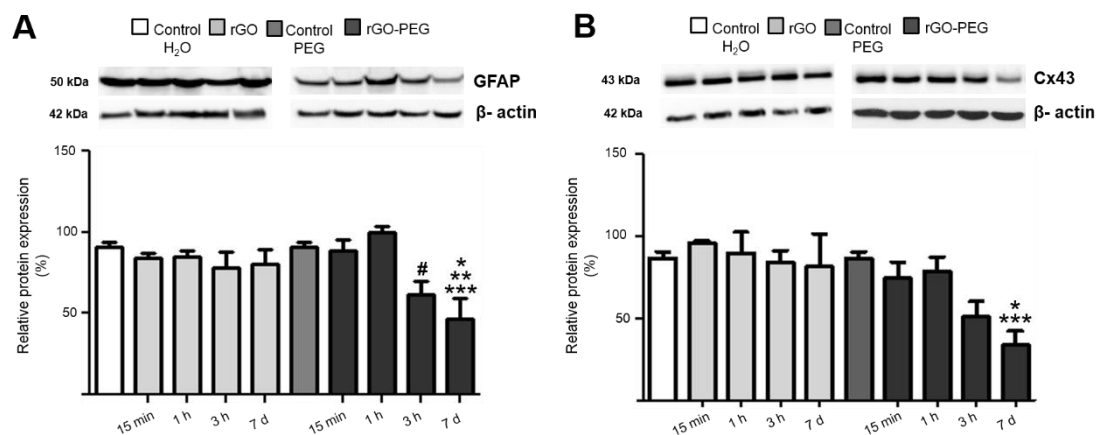


Fig. 5 Expression of astrocytic markers assessed by western blotting in hippocampal homogenate. Expression of (A) GFAP and (B) Cx43 at different intervals after rGO and rGO-PEG (7 mg/kg, i.v.) administration. Immunoreactive bands were quantified densitometrically and normalized to an internal standard (β -actin). The results were shown as percentage of control (100%), and represent mean \pm SEM (n = 5 rats/interval). A = # $p < 0.05$ vs. control H₂O, control PEG, rGO-PEG 1h; * $p < 0.05$ vs. rGO 3 h, 7d; ** $p < 0.01$ vs. rGO 15 min, 1 h, rGO-PEG 15 min; *** $p < 0.001$ vs. control H₂O, control PEG, rGO-PEG 1 h. B = * $p < 0.05$ vs. rGO 15 min, 3 h, 7 d, rGO-PEG 1 h; *** $p < 0.001$ vs. control H₂O, rGO 1 h, control PEG (One-way ANOVA plus Tukey post-comparison test).

Similarly to GFAP, the i.v. injection of rGO-PEG led to a reduction in Cx43 expression at 3 h and 7 days (159%, $p < 0.001$) (Fig. 5B) when compared to the control vehicle. These findings offer a plausible hypothesis that the strong retraction of the astrocyte processes and a loss of viability (seen in *in vitro* preparations) most likely eliminated homotypic contacts among the astrocyte processes, and even heterotypic contacts among astrocytes and endothelial cells and/or neuronal cells, also *in vivo*. Therefore, we suggest that the long-lasting and progressive decrease of Cx43 from 3 h to 7 days following the systemic administration of rGO-PEG, but not after the administration of non-PEGylated rGO, impaired the exchange of information among astrocytes due to non-operant GJs.

Astrocytes are key regulators of BBB integrity and have an impressive capacity to modulate CNS homeostasis (Verkhatsky and Nedergaard 2014). Typically, under stimuli, the astrocytes react by proliferation or the hypertrophy of cytoplasmic processes and increased expression of the intermediate filament protein GFAP from astrocyte cytoskeleton. They are also able to increase or decrease the expression of the gap-junction (GJ) protein connexin-43 (Cx43) depending on the stimulus, thus regulating the exchange of information between cells. Changes in the expression of Cx43 and the exchange of information among astrocytes are relevant to many brain lesions and pathologies (Rouachet al. 2002), as they can result in the dissemination of the pathological state and/or the accumulation of toxicants in the absence of functional GJ channels (Wallraff et al. 2006).

A recent study reported that the lack of Cx43 expression or the blockade of Cx43 channels results in increased reactive oxygen species (ROS)-induced astrocytic death (Leet al. 2014), one of the several mechanisms leading to nanotoxicity (de Jesus and Kapila 2014).

PEGylation of rGO increased ROS generation

To further widen our understanding of the mechanisms triggering toxicity we investigated if rGO-PEG treatment affects ROS generation (*in vitro*) and the antioxidant enzymatic system (*in vivo*) in comparison with the effect of non-PEGylated rGO.

Measurement of ROS formation was performed using an oxidant-sensitive fluorogenic probe CM-H2DCFDA (5-(6)-chloromethyl-2',7'-dichlorodihydrofluorescein diacetate, acetyl ester). An increase in CM-H2DCFDA fluorescence reflects an increase in ROS levels (Karlsson et al. 2010).

Following a 24 h exposure of astrocytes to nanomaterials, intracellular ROS levels significantly increased in both PEGylated and non-PEGylated rGO-treated cells (Fig. 6A). The highest concentration of rGO-PEG induced a 270% increase in the intracellular levels of ROS ($p < 0.001$), while rGO induced a 33% increase ($p < 0.001$), in comparison with their respective vehicle controls.

The non-PEGylated rGO did not induce ROS production in RBECs, but as with the astrocytes response, the highest concentration (100 $\mu\text{g/ml}$) of rGO-PEG enhanced the generation of ROS ($p < 0.001$) in RBECs, in comparison with all other groups (Fig. 6B).

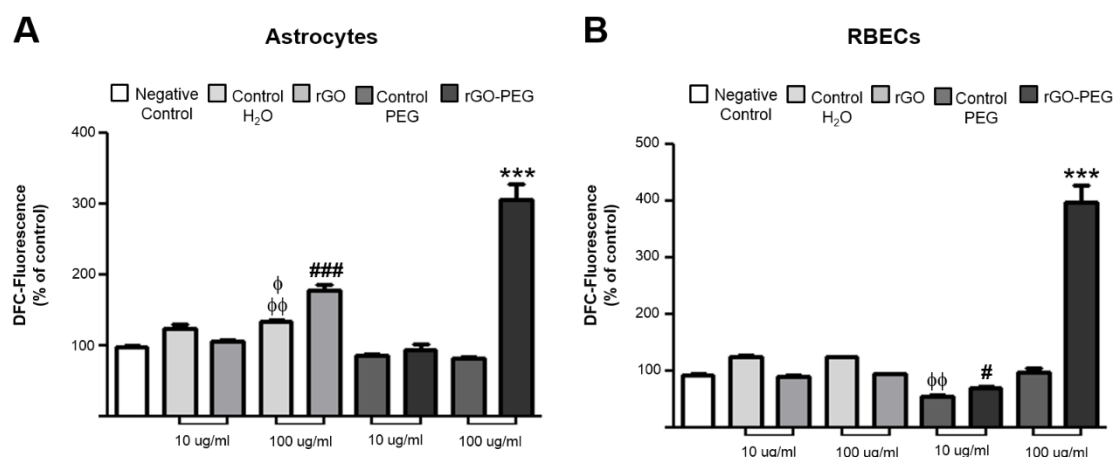


Fig. 6 ROS levels in astrocytes and RBECs incubated with rGO and rGO-PEG. Intracellular ROS levels were detected with CM-H₂-DCFDA in (A) astrocytes and (B) RBECs after 24 h and 3 h and 30 min, respectively. The bars show the quantitative analysis of fluorescent intensity from four experiments. Data represent the mean \pm SEM. A = ϕ p<0.05 vs. control PEG 10 μ g/ml; $\phi\phi$ p<0.01 vs. control PEG 100 μ g/ml; ###p<0.001 vs. control PEG 10 μ g/ml, rGO-PEG 10 μ g/ml, control PEG 100 μ g/ml; ***p<0.001 vs. all other groups. B = $\phi\phi$ p<0.01 vs. control H₂O 10 μ g/ml, 100 μ g/ml, #p<0.05 vs. control H₂O 10 μ g/ml, 100 μ g/ml; ***p<0.001 vs. all other groups (One-way ANOVA plus Tukey post-comparison test).

This data supports our hypothesis that oxidative stress is a major factor in the toxicity of rGO-PEG. The induction of ROS generation seems to be a general cellular response to rGO-PEG. Reshma et al. (2015) described the production of ROS in A549 cells after treatment with PEGylated rGO and non-PEGylated rGO. Their results reveal that PEGylated rGO were able to induce prominent ROS production at all time-points (0.5, 2, 4, 5 and 24 h) and at concentrations ranging from 5 to 100 μ g/ml. The authors found that rGO failed to generate ROS at up to 4 h as the concentration of the particle increased from 5 to 100 μ g/ml. However, ROS generation increased after 6 h of exposure with 50 μ g/ml and after 6 and 24 h of exposure with 100 μ g/ml. The findings show that the formation of ROS depends of variables such as time of exposure and the concentration of the nanoparticle, which may suggest that antioxidant activity is likely to depend on the same variables.

The detoxification of excess ROS is mediated by an efficient antioxidant system comprising non-enzymatic molecules and antioxidant enzymes (Liou and Storz2010), the most efficient of which are enzymatic antioxidants glutathione peroxidase, catalase and superoxide dismutase (SOD) (Rahman2007).

We initiated our *in vivo* analysis by evaluating the protein expression of catalase and SOD-1 in the hippocampus. As shown in Figure 7, the expression of catalase was

27% higher at 3 h ($p<0.01$) and 18% higher at 7 days ($p<0.05$) post-rGO-PEG administration, in comparison with control levels. Interestingly, only a 12% increase was detected in SOD-1 expression by day 7 (Fig. 7B).

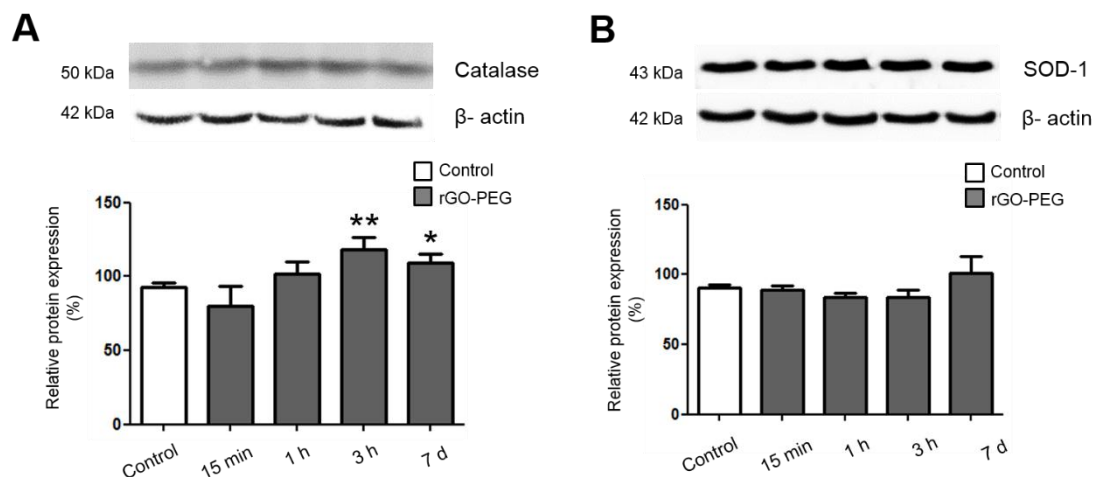


Fig. 7 Effects of rGO-PEG administration in antioxidant enzymes. (A) Densitometric analysis of (A) catalase and (B) SOD-1 performed after normalization with β -actin. The results were expressed as percentage of control (100%) and columns represent the mean \pm SEM ($n=5$ rats/interval). * $p<0.05$, ** $p<0.01$ and *** $p<0.001$ compared to the control (Student's t test).

To determine whether the protein levels of catalase and SOD-1 in hippocampus paralleled the activity level of the enzymes, we measured total SODs and catalase activities from serum samples. Over time, increases in the antioxidant enzymes and in lipid peroxidation measured by thiobarbituric acid reactive substances (TBARS) were observed (Table 3).

SOD catalyzes the conversion of superoxide anions to oxygen and hydrogen peroxide. Thus, CAT converts hydrogen peroxide to water and oxygen and completes the detoxification initiated by SOD (Rahman2007). It has been found that cells can tolerate moderate oxidative stress by up-regulating their reductive defense systems and restoring the oxidant/antioxidant balance (Halliwell 2015). Taken together, these results indicate that the increase in catalase and SOD activity/expression could be due to oxidative stress generation and may suggest a possible adaptive mechanism against insults caused by rGO-PEG administration.

Table 3. Serum levels of SOD, catalase and TBARS after rGO-PEG treatment.

	Unit	Control	rGO-PEG 15 min	rGO-PEG 1 h	rGO-PEG 3 h	rGO-PEG 7 d
CAT	nmol/min/ml	64 ± 14.6	71 ± 12.8	88 ± 19.8	89 ± 9.4	123 ± 18.3*
SOD	U/ml	35 ± 2.2	56 ± 7.8	43 ± 0.5*	49 ± 2.4**	49 ± 3.9*
TBARS	nmol/ml	3.0 ± 0.8	2.9 ± 0.7	3.4 ± 0.5	3.5 ± 0.2	4.4 ± 0.7

SOD: superoxide dismutase; CAT: catalase; TBARS: Thiobarbituric acid reactive substances. Values are mean \pm SEM of 3-4 animals in each group. * $p < 0.05$ and ** $p < 0.01$ compared to control (Student's t test).

Conclusions

The PEGylation of nanomaterials and therapeutics is currently considered to be one of the most promising approaches to reducing toxicity and obtaining favorable pharmacokinetic results. However, deleterious effects and death have been observed in different cell types treated with PEGylated nanoparticles, mostly through the induction of oxidative stress, which corroborated the results of the present experimental design.

Herein, the combined *in vitro* and *in vivo* toxicity profiles of PEGylated rGO have been investigated and reported for the first time. The data of the present study suggests the dose- and time-dependent toxicity of PEGylated rGO for key components of the blood-brain barrier, such as astrocytes and endothelial cells. In terms of toxicity mechanisms, the formation of intracellular ROS and the increase in the enzymatic antioxidant system induced by PEGylated-rGO suggest oxidative stress-mediated damage.

Conflict of interest

The manuscript does not contain clinical studies or patient data. The authors declare they have no conflict of interest.

Acknowledgements

This work is supported by the Brazilian funding agencies, Fundação de Amparo à Pesquisa do Estado de São Paulo (FAPESP) (MCPM's doctorat studentships nos. 2012/24782-5 and 2015/03254-9), Conselho Nacional de Desenvolvimento Científico e Tecnológico (CNPq) (grant no. 305099/2011-6) and Coordenação de Aperfeiçoamento de Pessoal de Nível Superior (CAPES). We dedicate this study to Professor Vitor Baranauskas (Brazilian Academy of Sciences, *in memoriam*) by his contribution to science in the last years.

References

- Batista AG, Lenquiste SA, Cazarin CBB, da Silva JK, Luiz-Ferreira A, Bogusz Junior S, Hantao LW, de Souza RN, Augusto F, Prado MA, Maróstica Junior MR (2014) Intake of jaborcaba peel attenuates oxidative stress in tissues and reduces circulating saturated lipids of rats with high-fat diet-induced obesity. *J Funct Foods* 6:450-61.
- Bottini M, Rosato N, Bottini N, Huang X, Teng X, Chen D, Tang F, He J (2011) PEG-modified nanotubes in biomedicine: current status and challenges ahead. *Biomacromolecules* 12:3381-93.
- Bresgen N, Jaksch H, Bauer HC, Eckl P, Krizbai I, Tempfer H (2006) Astrocytes are more resistant than cerebral endothelial cells toward geno- and cytotoxicity mediated by short-term oxidative stress. *J Neurosci Res* 84(8):1821-8.
- Byun J (2015) Emerging frontiers of graphene in biomedicine. *J Microbiol Biotechnol* 25(2):145-51.
- Chiang ET, Camp SM, Dudek SM, Brown ME, Usatyuk PV, Zaborina O, Alverdy JC, Garcia JG (2009) Protective effects of high-molecular weight polyethylene glycol (PEG) in human lung endothelial cell barrier regulation: role of actin cytoskeletal rearrangement. *Microvasc Res* 77(2):174-86.
- de Jesus MB, Kapila YL (2014) Cellular mechanisms in nanomaterial internalization, intracellular trafficking, and toxicity. In: Durán N, Guterres SS, Alves OL (ed) *Nanomedicine and Nanotoxicology*, Springer, New York, pp 201-27.
- Guo W, Wang S, Yu X, Qiu J, Li J, Tang W, Li Z, Mou X, Liu H, Wang Z (2016) Construction of a 3D rGO-collagen hybrid scaffold for enhancement of the neural differentiation of mesenchymal stem cells. *Nanoscale* 8:1897-1904.
- Guo X, Mei N (2014) Assessment of the toxic potential of graphene family nanomaterials. *J Food Drug Anal* 22(1):105-15.
- Gupta B, Kumar N, Panda K, Dash S, Tyagi AK (2016) Energy efficient reduced graphene oxide additives: mechanism of effective lubrication and antiwear properties. *Sci Rep* 6:18372. doi: 10.1038/srep18372.
- Halliwell B (2015) *Free radicals and other reactive species in disease*. John Wiley and Sons. doi: 10.1002/9780470015902.a0002269.pub3.
- Hawkins BT, Davis TP (2005) The blood-brain barrier/neurovascular unit in health and disease. *Pharmacol Rev* 57(2):173-85.
- Johansson LH, Borg LAH (1988) A spectrophotometric method for determination of catalase activity in small tissue samples. *Anal Biochem* 174:331-6.

- John AA, Subramanian AP, Vellayappan MV, Balaji A, Mohandas H, Jaganathan SK (2015) Carbon nanotubes and graphene as emerging candidates in neuroregeneration and neurodrug delivery. *Int J Nanomedicine* 10:4267-77.
- Jokerst JV, Lobovkina T, Zare RN, Gambhir SS (2011) Nanoparticle PEGylation for imaging and therapy. *Nanomedicine (Lond)* 6(4):715-28.
- Karlsson M, Kurz T, Brunk UT, Nilsson SE, Frennesson CI (2010) What does the commonly used DCF test for oxidative stress really show? *Biochem J* 428(2):183-90.
- Ke N, Wang X, Xu X, Abassi YA (2011) The xCELLigence system for real-time and label-free monitoring of cell viability. *Methods Mol Biol* 740:33-43.
- Kho D, MacDonald C, Johnson R, Unsworth CP, O'Carroll SJ, Mez ED, Angel CE, Graham ES (2015) Application of xCELLigence RTCA Biosensor Technology for Revealing the Profile and Window of Drug Responsiveness in Real Time. *Biosensors* 5:199-222.
- Le HT, Sin WC, Lozinsky S, Bechberger J, Vega JL, Guo XQ, Sáez JC, Naus CC (2014) Gap junction intercellular communication mediated by connexin43 in astrocytes is essential for their resistance to oxidative stress. *J Biol Chem* 289(3):1345-54.
- Lindstrom NM, Moore DM, Zimmerman K, Smith SA (2015) Hematologic assessment in pet rats, mice, hamsters, and gerbils: blood sample collection and blood cell identification. *Vet Clin North Am Exot Anim Pract* 18(1):21-32.
- Liou GY, Storz P (2010) Reactive oxygen species in cancer. *Free Radic Res* 44(5):479-96.
- Luissint AC, Artus C, Glacial F, Ganeshamoorthy K, Couraud PO. Tight junctions at the blood brain barrier: physiological architecture and disease-associated dysregulation. *Fluids Barriers CNS*. 2012;9(1):23.
- Mendonça MC, Soares ES, de Jesus MB, Ceragioli HJ, Ferreira MS, Catharino RR, da Cruz-Höfling MA (2015) Reduced graphene oxide induce transient blood-brain barrier opening: an *in vivo* study. *J Nanobiotechnol* 13:78. doi: 10.1186/s12951-015-0143-z.
- Mendonça MC, Soares ES, de Jesus MB, Ceragioli HJ, Irazusta SP, Batista ÂG, Vinolo MA⁷, Maróstica Júnior MR, da Cruz-Höfling MA (2016) Reduced graphene oxide: nanotoxicological profile in rats. *J Nanobiotechnology* 14(1):53. doi: 10.1186/s12951-016-0206-9.
- Moret F, Selvestrel F, Lubian E, Mognato M, Celotti L, Mancin F, Reddi E (2015) PEGylation of ORMOSIL nanoparticles differently modulates the *in vitro* toxicity toward human lung cells. *Arch Toxicol* 89(4):607-20.

- Nitta T, Hata M, Gotoh S, Seo Y, Sasaki H, Hashimoto N, Furuse M, Tsukita S (2003) Size-selective loosening of the blood-brain barrier in claudin-5-deficient mice. *J Cell Biol* 161(3):653-60.
- Ohkawa H, Ohishi N, Yagi K (1979) Assay for lipid peroxides in animal-tissues by thiobarbituric acid reaction. *Anal Biochem* 95:351-358.
- Rahman K (2007) Studies on free radicals, antioxidants, and co-factors. *Clin Interv Aging* 2(2):219-236.
- Reshma SC, Syama S, Mohanan PV (2015) Nano-biointeractions of PEGylated and bare reduced graphene oxide on lung alveolar epithelial cells: A comparative *in vitro* study. *Colloids Surf B Biointerfaces* 140:104-16.
- Rouach N, Avignone E, Mème W, Koulakoff A, Venance L, Blomstrand F, Giaume C (2002) Gap junction and connexin expression in the normal and pathological central nervous system. *Biol Cell* 94(7-8):457-75.
- Soenen SJ, Manshian BB, Abdelmonem AM, Montenegro J-M, Tan S, Balcaen L, Vanhaecke F, Brisson AR, Parak WJ, Smedt SCD, Braeckmans K (2014) The cellular interactions of PEGylated gold nanoparticles: effect of PEGylation on cellular uptake and cytotoxicity. *Part Part Syst Charact* 31:794-800.
- Sofroniew MV, Vinters HV (2010) Astrocytes: biology and pathology. *Acta Neuropathol* 119(1):7-35.
- Verhoef JJ, Anchordoquy TJ (2013) Questioning the use of PEGylation for drug delivery. *Drug Deliv Transl Res* 3(6):499-503.
- Verkhatsky A, Nedergaard M (2014) Astroglial cradle in the life of the synapse. *Phil Trans R Soc Lond B Biol Sci* 369:20130595. doi: 10.1098/rstb.2013.0595.
- Vila M, Portolés MT, Marques PA, Feito MJ, Matesanz MC, Ramírez-Santillán C, Gonçalves G, Cruz SM, Nieto A, Vallet-Regi M (2012) Cell uptake survey of pegylated nanographene oxide. *Nanotechnology* 23(46):465103.
- Wallraff A, Kohling R, Heinemann U, Theis M, Willecke K, Steinhauser C (2006) The impact of astrocytic junctional coupling on potassium buffering in the hippocampus. *J Neurosci* 26:5438-47.
- Wilhelm I, Fazakas C, Krizbai IA (2011) *In vitro* models of the blood-brain barrier. *Acta Neurobiol Exp* 71:113-28.
- Wojtoniszak M, Chen X, Kalenczuk RJ, Wajda A, Łapczuk J, Kurzewski M, Drozdziak M, Chu PK, Borowiak-Palen E (2012) Synthesis, dispersion, and cytocompatibility of graphene oxide and reduced graphene oxide. *Colloids Surf B Biointerfaces* 89:79-85.

- Zhang Y, Nayak TR, Hong H, Cai W (2012) Graphene: a versatile nanoplatform for biomedical applications. *Nanoscale* 4(13):3833-42.
- Zhao X, Ahram A, Berman RF, Muizelaar JP, Lyeth BG (2003) Early loss of astrocytes after experimental traumatic brain injury. *Glia* 44(2):140-52.
- Zinkevich T, Venderbosch B, Jaspers M, Kouwer PH, Rowan AE, van Eck ER, Kentgens AP (2016) Solid-state NMR characterization of tri-ethyleneglycol grafted polyisocyanopeptides. *Magn Reson Chem* 54(4):328-33.



IV DISCUSSÃO GERAL

O desenvolvimento de novas tecnologias tem sido um importante fator para o desenvolvimento de terapias mais eficazes para o tratamento de distúrbios neurológicos. Entre as últimas inovações tecnológicas, a nanotecnologia ocupa uma posição de destaque. Contudo, a maioria dos estudos incide essencialmente na avaliação dos efeitos do fármaco comparativamente com o complexo nanocarreador-fármaco, sendo escassos os estudos que avaliam os efeitos que o próprio nanomaterial pode provocar no organismo.

A presente Tese, como já descrito nos capítulos anteriores, mostra a avaliação dos efeitos de um novo nanomaterial da família do grafeno - o óxido de grafeno reduzido, no sistema nervoso central, particularmente na BHE, de ratos adultos e seus potenciais efeitos toxicológicos.

Para melhor compreensão, os resultados discutidos ao longo deste tópico foram divididos em cinco subtópicos: (i) caracterização dos nanomateriais; (ii) distribuição do nanomaterial no parênquima cerebral; (iii) avaliação da integridade da BHE; (iv) avaliação *in vivo* da toxicidade aguda e subcrônica de rGO e (v) avaliação os efeitos da pegulação sobre funcionalidade e toxicidade de rGO *in vitro* e *in vivo*.

4.1 Caracterização dos nanomateriais

Atualmente, não existe um guia de orientações da *Food and Drug Administration* (FDA) ou outra agência regulatória desenvolvido especificamente para o registro de formulações contendo nanomateriais com finalidade terapêutica ou diagnóstica.

A FDA não apresenta uma opinião categórica afirmando que a nanotecnologia é segura ou nociva. A agência visa o desenvolvimento de uma abordagem regulatória adaptável e flexível, que considere as características específicas e os efeitos dos nanomateriais no contexto biológico particular de cada produto e seu uso pretendido [76].

Com esta finalidade, é preciso avaliar uma ampla gama de propriedades físico-químicas para ajudar a determinar se o material produzido é seguro para o uso projetado. Dependendo da aplicação, características como tamanho; morfologia; química de superfície - potencial zeta/carga de superfície, funcionalização; agregação/aglomeração; área

de superfície, porosidade, e quantidade de impurezas devem ser imprescindivelmente avaliadas.

Neste estudo, com o início do processo de redução do material a coloração passou gradualmente de marrom para preto, alteração característica da redução do óxido de grafeno [77]. Para corroborar os dados visuais, a solução aquosa de rGO foi caracterizada por espectroscopia no ultravioleta visível (UV-Vis). O óxido de grafeno apresenta absorção em 230 nm, correspondendo às transições $\pi-\pi^*$ das ligações dos anéis aromáticos C=C, e um ombro em 295 nm, que pode ser atribuído às transições $n-\pi^*$ de ligações C=O [78]. O espectro UV-Vis do rGO (Fig. 1A, Capítulo I), exibiu apenas um pico de absorção em 265 nm, indicando que alguns grupos funcionais disponíveis na superfície foram removidos e a estrutura cristalina do grafeno foi parcialmente restaurada [78].

Uma das técnicas mais utilizadas para caracterização de nanomateriais da família do carbono é a espectroscopia Raman. Esta técnica permite a obtenção de informações sobre as características estruturais dos materiais carbonosos, tais como desordens na estrutura hexagonal do grafite (banda D), vibração no plano de átomos de carbonos sp^2 (banda G) e ordem de empilhamento (banda 2D) [79]. O espectro Raman apresentado na Fig. 1C do Capítulo I apresenta três bandas principais, D (1350 cm^{-1}), G (1598 cm^{-1}) e 2D (2750 cm^{-1}). Nota-se que a intensidade da banda D é superior à G, indicando desorganização na estrutura do material, provavelmente devido ao processo de redução térmica que introduz defeitos na estrutura cristalina em razão da quebra da estrutura gráfica e a presença de grupos funcionais epóxi e hidroxila residuais. O aparecimento da banda 2D indica a presença de multicamadas, confirmado por FE-SEM (Fig. 6A, Capítulo II).

Em relação à morfologia, rGO apresenta-se como finas folhas enrugadas, sobrepostas ou torcidas e intimamente associadas umas com as outras (Fig. 1B, Capítulo I). Imagens similares foram obtidas após a funcionalização de rGO com PEG (Fig. 1C, D, Capítulo IV).

A análise de dispersão dinâmica de luz (DLS, do inglês *Dynamic light scattering*) mostrou que rGO apresenta um padrão diferente de tamanho, carga de superfície e dispersão quando dissolvido em água e após funcionalização com PEG.

Um aumento significativo no tamanho, de $342 \pm 23,5\text{ nm}$ para $910 \pm 32,7\text{ nm}$, foi observado após a peguilação (Tabela 1, Capítulo III). O tamanho é um fator crucial que regula a circulação dos nanomateriais na corrente sanguínea, a penetração através das barreiras fisiológicas, sua localização e até mesmo a indução de respostas celulares [80].

A comparação do potencial zeta revelou que a superfície de carga associada ao rGO apresenta-se mais negativa ($-25 \pm 0,18$ mV) do que rGO-PEG ($-4,2 \pm 3,8$ mV). Isto sugere a existência de ramificações amino positivas, resultando em uma menor carga eletrostática negativa após a funcionalização [81]. Estudos recentes têm mostrado que nanomateriais com carga positiva apresentam melhor captação celular e lisossomal quando comparados com os seus homólogos neutros ou carregados negativamente. No entanto, nanomateriais com carga positiva podem ser mais tóxicos do que os seus homólogos carregados negativamente [82].

Em relação à dispersão, a peguilação de rGO induziu uma diminuição dos valores de PDI de $0,56 \pm 0,03$ para $0,39 \pm 0,04$, indicando homogeneidade do diâmetro das partículas em suspensão, provavelmente devido a menor suscetibilidade de formação de agregados. De qualquer forma, rGO apresentou boa estabilidade em água e diferentes soluções fisiológicas incluindo salina, meio de cultura DMEM e albumina bovina sérica (Fig. 6B, Capítulo III).

Para confirmar a ligação entre rGO e PEG, utilizamos FTIR-ATR e ressonância magnética nuclear de carbono-13. rGO-PEG exibiu um espectro com bandas em 1080 cm^{-1} (-C-O-C), 1641 cm^{-1} (C=O) e 3359 cm^{-1} (O-H) (Fig. 1A, Capítulo III), indicando *crosslink* entre PEG e rGO [83]. O mesmo padrão foi observado na ressonância magnética, com a presença de um pico em 70 ppm correspondente ao grupo -O-CH₂ do PEG [84].

4.2 Distribuição do nanomaterial no parênquima cerebral

O padrão ouro para visualização de nanomateriais em amostras de tecido é a microscopia eletrônica, que apresenta um processo relativamente demorado de preparação e análise das amostras. Além disso, devido ao pequeno campo de visão há dificuldade de localização dos nanomateriais e possibilidade de que a região analisada não seja representativa de todo o tecido. Neste contexto, optamos por utilizar um método de análise alternativo que apresenta baixo custo, simples preparação das amostras e proporciona informações precisas em um amplo campo de observação.

A espectrometria MALDI-MSI permite a análise espacial da distribuição de moléculas específicas obtidas diretamente de secções de tecido congelado. Após a ionização da amostra, a mesma é direcionada para um analisador de massa para separar os íons formados de acordo com suas relações massa/carga (m/z). Então, a partir do

armazenamento do espectro de massas de cada íon, uma imagem bidimensional da amostra pode ser obtida [85].

Inicialmente, realizamos a análise da solução aquosa de rGO para determinarmos os íons mais abundantes. rGO originou quatro picos principais: m/z 285, 421, 465 e 509 (Fig. 2A, Capítulo I). O pico mais proeminente, m/z 465, indica o íon mais abundante formado durante o processo de ionização e, portanto, foi utilizado como precursor para geração das imagens.

As imagens foram obtidas 15 minutos, 1 hora, 3 horas e 7 dias após a injeção intravenosa de 7 mg/Kg de rGO. O nanomaterial apresentou distribuição em todo parênquima cerebral, concentrando-se principalmente em duas regiões cerebrais, o tálamo e o hipocampo (Fig. 3, Capítulo I). O maior acúmulo de rGO nessas regiões demonstra que existem diferenças celulares e moleculares na composição da BHE nas diferentes regiões do cérebro, e que estas regiões são afetadas de forma diversificada segundo a injúria provocada [86]. A identificação das regiões alvo é importante pois permite que tais nanomateriais sejam utilizados no tratamento de doenças específicas, nesse caso por exemplo, a Doença de Alzheimer e Parkinson.

Tendo em vista o potencial uso de rGO para aplicações no campo da neurociência, é fundamental compreender o seu comportamento e biodisponibilidade *in vivo*. Após criação de um histograma baseado na intensidade dos pixels do íon m/z 465 de rGO, realizamos a estimativa da quantidade de rGO presente no parênquima cerebral ao longo do tempo. Houve um aumento progressivo na quantidade de rGO durante as primeiras 3 horas, indicando um movimento contínuo de rGO do sangue para o cérebro. Sete dias após a única administração de rGO, a concentração do nanomaterial no cérebro ainda era significativamente mais elevada do que nas imagem dos animais controle, apresentando quantidades similares às observadas 15 minutos após a administração.

O tamanho de rGO ($342 \pm 23,5$ nm) não foi, aparentemente, um obstáculo à sua entrada no cérebro. Poucos estudos demonstraram a presença de nanopartículas com tamanho entre 200-400 nm no cérebro [87, 88]; entretanto, nenhum destes trabalhos forneceu uma explicação clara do mecanismo pelo qual as nanopartículas chegaram ao cérebro. Possíveis explicações incluem (i) alterações na permeabilidade da BHE; (ii) alterações topológicas (dobramento, rolagem, formação de tubos e ondulações) nas bordas das finas folhas resultariam em dimensões menores e, dessa forma, permitiriam a entrada no cérebro [89]; (ii) deslizamento das folhas de rGO perpendicularmente através das membranas celulares, tal como sugerido *in vitro* [90].

4.3 Avaliação da integridade da BHE

Com base nos resultados obtidos anteriormente, a primeira hipótese avaliada foi de que a entrada de rGO no cérebro estaria relacionada com alterações na permeabilidade da BHE.

Para confirmar tal hipótese, a permeabilidade da BHE foi investigada através do extravasamento do corante azul de Evans [91]. Após administração intravenosa, observou-se que o corante difundiu-se de maneira sistêmica sendo bem evidente nas patas, olhos e orelhas dos animais (Fig. 1, Apêndice). Após 10 minutos de circulação do corante, não havia indícios de sua presença no cérebro dos animais controle (Fig. 5A, Capítulo I), enquanto que o órgão dos animais tratados com rGO encontrava-se impregnado pelo corante (Fig. 5B, Capítulo I), indicando ruptura da BHE.

Após perfusão com solução fisiológica para lavagem do excesso de corante, notou-se que a presença de azul de Evans concentrou-se principalmente no hipocampo, em menor extensão no tálamo e manteve-se ausente nas outras áreas do parênquima cerebral (Fig. 2, Apêndice). De fato, regiões adjacentes às áreas periventriculares são as regiões mais suscetíveis a disfunções na BHE [92].

Para elucidar os mecanismos pelos quais a permeabilidade da BHE foi alterada no hipocampo dos animais tratados com rGO investigamos a participação dos principais mecanismos envolvidos no transporte de substâncias através da BHE: (i) transporte pela via paracelular, controlado pelas junções interendoteliais; (ii) transporte pela via transcelular, uma rota de transporte vesicular; (iii) transporte por proteínas (influxo) e (iv) influência sobre as bombas de efluxo, já que substâncias que induzem ou inibem a P-gp podem resultar em interações farmacocinéticas causando toxicidade.

Inicialmente analisamos a expressão das proteínas interjuncionais ocludina (junção de oclusão); β -catenina (junção de adesão); assim como de laminina, uma das proteínas que compõem a lâmina basal. Nossos dados mostraram que, de fato, rGO promoveu diminuição transitória na expressão das proteínas ocludina, β -catenina e laminina. Ocludina apresentou recuperação total 3 horas após a administração de rGO, enquanto que ocorreu apenas recuperação parcial da expressão das proteínas β -catenina e laminina. Um padrão de recuperação similar foi observado utilizando microscopia eletrônica de transmissão (Fig. 6, Capítulo I).

A influência da administração de rGO sobre a via transcelular foi avaliada através da análise da expressão de caveolina-1, uma vez que o transporte transcelular mediado por

caveólas desempenha um papel importante no transporte de fármacos através da BHE [93]. Quinze minutos e 1 hora após a administração de rGO observou-se um aumento progressivo na expressão de caveolina-1 retornando aos níveis basais após 3 horas (Fig. 3, Apêndice). Recentemente, a proteína caveolina-1 tem sido associada a alterações na permeabilidade da BHE, com aumentos em sua expressão precedendo a diminuição da expressão das proteínas interjuncionais [93], assim como observado neste estudo.

A presença sistêmica de rGO não foi capaz de afetar o influxo transcelular (de glicose) tampouco o efluxo na interface sangue-cérebro (Fig. 4, Apêndice), sugerindo que rGO não é indutor ou inibidor dessas proteínas.

Os resultados obtidos até o momento demonstram que o rGO promove abertura transitória da BHE, cujas proteínas se recuperam total ou parcialmente 3 h após a sua administração. A manutenção da expressão dos transportadores de influxo de glicose e efluxo, fornecem boas perspectivas para o uso de rGO com fins terapêuticos. A identificação de substâncias que regulam a permeabilidade do endotélio cerebral pode contribuir para o desenvolvimento de terapias mais eficazes para o tratamento de distúrbios neurológicos que possuem acesso restrito de fármacos ao cérebro.

4.4. Avaliação *in vivo* da toxicidade aguda e subcrônica de rGO.

Visto que a administração de rGO altera a permeabilidade da BHE afetando tanto o transporte paracelular quanto o transporte transcelular, primeiramente nós investigamos os possíveis efeitos neurotóxicos de rGO.

Durante avaliação clínica, nenhum sinal de alteração do sistema nervoso central e/ou periférico foi observado antes ou após a injeção intravenosa de 7 mg/kg de rGO (Tabela I, Capítulo II). A análise histológica do hipocampo dos animais tratados também não apresentou diferenças morfológicas quando comparada com a análise do hipocampo dos animais controle, independentemente do tempo após a administração de rGO (Fig. 1A,B, Capítulo II).

A figura 1C,D do Capítulo II ilustra a imunomarcagem de NeuN na região CA1 do hipocampo de um rato tratado com veículo (painel C) e 15 minutos após a administração rGO (painel D). Independentemente do tempo de exposição ao rGO, observou-se que os núcleos dos neurônios piramidais das sub-regiões CA1, CA2 e CA3 e dos neurônios granulares do giro denteado apresentaram um padrão de marcação similar entre os grupos controle e tratados. A expressão de NeuN, avaliada por western blotting, apresentou um

aumento imediato (15 minutos) mas ocasional, retornando e permanecendo nos níveis basais 1 hora, 3 horas e 7 dias após a exposição a rGO. Os resultados sugerem que o nanomaterial não interferiu na manutenção da viabilidade neuronal.

Em relação aos astrócitos, observou-se que os corpos e processos astrocíticos positivos para GFAP eram semelhantes nos grupos controle e tratados (Fig. 1 D,E, Capítulo II). Em situações de injúria, os astrócitos respondem rapidamente através de um processo denominado astrogliose, uma marca patológica de lesões estruturais do SNC [17]. A astrogliose é caracterizada por hiperplasia ou hipertrofia dos astrócitos, com consequente aumento de GFAP. A análise da expressão de GFAP mostrou que o tratamento com rGO não induziu alterações significativas nos níveis de GFAP ao longo do tempo (Fig. 1H, Capítulo II), sugerindo que rGO não provoca danos ao SNC.

Um dos pré-requisitos para o uso de nanomateriais com finalidade terapêutica é a compatibilidade com o sangue e seus componentes. Assim, os parâmetros hematológicos dos ratos tratados com rGO foram avaliados e comparados com o grupo controle. Conforme dados da Tabela 2 do Capítulo II, não ocorreram alterações significativas em nenhum dos parâmetros hematológicos analisados. Tem sido demonstrado que nanomateriais baseados em grafeno são compatíveis com sangue e não provocam hemólise, alterações na coagulação ou anormalidades em parâmetros hematológicos [94].

Embora os parâmetros hematológicos dos ratos tratados com rGO não tenham apresentado diferenças quando comparados com os parâmetros dos animais controle, houve indução de leucocitose (rGO 1 hora *vs.* rGO 3 horas) e leucopenia (rGO 3 horas *vs.* rGO 7 dias) intra-grupos; porém, todos os grupos apresentaram valor de leucócitos totais dentro dos valores de referência para ratos Wistar machos [95, 96].

Os leucócitos participam do mecanismo de defesa do organismo e, portanto, a contagem dos leucócitos totais é muito empregada para detecção de possíveis agentes infecciosos ou corpos estranhos. Para confirmar que a indução de leucocitose intra-grupos não representa uma resposta inflamatória em decorrência da abertura da BHE induzida por rGO, nós avaliamos os níveis séricos das citocinas pró-inflamatórias IL-6 e TNF- α e a expressão de IFN- γ e TNF- α em homogenato hipocampal.

Os níveis de ambas citocinas foram indetectáveis no soro dos animais tratados. Em todas as amostras, os níveis de IL-6 e TNF- α encontraram-se abaixo dos valores de referência mínimos, 62,5 pg/mL para IL-6 and 125 pg/ml para TNF- α . Do mesmo modo, nenhuma alteração significativa foi observada na expressão de qualquer um dos marcadores inflamatórios ao longo do tempo (Fig. 2, Capítulo II). Com base nestes resultados e na

ausência de infiltrado de células inflamatórias (Fig. 1B, Capítulo II), sugere-se que o aumento do número de leucócitos não está associado a um processo inflamatório. Um aumento em até duas vezes no número de leucócitos circulantes pode refletir efeitos induzidos fisiologicamente em resposta ao medo, excitação ou exercício [97].

Após administrados, os nanomateriais podem deixar a corrente sanguínea e acumular-se em órgãos vitais como fígado e rins. Neste contexto, os níveis plasmáticos de marcadores de função hepática e renal foram avaliados.

Para avaliar a hepatotoxicidade, os níveis das enzimas transaminases, alanina aminotransferase e aspartato aminotransferase foram analisados. Não houve aumento nos níveis séricos das transaminases comparando-se os grupos tratados ao grupo controle (Tabela 3, Capítulo II). A análise histológica também não indicou alterações na estrutura hepática dos animais tratados com rGO (Fig. 3, Capítulo II).

Os dados da Tabela 3 do Capítulo II, demonstram que não houve alteração significativa nos níveis de creatinina. A dosagem dos níveis séricos de creatinina é corriqueiramente usada para estimar a taxa de filtração glomerular [98]. Entretanto, esta medida pode apresentar baixa sensibilidade para detectar graus leves de perda de função renal. Dessa forma, confirmamos os dados avaliando aspectos morfológicos tais como presença de lesões glomerulares, infiltrado inflamatório, fibrose e células apoptóticas. Nenhuma alteração aparente foi detectada nos animais tratados com rGO (Fig. 4, Capítulo II).

Em complemento, os níveis de ureia também foram investigados. Uma diminuição transitória nos níveis de ureia foi observada 3 h após administração de rGO, em comparação com o grupo controle (Tabela 3, Capítulo II). Alterações intra-grupos também foram observadas (rGO 15 minutos vs. rGO 1 hora e rGO 15 minutos vs. rGO 3 horas). Uma semana após o tratamento com rGO, os níveis de ureia retornaram aos níveis basais. Durante muitos anos a avaliação de ureia foi amplamente utilizada para avaliar a função renal; entretanto, a interpretação dos níveis de ureia devem ser cuidadosamente considerados no contexto clínico uma vez que alterações nos seus níveis podem não estar diretamente relacionados com alterações na função renal [98].

A ureia é produzida pelo fígado e excretada pelos rins, quando esta excreção falha, seja por condições pré-renais quanto renais, a uréia começa a acumular-se no sangue. Nos seres humanos, os baixos níveis de ureia foram observados em várias condições, tais como trauma, cirurgia, desnutrição, excesso de líquido e uso de opióides e esteróides

anabolizantes [99, 100], enquanto que níveis baixos não são comuns e não costumam ser relatados em animais.

Em conjunto, os resultados indicam que rGO é hemocompatível e não apresenta potencial neuro, hepato ou nefrotóxico, podendo ser considerado um nanomaterial não tóxico nas condições experimentais avaliadas.

4.5 Avaliação dos efeitos da peguilação sobre a toxicidade de rGO *in vitro* e *in vivo*.

Na segunda fase do presente projeto, foram realizados testes *in vitro* e *in vivo* com rGO funcionalizado com o polímero PEG visando verificar a influência da peguilação sobre as características funcionais e toxicológicas de rGO. A adição de PEG à superfície de nanomateriais vem sendo amplamente utilizada para reduzir a absorção dos nanomateriais pelo sistema reticuloendotelial, prolongando assim, seu tempo de permanência na circulação sanguínea; além de diminuir a degradação por enzimas metabólicas e reduzir a imunogenicidade e toxicidade [101].

A citotoxicidade de rGO foi avaliada em cultura primária de astrócitos e células endoteliais cerebrais utilizando o ensaio EZ4U e o sistema xCELLigence. Por ambas as metodologias, foi possível observar um decréscimo da viabilidade celular com o aumento da concentração, tanto nos astrócitos (Fig. 2A,B, Capítulo III) quanto nas células endoteliais cerebrais (Fig. 3A,B, Capítulo III), quando comparado aos controles. Não foram observadas diferenças entre os controles e as células tratadas com rGO não peguilado (Fig. 2A,B e Fig. 3A,B, Capítulo III).

Os resultados da imunomarcação com marcadores astrocitários (GFAP e AQP4) e endoteliais (Claudina-5 e ocludina) sugerem que a alteração na viabilidade é decorrente de alterações morfológicas proeminentes que se seguem à morte celular, indicando alta toxicidade do nanomaterial peguilado (Fig. 2E,H e Fig. 3F, Capítulo III).

Deve-se ter cuidado ao afirmar que PEG é um produto não-tóxico e não-imunogênico. Recentemente, alguns estudos têm demonstrado que a inclusão de PEG em nanopartículas e fármacos promove a ativação do sistema complemento e induz a produção de anticorpos anti-PEG, que aceleram a sua depuração comprometendo a eficácia terapêutica [102]. Além disso, outros estudos demonstraram que moléculas terapêuticas que exigem entrega intracelular, tais como siRNA e genes, quando peguiladas apresentam redução na sua captação e entrega [103].

Nos estudos *in vivo*, os animais tratados com rGO-PEG apresentaram uma diminuição mais acentuada e prolongada na expressão das proteínas interjuncionais e da laminina (Fig. 4, Capítulo III) quando comparados com os resultados dos animais tratados com rGO apresentados anteriormente (Fig. 7, Capítulo I).

Outro ponto abordado no sentido de confirmar os resultados obtidos *in vitro*, foi a determinação *in vivo* da expressão de GFAP e Cx43. Nos últimos anos, tem sido proposto que as conexinas possuem um papel importante na estabilização das junções endoteliais cerebrais uma vez que o uso de inibidores de conexinas resulta na regulação negativa de ocludina e claudina com conseqüente aumento na permeabilidade da barreira [104].

Nossos dados mostraram que a presença do rGO-PEG na circulação foi capaz de afetar a expressão de GFAP e Cx43 de forma similar (Fig. 5, Capítulo III). Entre 3 horas e 7 dias após administração de rGO-PEG, ocorreu uma diminuição progressiva na expressão de ambas proteínas, provavelmente em decorrência de morte celular. Sabe-se que diminuições na expressão de Cx43 resultam em aumento da morte astrocitária induzida por espécies reativas de oxigênio (EROs) [105].

Para confirmar tal hipótese, avaliamos a produção de EROs (*in vitro*) e as enzimas do sistema antioxidante enzimático catalase e SOD (*in vivo*) após administração de rGO-PEG em comparação com os efeitos de rGO não peguilado.

Nos astrócitos, a concentração mais elevada de rGO-PEG induziu um aumento de 270% nos níveis intracelulares de EROs, enquanto que rGO induziu um aumento de 33 %, em comparação com os respectivos controles (veículos) (Fig. 6A, Capítulo III). Nas células endoteliais cerebrais apenas o tratamento com rGO-PEG induziu aumento na produção intracelular de EROs (Fig. 6B, Capítulo III).

A comparação da expressão de catalase e SOD-1 após administração de rGO (Fig. 5, Capítulo II) e de rGO-PEG (Fig. 7, Capítulo III), revelou um aumento apenas na expressão de catalase após a administração do nanomaterial peguilado. Em complemento, a análise dos níveis séricos das mesmas enzimas indicou um aumento nos níveis de SOD 1 h e 7 dias após o tratamento com ambos nanomateriais (Tabela 4, Capítulo II e Tabela 2, Capítulo III); e um aumento nos níveis de catalase 7 dias após o tratamento com rGO-PEG (Tabela 2, Capítulo III). Não houve indução de peroxidação lipídica, avaliada pelo teste de TBARS, em nenhum dos grupos analisados.

Embora a formulação de rGO tenha induzido um aumento nos níveis de EROs nos astrócitos e nos níveis séricos de SOD *in vivo*, este nanomaterial mostrou-se menos tóxico que seu padrão peguilado, que induziu alterações proeminentes em todas as análises

realizadas. Tal comportamento pode estar relacionado ao fato de que rGO não atinge o limiar necessário para produzir toxicidade celular, demonstrando que seus efeitos são autolimitados.

Em conjunto, esses resultados demonstram que o efeito citotóxico causado por rGO-PEG nos astrócitos e nas células endoteliais cerebrais está intimamente envolvido com a produção de EROs, o que poderia acarretar diversos outros danos celulares, como por exemplo, alterações genotóxicas. Dessa forma, utilizamos o ensaio de micronúcleos em sangue periférico como bioindicador de genotoxicidade. Foi observado um aumento da frequência de micronúcleos de $0,32 \pm 0,149$ para $0,64 \pm 0,193$ nos animais expostos à rGO-PEG por 7 dias. Em comparação, a frequência de micronúcleos dos animais controle e tratados com rGO manteve-se similar ($0,68 \pm 0,13$ vs. $0,64 \pm 0,19$) (Tabela 5, Capítulo II).

Danos hepáticos e renais também são comumente avaliados em estudos envolvendo nanomateriais que induzem estresse oxidativo. A grande maioria dos compostos endógenos e xenobióticos são biotransformados no fígado e excretados pelos rins. Estudos histológicos evidenciaram alterações morfológicas hepáticas e renais nos grupos tratados com rGO-PEG.

Na análise hepática dos animais tratados com PEG (grupo controle), observou-se uma organização estrutural típica, veias centrais normais, ausência de infiltrado inflamatório e presença de raros hepatócitos com núcleos picnóticos e cromatina condensada (Fig. 5A, Apêndice). Nos animais tratados com rGO-PEG observou-se congestão dos sinusóides iniciando 3 horas após sua administração (Fig. 5C, Apêndice) e culminando com fibrose aos 7 dias (Fig. 5E, Apêndice).

O parênquima renal dos animais controle apresentou glomérulos em quantidade adequada, sem alterações histológicas e ausência de alterações túbulo-intersticiais (Fig. 6A, Apêndice). Entretanto, 15 minutos após a administração de rGO-PEG observou-se hipertrofia tubular discreta (Fig. 6B, Apêndice) acompanhada por glomérulos escleróticos entre 1 hora (Fig. 6C, Apêndice) e 3 horas (Fig. 6D, Apêndice). Ambas alterações encontradas nos rins dos grupos tratados foram reversíveis. Decorridos 7 dias da exposição à rGO-PEG, o córtex renal apresentou sinais de recuperação (Fig. 6E, Apêndice).

Os resultados aqui relatados demonstram que a ligação de PEG à rGO provocou uma associação sinérgica que culminou em graves efeitos tóxicos. As diferenças entre o presente estudo e alguns resultados encontrados na literatura podem ser explicadas por

diferenças no desenho e modelo experimental. É evidente que as características físico-químicas dos nanomateriais devem ser consideradas em termos de efeitos toxicológicos.

Em relação ao futuro desenvolvimento de revestimentos de superfície de nanomateriais, ressaltamos que a peguilação pode não ser sempre a melhor estratégia no desenvolvimento de dispositivos para a entrega de fármacos.



V CONCLUSÕES

Com base nos resultados obtidos neste trabalho concluímos que:

- A suspensão aquosa de rGO demonstrou bons parâmetros referentes a tamanho, índice de polidispersão e potencial zeta.
- Há diferenças regionais na localização de rGO, provavelmente devido a heterogeneidade da BHE em diversas regiões do cérebro. rGO acumulou-se principalmente no tálamo e hipocampo. O entendimento das características regionais da BHE é importante para desenvolver uma base de conhecimento das propriedades de transporte sangue-cérebro, fundamental para o carreamento de fármacos para áreas cerebrais de interesse.
- A injeção intravenosa única de 7mg/kg de rGO provocou abertura transitória da BHE de ratos Wistar adultos, particularmente na região do hipocampo. O período de 1 hora após a administração do nanomaterial parece ser crítico na resposta dos animais.
- A alteração na permeabilidade da BHE provocada por rGO foi identificada através do extravasamento do corante azul de Evans e da presença do traçador extracelular nitrato de lantânio no espaço interendotelial. Os mecanismos pelos quais a permeabilidade da BHE foi alterada envolvem tanto o transporte paracelular quanto o transporte transcelular.
- Os testes hematológicos, histopatológicos, bioquímicos e genotóxicos demonstraram que, nas condições experimentais utilizadas, rGO induz efeitos toxicológicos mínimos. As alterações ocorrem de forma dinâmica e autolimitante, não induzindo danos permanentes.
- A PEGuilação de rGO melhorou sua dispersibilidade mas não sua interação com componentes celulares da BHE. rGO-PEG provocou efeitos deletérios significativos em astrócitos e células endoteliais assim como diminuição na expressão de marcadores astrocitários (GFAP e Cx43) e das junções interendoteliais (occludina e β -catenina) em homogenato hipocampal. A formação intracelular de espécies reativas de oxigênio *in vitro*

e o aumento no sistema antioxidante enzimático *in vivo* induzido por rGO-PEG sugerem danos mediados por estresse oxidativo.

Conclusão geral:

Em conjunto os dados sugerem que rGO, mas não rGO-PEG, pode ser uma ferramenta promissora para o carregamento de fármacos empregados no tratamento de disorders cerebrais que normalmente não respondem aos tratamentos convencionais devido à impermeabilidade da BHE.



VI REFERÊNCIAS

1. Abbott NJ, Ronnback L, Hansson E. Astrocyte-endothelial interactions at the blood brain barrier. *Nat Rev Neurosci.* 2006; 7:41-53.
2. Hawkins BT, Davis TP. The blood-brain barrier/neurovascular unit in health and disease. *Pharmacol Rev.* 2005; 57(2):173-85.
3. Chen Y, Liu L. Modern methods for delivery of drugs across the blood-brain barrier. *Adv Drug Deliv Rev.* 2012; 64(7):640-65.
4. Daneman R. The blood-brain barrier in health and disease. *Ann Neurol.* 2012; 72(5):648-72.
5. Wallez Y, Huber P. Endothelial adherens and tight junctions in vascular homeostasis, inflammation and angiogenesis. *Biochim Biophys Acta.* 2008; 1778(3):794-809.
6. Hartsock A, Nelson WJ. Adherens and tight junctions: structure, function and connections to the actin cytoskeleton. *Biochim Biophys Acta.* 2008; 1778(3):660-9.
7. Bazzoni G, Dejana E. Endothelial cell-to-cell junctions: molecular organization and role in vascular homeostasis. *Physiol Rev.* 2004; 84(3):869-901.
8. Nakase T, Naus CC. Gap junctions and neurological disorders of the central nervous system. *Biochim Biophys Acta.* 2004; 1662(1-2):149-58.
9. De Bock M, Vandenbroucke RE, Decrock E, Culot M, Cecchelli R, Leybaert L. A new angle on blood-CNS interfaces: a role for connexins?. *FEBS Lett.* 2014; 588(8):1259-70.
10. Winkler EA, Bell RD, Zlokovic BV. Central nervous system pericytes in health and disease. *Nat Neurosci.* 2011; 14(11):1398-405.
11. Bonkowski D, Katyshev V, Balabanov RD, Borisov A, Dore-Duffy P. The CNS microvascular pericyte: pericyte-astrocyte crosstalk in the regulation of tissue survival. *Fluids Barriers CNS.* 2011; 8(1):8. doi: 10.1186/2045-8118-8-8.
12. Wang CX, Shuaib A. Critical role of microvasculature basal lamina in ischemic brain injury. *Prog Neurobiol.* 2007; 83(3):140-8.
13. Molofsky AV, Krencik R, Ullian EM, Tsai HH, Deneen B, Richardson WD, et al. Astrocytes and disease: a neurodevelopmental perspective. *Genes Dev.* 2012; 26(9):891-907.

14. Cabezas R, Avila M, Gonzalez J, El-Bachá RS, Báez E, García-Segura LM, et al. Astrocytic modulation of blood brain barrier: perspectives on Parkinson's disease. *Front Cell Neurosci.* 2014; 8:211. doi: 10.3389/fncel.2014.00211.
15. Giaume C, Naus CC. Connexins, gap junctions, and glia. *WIREs Membr Transp Signal.* 2013; 2:133-42.
16. Papadopoulos MC, Verkman AS. Aquaporin water channels in the nervous system. *Nat Rev Neurosci.* 2013; 14(4):265-77.
17. Sofroniew MV, Vinters HV. Astrocytes: biology and pathology. *Acta Neuropathol.* 2010; 119(1):7-35.
18. Muoio V, Persson PB, Sendeski MM. The neurovascular unit - concept review. *Acta Physiol (Oxf).* 2014; 210(4):790-8.
19. Duan W, Zhang YP, Hou Z, Huang C, Zhu H, Zhang CQ, et al. Novel Insights into NeuN: from Neuronal Marker to Splicing Regulator. *Mol Neurobiol.* 2016; 53(3):1637-47.
20. Marques-Deak A, Sternberg E. Psiconeuroimunologia - A relação entre o sistema nervoso central e o sistema imunológico *Rev. Bras. Psiquiatr.* 2004; 26(3). doi: 10.1590/S1516-44462004000300002
21. Stamatovic SM, Keep RF, Andjelkovic AV. Brain endothelial cell-cell junctions: how to "open" the blood brain barrier. *Curr Neuropharmacol.* 2008; 6(3):179-92.
22. Wong AD, Ye M, Levy AF, Rothstein JD, Bergles DE, Searson PC. The blood-brain barrier: an engineering perspective. *Front Neuroeng.* 2013; 6:7. doi: 10.3389/fneng.2013.00007.
23. Xiao G, Gan L. Receptor-mediated endocytosis and brain delivery of therapeutic biologics. *Int. J. Cell Biol.* 2013, Article ID 703545. doi:10.1155/2013/703545.
24. Lu CT, Zhao YZ, Wong HL, Cai J, Peng L, Tian XQ. Current approaches to enhance CNS delivery of drugs across the brain barriers. *Int J Nanomedicine.* 2014;9:2241-57.
25. Stockwell J, Abdi N, Lu X, Maheshwari O, Taghibiglou C. Novel central nervous system drug delivery systems. *Chem Biol Drug Des.* 2014 ;83(5):507-20.
26. Chapman CD, Frey WH, Craft S, Danielyan L, Hallschmid M, Schiöth HB, et al. Intranasal treatment of central nervous system dysfunction in humans. *Pharm Res.* 2013; 30(10):2475-84.
27. Pathan SA, Iqbal Z, Zaidi SM, Talegaonkar S, Vohra D, Jain GK, et al. CNS drug delivery systems: novel approaches. *Recent Pat Drug Deliv Formul.* 2009; 3(1):71-89.

28. Fortuna A, Alves G, Serralheiro A, Sousa J, Falcão A. Intranasal delivery of systemic-acting drugs: small-molecules and biomacromolecules. *Eur J Pharm Biopharm.* 2014; 88(1):8-27.
29. Zawilska JB, Wojcieszak J, Olejniczak AB. Prodrugs: a challenge for the drug development. *Pharmacol Rep.* 2013; 65(1):1-14.
30. Löscher W, Potschka H. Drug resistance in brain diseases and the role of drug efflux transporters. *Nat Rev Neurosci.* 2005; 6(8):591-602.
31. Meairs S. Facilitation of drug transport across the blood-brain barrier with ultrasound and microbubbles. *Pharmaceutics.* 2015; 7(3):275-293.
32. Saunders NR, Habgood MD, Møllgård K, Dziegielewska KM. The biological significance of brain barrier mechanisms: help or hindrance in drug delivery to the central nervous system?. *F1000Res.* 2016 Mar 10;5. pii: F1000 Faculty Rev-313. doi: 10.12688/f1000research.7378.1. eCollection 2016.
33. Rapoport SI. Osmotic opening of the blood-brain barrier: principles, mechanism, and therapeutic applications. *Cell Mol Neurobiol.* 2000; 20(2):217-30.
34. Saija A, Princi P, Trombetta D, Lanza M, De Pasquale A. Changes in the permeability of the blood-brain barrier following sodium dodecyl sulphate administration in the rat. *Exp Brain Res.* 1997; 115(3):546-51.
35. Pardridge WM. Blood-brain barrier delivery. *Drug Discov Today.* 2007;12(1-2):54-61.
36. Gregor A, Lind M, Newman H, Grant R, Hadley DM, Barton T, et al. Phase II studies of RMP-7 and carboplatin in the treatment of recurrent high grade glioma. RMP-7 European Study Group. *J Neurooncol.* 1999; 44(2):137-45.
37. Warren K, Jakacki R, Widemann B, Aikin A, Libucha M, Packer R, et al. Phase II trial of intravenous lobradimil and carboplatin in childhood brain tumors: a report from the Children's Oncology. *Cancer Chemother Pharmacol.* 2006; 58(3):343-7.
38. European Commission (EC). [Internet]. Definition of a nanomaterial. 2011/696/UE. [updated 2016 Feb 03]. Available from: http://ec.europa.eu/environment/chemicals/nanotech/faq/definition_en.htm
39. Radomska A, Leszczyszyn J, Radomski MW. The nanopharmacology and nanotoxicology of nanomaterials: new opportunities and challenges. *Adv Clin Exp Med.* 2016; 25(1):151-62.
40. Cha C, Shin SR, Annabi N, Dokmeci MR, Khademhosseini A. Carbon-based nanomaterials: multifunctional materials for biomedical engineering. *ACS Nano.* 2013; 7(4):2891-7.

41. Geim AK, Novoselov KS. The rise of graphene. *Nature Materials*. 2007; 6:183-91.
42. Zhu Y, Murali S, Cai W, Li X, Suk JW, Potts JR, et al. Graphene and graphene oxide: synthesis, properties, and applications. *Adv Mater*. 2010; 22(35):3906-24.
43. Servant A, Bianco A, Prato M, Kostarelos K. Graphene for multi-functional synthetic biology: the last 'zeitgeist' in nanomedicine. *Bioorg Med Chem Lett*. 2014; 24(7):1638-49.
44. Goenka S, Sant V, Sant S. Graphene-based nanomaterials for drug delivery and tissue engineering. *J Control Release*. 2014; 173:75-88.
45. Krishnamoorthy K, Veerapandian M, Yun K, Kim SJ. The chemical and structural analysis of graphene oxide with different degrees of oxidation. *Carbon*. 2013; 53:38-49.
46. Georgakilas V, Tiwari JN, Kemp KC, Perman JA, Bourlinos AB, Kim KS, et al. Noncovalent functionalization of graphene and graphene oxide for energy materials, biosensing, catalytic, and biomedical applications. *Chem Rev*. 2016; 116 (9):5464-559.
47. Chowdhury DR, Singh C, Paul A. Role of graphite precursor and sodium nitrate in graphite oxide synthesis. *RSC Adv*. 2014; 4:15138-45
48. Konios D, Stylianakis MM, Stratakis E, Kymakis E. Dispersion behaviour of graphene oxide and reduced graphene oxide. *J Colloid Interface Sci.*, 2014; 430:108-12.
49. University of Turku [Internet]. Graphenes. Available from: <https://www.utu.fi/en/units/sci/units/chemistry/research/mcca/Pages/Sub-pages%20of%20Functional%20Materials/Graphenes.aspx>
50. Pei S, Cheng HM. The reduction of graphene oxide. *Carbon*, 2012;50: 3210-28.
51. Li J, Zeng X, Ren T, van der Heide E. The Preparation of graphene oxide and its derivatives and their application in bio-tribological systems. *Lubricants*. 2014; 2:137-161.
52. Georgakilas V, Otyepka M, Bourlinos AB, Chandra V, Kim N, Kemp KC, et al. Functionalization of graphene: covalent and non-covalent approaches, derivatives and applications. *Chem Rev*. 2012; 112(11):6156-214.
53. Dreyer DR, Park S, Bielawski CW, Ruoff RS. The chemistry of graphene oxide. *Chem Soc Rev*. 2010; 39:228-240.
54. Layek RK, Nandi AK, A review on synthesis and properties of polymer functionalized graphene. *Polymer*. 2013; 54(19):5087-103.

55. Yang C, Denno ME, Pyakurel P, Venton BJ. Recent trends in carbon nanomaterial-based electrochemical sensors for biomolecules: A review. *Anal Chim Acta*. 2015; 887:17-37.
56. Kim SK, Kim D, Jeon S. Electrochemical determination of serotonin on glassy carbon electrode modified with various graphene nanomaterials. *Sens. Actuators B Chem*. 2012; 174:285-29.
57. Yagati AK, Park J, Cho S. Reduced graphene oxide modified the interdigitated chain electrode for an insulin sensor. *Sensors*. 2016. 16(1):109. doi: 10.3390/s16010109.
58. Wei J, Qiu J, Li L, Ren L, Zhang X, Chaudhuri J, et al. A reduced graphene oxide based electrochemical biosensor for tyrosine detection. *Nanotechnology*. 2012; 23(33):335707. doi: 10.1088/0957-4484/23/33/335707.
59. Sethuraman V, Muthuraja P, Anandha Raj J, Manisankar P. A highly sensitive electrochemical biosensor for catechol using conducting polymer reduced graphene oxide-metal oxide enzyme modified electrode. *Biosens Bioelectron*. 2015. doi: 10.1016/j.bios.2015.12.074.
60. Liu TC, Chuang MC, Chu CY, Huang WC, Lai HY, Wang CT, et al. Implantable graphene-based neural electrode interfaces for electrophysiology and neurochemistry in *in vivo* hyperacute stroke model. *ACS Appl Mater Interfaces*. 2016; 8(1):187-96.
61. Monaco AM, Giugliano M. Carbon-based smart nanomaterials in biomedicine and neuroengineering. *Beilstein J Nanotechnol*. 2014; 5:1849-63.
62. Akhavan O. Graphene scaffolds in progressive nanotechnology/stem cell-based tissue engineering of nervous systems. *J Mater Chem B*. 2016; 4: 3169-3190.
63. Defterali Ç, Verdejo R, Peponi L, Martín ED, Martínez-Murillo R, López-Manchado MÁ, et al. Thermally reduced graphene is a permissive material for neurons and astrocytes and *de novo* neurogenesis in the adult olfactory bulb *in vivo*. *Biomaterials*. 2016; 82:84-93.
64. Bressan E, Ferroni L, Gardin C, Sbricoli L, Gobbato L, Ludovichetti FS, et al. Graphene based scaffolds effects on stem cells commitment. *J Transl Med*. 2014; 12:296. doi: 10.1186/s12967-014-0296-9.
65. Shin SR, Li YC, Jang H, Khoshakhlagh P, Akbari M, Nasajpour A, et al. Graphene-based materials for tissue engineering. *Adv Drug Deliv Rev*. 2016. doi: 10.1016/j.addr.2016.03.007.
66. Orecchioni M, Cabizza R, Bianco A, Delogu LG. Graphene as cancer theranostic tool: progress and future challenges. *Theranostics*. 2015; 5(7):710-23.

67. Wu S-Y, An SSA, Hulme J. Current applications of graphene oxide in nanomedicine. *Int J Nanomedicine*. 2015; 10:9-24.
68. Donaldson K, Stone V, Tran CL, Kreyling W, Borm PJ. Nanotoxicology. *Occup Environ Med*. 2004;61(9):727-8.
69. Jiang J, Oberdorster G, Biswas P. Characterization of size, surface charge, and agglomeration state of nanoparticle dispersions for toxicological studies. *J Nanopart Res*. 2009; 11:77-89.
70. Martinez DST, Alves OL. Interação de nanomateriais com biosistemas e a nanotoxicologia: na direção de uma regulamentação. *Cienc. Cult*. 2013; 65(3):32-36.
71. Nehoff H, Parayath NN, Taurin S, Greish K. *In vivo* evaluation of acute and chronic nanotoxicity. In: Sahu SC, Casciano DA, editors. *Handbook of nanotoxicology, nanomedicine and stem cell use in toxicology*. Chichester: John Wiley & Sons; 2014.
72. Bianco A. Graphene: safe or toxic? The two faces of the medal. *Angew Chem Int Ed Engl*. 2013; 52:4986-97.
73. Ma Y, Shen H, Tu X, Zhang Z. Assessing in vivo toxicity of graphene materials: current methods and future outlook. *Nanomedicine (Lond)*. 2014; 9(10):1565-80.
74. Singh Z. Applications and toxicity of graphene family nanomaterials and their composites. *Nanotechnol Sci Appl*. 2016; 9: 15-28.
75. Syama S, Mohanan PV. Safety and biocompatibility of graphene: A new generation nanomaterial for biomedical application. *Int J Biol Macromol*. 2016; 86:546-55.
76. FDA. [Internet]. FDA's Approach to Regulation of Nanotechnology Products. Available from: <http://www.fda.gov/ScienceResearch/SpecialTopics/Nanotechnology/ucm402230.htm#approach>
77. Feng H, Cheng R, Zhao X, Duan X, Li J. A low-temperature method to produce highly reduced graphene oxide. *Nat Commun*. 2013; 4:1539. doi: 10.1038/ncomms2555.
78. Yang S, Yue W, Huang D, Chen C, Lin H, Yang X. A facile green strategy for rapid reduction of graphene oxide by metallic zinc. *RSC Adv*. 2012; 2:8827-32.
79. Ferrari AC, Basko DM. Raman spectroscopy as a versatile tool for studying the properties of graphene. *Nat Nanotechnol*. 2013; 8:235-46.
80. Jiang W, Kim BY, Rutka JT, Chan WC. Nanoparticle-mediated cellular response is size-dependent. *Nat Nanotechnol*. 2008; 3(3):145-50.
81. Vila M, Portolés MT, Marques PA, Feito MJ, Matesanz MC, Ramírez-Santillán C, et al. Cell uptake survey of pegylated nanographene oxide. *Nanotechnology*. 2012; 23(46):465103.

82. Lin PC, Lin S, Wang PC, Sridhar R. Techniques for physicochemical characterization of nanomaterials. *Biotechnol Adv.* 2014; 32(4):711-26.
83. Gupta B, Kumar N, Panda K, Dash S, Tyagi AK. Energy efficient reduced graphene oxide additives: mechanism of effective lubrication and antiwear properties. *Sci. Rep.* 2016; 6:18372. doi: 10.1038/srep18372.
84. Zinkevich T, Venderbosch B, Jaspers M, Kouwer PH, Rowan AE, van Eck ER, et al. Solid-state NMR characterization of tri-ethyleneglycol grafted polyisocyanopeptides. *Magn Reson Chem.* 2016; 54(4):328-33.
85. Menegasso ARS. Desenvolvimento da Técnica de MALDI Imaging utilizando tecidos animais [Trabalho de conclusão de curso]. Rio Claro: Universidade Estadual Paulista, Instituto de Biociências; 2010.
86. Nyúl-Tóth Á, Suciú M, Molnár J, Fazakas C, Haskó J, Herman H, et al. Differences in the molecular structure of the blood-brain barrier in the cerebral cortex and white matter: an *in silico*, *in vitro* and *ex vivo* study. *Am J Physiol Heart Circ Physiol.* 2016. doi: 10.1152/ajpheart.00774.2015.
87. Schroeder U, Sommerfeld P, Sabel BA. Efficacy of oral dalarginloaded nanoparticle delivery across the blood-brain barrier. *Peptides.* 1998; 19:777-80.
88. Selvi BR, Jagadeesan D, Suma BS, Nagashankar G, Arif M, Balasubramanyam K, et al. Intrinsically fluorescent carbon nanospheres as a nuclear targeting vector: delivery of membrane-impermeable molecule to modulate gene expression *in vivo*. *Nano Lett.* 2008; 8:3182-8.
89. Ivanovskaya VV, Wagner P, Zobelli A, Suarez-Martinez I, Yaya A, Ewels CP. Graphene edge structures: folding, scrolling, tubing, rippling and twisting. In: Ottaviano L, Morandi V, editors. *GraphITA 2011*, Springer: Heidelberg, Berlin, 2012, p. 75-85.
90. Russier J, Treossi E, Scarsi A, Perrozzi F, Dumortier H, Ottaviano L, et al. Evidencing the mask effect of graphene oxide: a comparative study on primary human and murine phagocytic cells. *Nanoscale.* 2013; 5(22):11234-47.
91. Nag S. Blood-brain barrier permeability using tracers and immunohistochemistry. *Methods Mol Med.* 2003; 89:133-44.
92. Ueno M, Akiguchi I, Hosokawa M, Kotani H, Kanenishi K, Sakamoto H. Blood-brain barrier permeability in the periventricular areas of the normal mouse brain. *Acta Neuropathol.* 2000; 99(4):385-92.
93. Zhao YL, Song JN, Zhang M. Role of caveolin-1 in the biology of the blood-brain barrier. *Rev Neurosci.* 2014; 25(2):247-54.

94. Pinto AM, Gonçalves IC, Magalhães FD. Graphene-based materials biocompatibility: a review. *Colloids Surf B Biointerfaces*. 2013; 111:188-202.
95. Lindstrom NM, Moore DM, Zimmerman K, Smith SA. Hematologic assessment in pet rats, mice, hamsters, and gerbils: blood sample collection and blood cell identification. *Vet Clin North Am Exot Anim Pract*. 2015; 18(1):21-32.
96. Kampfmann I, Bauer N, Johannes S, Moritz A. Differences in hematologic variables in rats of the same strain but different origin. *Vet Clin Pathol*. 2012; 41(2):228-34.
97. Haschek WM, Rousseaux CG, Wallig MA. *Fundamentals of Toxicologic Pathology*, 2nd ed, Amsterdam: Elsevier/Academic Press; 2010.
98. Ferguson MA, Waikar SS. Established and emerging markers of kidney function. *Clin Chem*. 2012;58(4):680-9.
99. Gowda S, Desai PB, Kulkarni SS, Hull VV, Math AAK, Vernekar SN. Markers of renal function tests. *N Am J Med Sci*. 2010;2:170-3.
100. Pagana KD, Pagana TJ. *Mosby's manual of diagnostic and laboratory tests*. 4th ed. St. Louis: Mosby Elsevier; 2010.
101. Kolate A, Baradia D, Patil S, Vhora I, Kore G, Misra A. PEG - a versatile conjugating ligand for drugs and drug delivery systems. *J Control Release*. 2014;192:67-81.
102. Verhoef JJ, Carpenter JF, Anchordoquy TJ, Schellekens H. Potential induction of anti-PEG antibodies and complement activation toward PEGylated therapeutics. *Drug Discov Today*. 2014; 19(12):1945-52.
103. Verhoef JJ, Anchordoquy TJ. Questioning the Use of PEGylation for Drug Delivery. *Drug Deliv Transl Res*. 2013; 3(6):499-503.
104. De Bock M, Vandenbroucke RE, Decrock E, Culot M, Cecchelli R, Leybaert L. A new angle on blood-CNS interfaces: a role for connexins? *FEBS Lett*. 2014; 588(8):1259-70.
105. Le HT, Sin WC, Lozinsky S, Bechberger J, Vega JL, Guo XQ, et al. Gap junction intercellular communication mediated by connexin43 in astrocytes is essential for their resistance to oxidative stress. *J Biol Chem*. 2014; 289(3):1345-54.


VII APÊNDICE



Fig. 1 Fotografia representativa da distribuição do corante Azul de Evans 3 horas após a injeção de rGO (7mg/kg).

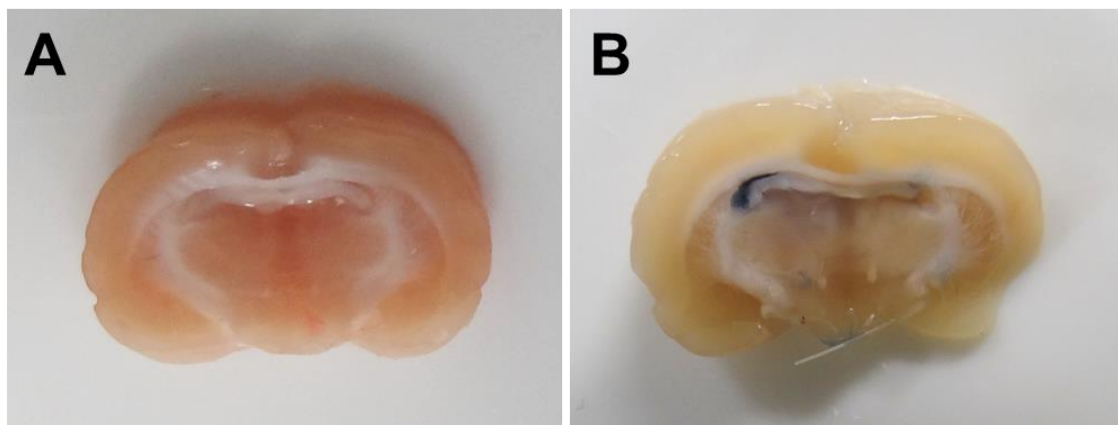


Fig. 2 Fotografias representativas de ratos adultos injetados com Azul de Evans 3 horas após a administração de (A) água destilada e (B) rGO.

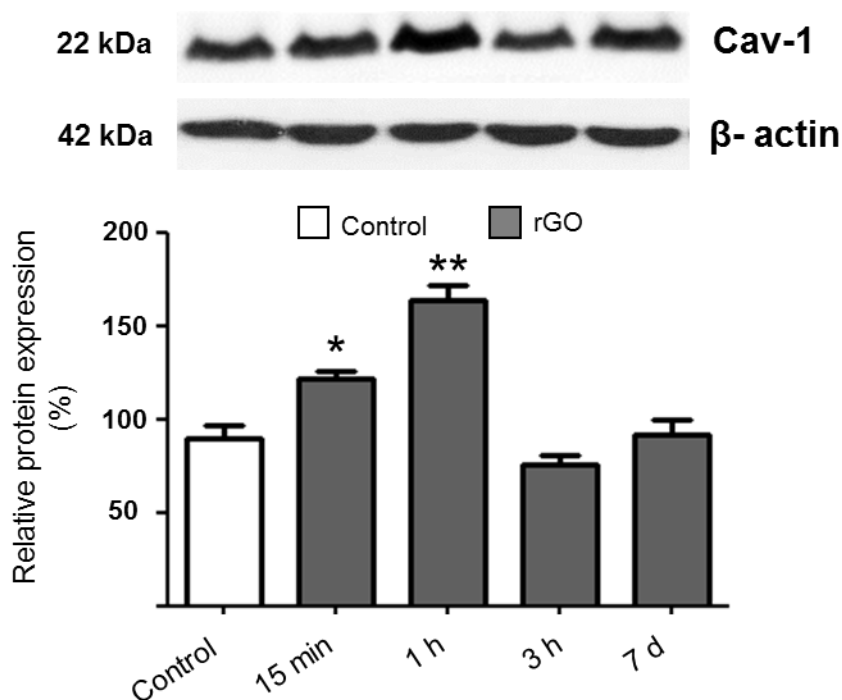


Fig. 3 Expressão de caveolina-1 após a administração i.v. de 7 mg/kg de rGO. As bandas foram normalizadas com o controle endógeno β-actina e quantificadas densitometricamente. Foram considerados significativos * $p < 0,05$ e ** $p < 0,01$ quando comparados ao grupos controle. Student *t*-test; dados apresentados como média ± SEM.

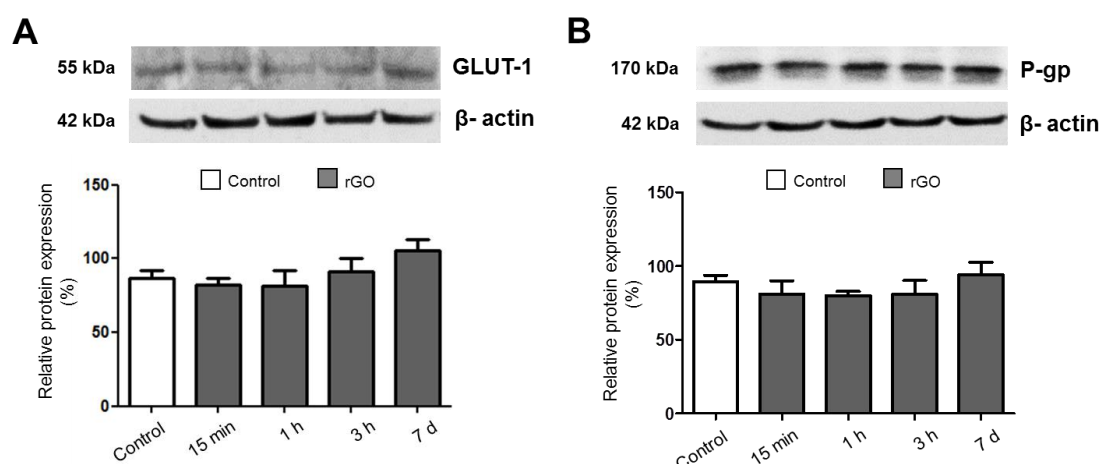


Fig. 4 Efeitos da administração i.v. de 7 mg/kg de rGO na expressão da (A) proteína de influxo de glicose GLUT-1 e (B) proteína de efluxo P-gp em homogenato hipocampal. As bandas foram normalizadas com o controle endógeno β-actina e quantificadas densitometricamente.

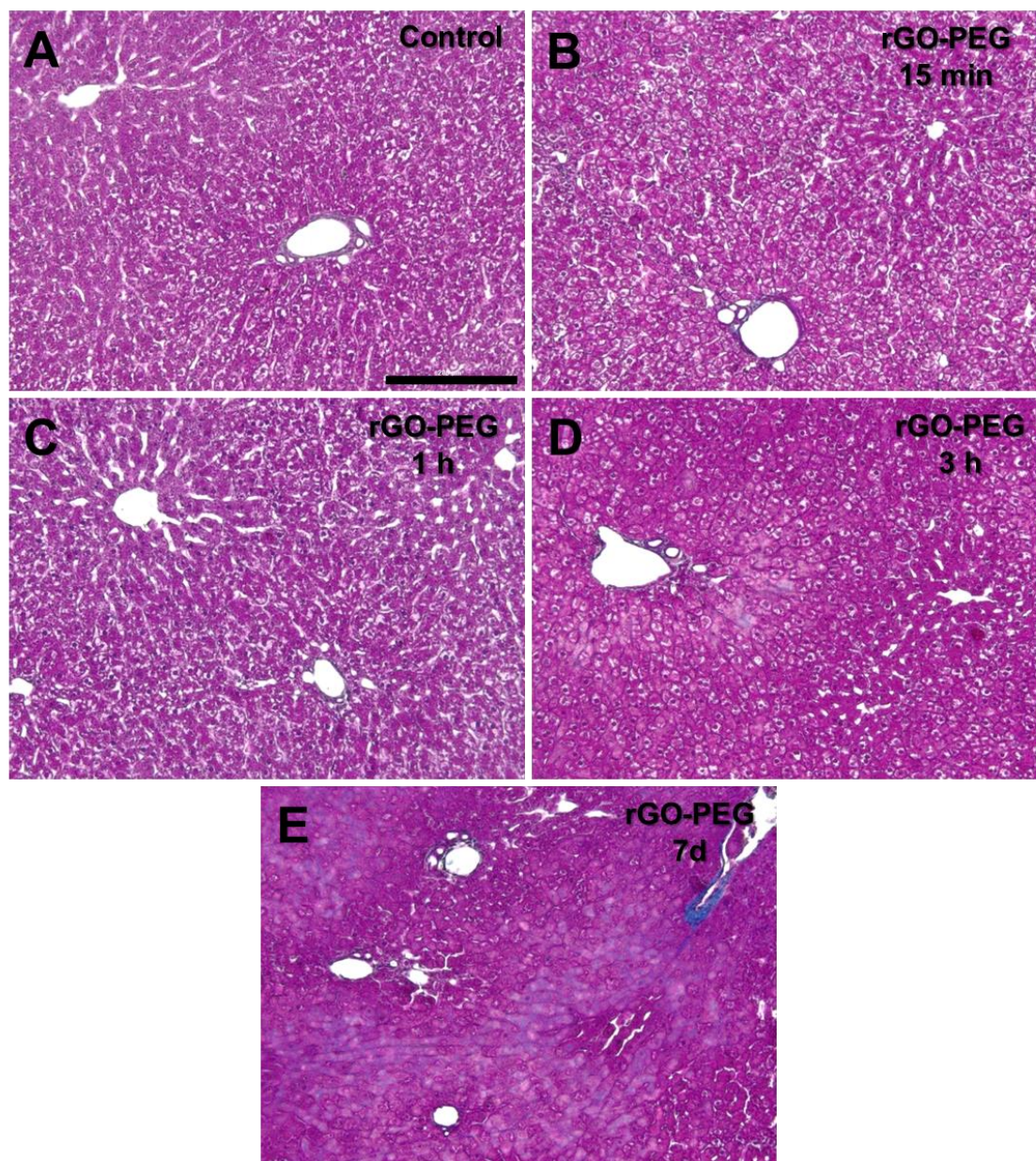


Fig. 5 Fotomicrografias representativas de secções histológicas de fígado após injeção i.v. de (A) PEG (controle) e (B-E) rGO-PEG. Coloração tricrômico de Masson. Barra = 200 μm .

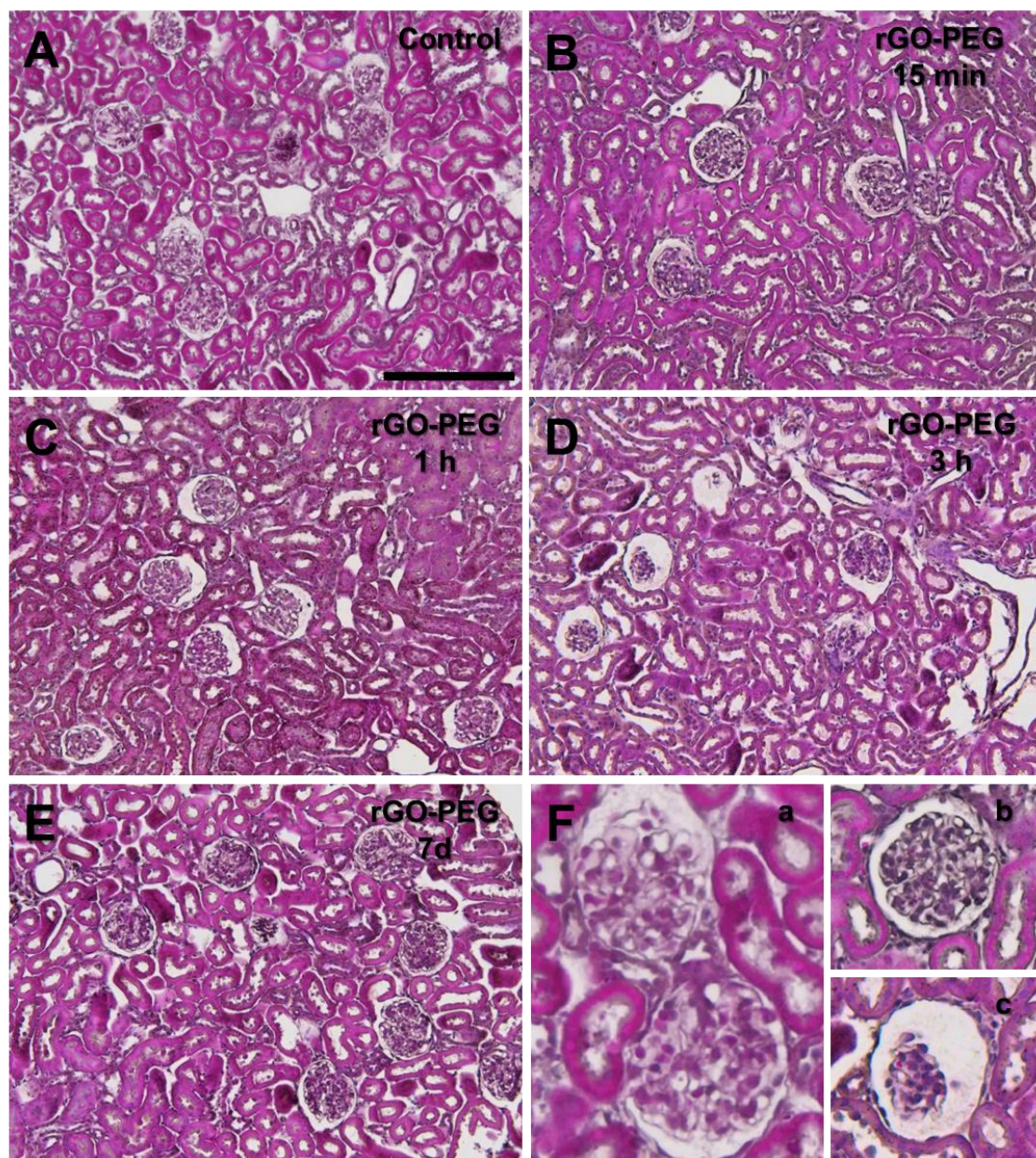




Fig. 6 Fotomicrografias representativas do cortex renal após injeção i.v. de (A) PEG (controle) e (B-E) rGO-PEG. (F) Foco no glomérulo de um animal (a) controle e após (b) 15 minutos e (c) 3 horas da administração de rGO-PEG. Secções coradas com tricrômico de Masson. Barra = 200 μm .



VIII ANEXOS

Anexo 7.1 Certificado da Comissão de Ética no Uso de Animais


CERTIFICADO

Certificamos que a proposta intitulada Óxido de grafeno e sistema nervoso central: avaliação dos efeitos na barreira hematoencefálica e perfil nanotoxicológico, registrada com o nº 2884-1, sob a responsabilidade de Profa. Dra. Maria Alice da Cruz Hofling / Monique Culturato Padilha Mendonça, que envolve a produção, manutenção ou utilização de animais pertencentes ao filo *Chordata*, subfilo *Vertebrata* (exceto o homem) para fins de pesquisa científica (ou ensino), encontra-se de acordo com os preceitos da LEI Nº 11.794, DE 8 DE OUTUBRO DE 2008, que estabelece procedimentos para o uso científico de animais, do DECRETO Nº 6.899, DE 15 DE JULHO DE 2009, e com as normas editadas pelo Conselho Nacional de Controle da Experimentação Animal (CONCEA), tendo sido aprovada pela Comissão de Ética no Uso de Animais da Universidade Estadual de Campinas - CEUA/UNICAMP, em 22 de outubro de 2012.


Finalidade:	() Ensino (X) Pesquisa Científica
Vigência do projeto:	01/2013-01/2016
Vigência da autorização para manipulação animal:	01/2013-01/2016
Espécie / linhagem/ raça:	Rato heterogênico / Wistar
No. de animais:	174
Peso / Idade:	06 semanas / 200g
Sexo:	Machos
Origem:	CEMIB/UNICAMP

A aprovação pela CEUA/UNICAMP não dispensa autorização prévia junto ao IBAMA, SISBIO ou CIBio.

Campinas, 12 de abril de 2016.



Prof. Dra. Liana Maria Cardoso Verinaud
Presidente



Fátima Alonso
Secretária Executiva

IMPORTANTE: Pedimos atenção ao prazo para envio do relatório final de atividades referente a este protocolo: até 30 dias após o encerramento de sua vigência. O formulário encontra-se disponível na página da CEUA/UNICAMP, área do pesquisador responsável. A não apresentação de relatório no prazo estabelecido impedirá que novos protocolos sejam submetidos.

CEUA/UNICAMP
Caixa Postal 6109
13083-970 Campinas, SP – Brasil

Telefone: (19) 3521-6359
E-mail: comisib@unicamp.br
<http://www.ib.unicamp.br/ceea/>

Anexo 7.2 - Direitos Autorais

Dear BioMed Central Customer Services team,

I am the first author of the article "Reduced graphene oxide induces transient blood-brain barrier opening: an in vivo study (DOI: 10.1186/s12951-015-0143-z)" and I would like to add the manuscript to my PhD Thesis. How can I obtain the permission?

Best regards,

Monique Culturato Padilha Mendonça

Institute of Biology, State University of Campinas (UNICAMP)

Department of Biochemistry and Tissue Biology

Rua Charles Darwin, SN

CEP 13083-863

+55 (19) 3521-6250 (19) 98189-3252

De: Ricardo Sison Jr. <info@biomedcentral.com> (info@biomedcentral.com)

Enviada: quarta-feira, 4 de maio de 2016 18:03:54

Para: mo_padilha@hotmail.com (mo_padilha@hotmail.com)

Dear Dr. Mendonca,

Thank you for contacting BioMed Central.

The article you refer to is an open access publication. Therefore you are free to use the article for the purpose required, as long as its integrity is maintained and its original authors, citation details and publisher are identified.

For detailed information about the terms please refer to the open access license: <http://www.biomedcentral.com/about/policies/license-agreement>

If you have any questions please do not hesitate to contact me.

Best wishes,

Joel Lagmay

Customer Services

info@biomedcentral.com

Phone: +44 (0)203 192 2009 Fax: +44 (0)203 192 2010